Modeling the Performance of the Piston Ring-Pack with Consideration of Non-Axisymmetric Characteristics of the Power Cylinder System in Internal Combustion Engines

by

Liang Liu

B.S. Automotive Engineering
Xi'an Jiaotong University, 1993

M.S. Mechanical Engineering
Wayne State University, 2000

Submitted to the Department of Mechanical Engineering
in Partial Fulfillment of the Requirements for the Degree of
Doctor of Philosophy

at the

Massachusetts Institute of Technology

February 2005

Signature of Author _____
Department of Mechanical Engineering
January, 2005

Certified by _____
Tian Tian
Lecturer, Department of Mechanical Engineering
Thesis Supervisor

Accepted by _____
Lallit Anand
Chairman, Department Committee on Graduate Studies
Department of Mechanical Engineering

(This page intentionally left blank)

Modeling the Performance of the Piston Ring-Pack with Consideration of Non-Axisymmetric Characteristics of the Power Cylinder System in Internal Combustion Engines

by

Liang Liu

Submitted to the Department of Mechanical Engineering
January 27, 2005
In Partial Fulfillment of the Requirements for the Degree of Doctor of Philosophy

ABSTRACT

The performance of the piston ring-pack is directly associated with the friction, oil consumption, wear, and blow-by in internal combustion engines. Because of non-axisymmetric characteristics of the power cylinder system, the performance of a ring varies along its circumference. Investigating these variations is of great interest for developing advanced ring-packs, but is out of the capabilities of the existing two-dimensional models. In this work, three separate but closely related numerical models were developed to study the performance of the piston ring-pack.

The model for static analysis was developed to facilitate the design of piston rings. In this model, a finite beam element model is adopted with incorporation of a physics-based sub-model describing the interaction between the ring and the bore as well as the ring and the groove. A step-by-step approach is adopted to calculate the ring/bore and ring/groove conformability if the free shape of the ring is given. A method that can be used to determine the free shape as to achieve a specific tension distribution is also developed. Model results revealed the complex ring/bore and ring/groove interaction.

A three-dimensional model for ring dynamics and blow-by gas flow was developed to address non-axisymmetric characteristics of the power cylinder system. In this model, the rings are discretized into straight beam elements. 3-D finite element analysis is employed to address the structural response of each ring to external loads. Physics-based sub-models are developed to simulate each ring's interactions with the piston groove and the liner. The gas flows driven by the pressure difference along both the axial and circumferential directions are modeled as well. This model predicts the inter-ring gas pressure and 3-D displacements of the three rings at various circumferential locations. Model results show significant variations of the dynamic behavior along ring circumference.

In the ring-pack lubrication model, an improved flow continuity algorithm is implemented in the ring/liner hydrodynamic lubrication, and proves to be very practicable. By coupling the ring/liner lubrication with the in-plane structural response of the ring, the lubrication along the entire ring circumference can be calculated. Model results show significant variations of lubrication along the circumference due to the non-axisymmetric characteristics of the power cylinder system. Bore distortion was found to have profound effects on oil transport along the liner. Particularly, it stimulates the occurrence of oil up-scraping by the top ring during compression stroke. Because the oil evaporation on the liner affects the liner oil film thickness, a sub-model for liner evaporation with consideration of multi-species oil is incorporated with the lubrication model. With consideration of oil transport along the liner, the prediction of evaporation is more precise.

The combination of these models is a complete package for piston ring-pack analysis. It is computationally robust and efficient, and thus has appreciable practical value.

Thesis Supervisor:

Tian Tian
Lecturer, Department of Mechanical Engineering

(This page intentionally left blank)

ACKNOWLEDGEMENT

I would like to thank my committee members for their guidance and constructive advices. In particular, I would like to thank my thesis supervisor Dr. Tian Tian, who not only gave me the opportunity to conduct my doctoral studies in MIT, but also supported and guided me consistently through his insightful and broad knowledge. I enjoyed and will remember every single discussion with him, which helped me to solve the problems I encountered and eventually leaded to the achievement of my thesis work. Besides being a respectable advisor, Dr. Tian has been the most instructive and supportive friend during the four and half years I spent in MIT. I would also like to express my gratitude to Professor John B. Heywood for the continuous help over the years, especially those advices on how to make good presentations. My sincerely thanks to Professor Gareth Mckinley and Professor Samir Nayfeh for accepting being part of the committee and delightful suggestions.

I would like to thank the members of the Consortium on Lubrication in Internal Combustion Engines at MIT, which include Mahle GmBh, AB Volvo, Dana Corporation, Peugeot PSA and Renault SA, for sponsoring this research. Also I would like to take this opportunity to thank the passionate and gifted engineers from these companies, specifically Remi Rabute and Randy Lunsford at Dana, Dr. Rolf-Gerhard Fiedler and Dr. Eduardo Tomanik at Mahle, Dr. Sebastien Messse and Dr. Gabriel Cavallaro at Peugeot PSA, Bengt Olson and Fredrick Stromstedt at Volvo. Their intensive testing works on the models and valuable feedbacks are crucial for the model development. Meanwhile, through the pleasant communication with them, I have gained precious practical engineering experiences, which are very difficult to obtain in school.

I gratefully acknowledge the support from the Sloan Automotive Laboratory faculty and staff: Professor Wai K. Cheng, Dr. Victor W. Wong, Thane Dewitt, Alexis Rozantes, and Karla Stryker.

I would like to thank Yong Li, Fiona McClure, Jinchul Hong, Ertan Yilmaz, Benoist Thirouard, Mohammad Rassuili, Yeunwoo Cho, Adam Vokac, and Yuetao Zhang for their contribution to my thesis work and the friendships that make my time in MIT enjoyable and fulfilling. I would also like to thank the following graduate students and visiting engineers in the Sloan Automotive Laboratory for their help: Steve Przesmitzki, Grant Smedley, Oscar Lopez, Jeff Jocsak, Morgan Andreae, Brian Hallgren, Ioannis Kitsopanidis, Halim Santoso, Matias Saiz.

The solid engineering background I obtained in Xi'an Jiaotong University has helped me to confront the difficulties I encountered in the courses and research in MIT. I would therefore be very grateful to the professors over there: Professor Yumei Chen, Professor Huixian Shen, and Professor Deming Jiang. Specifically, I sincerely thank Professor Shen for leading me to America and further to MIT.

I would like to express my deepest thanks to my lovely wife Lei for her support, sacrifice, patience, and most of all, her love throughout these years. Her encouragement has been one of the key driving forces for me to strive and archive a meaningful life goal.

I would like to express my special thanks to my parents, sister and brother. This thesis would not have been completed without their unconditional support.

Liang Liu
January 2005

(This page intentionally left blank)

Table of Contents

List of Figures

List of Tables

Chapter 1 Introduction

1.1 Importance of Piston Ring-Pack Performance

Development of modern automotive engines is driven by three major factors: fuel economy, pollutant engine-out emission, and customer satisfaction [1]. To satisfy these requirements, advanced technologies are needed for all aspects of engines, including lubrication oil, fuel and engine components. The performance of the piston ring-pack in an engine is directly associated with the friction, wear, blow-by gas flow and oil consumption, which are in turn closely related to the listed three factors. Therefore, a detailed understanding of the piston ring-pack performance is crucial for developing advanced internal combustion engine.

The friction generated between the piston ring-pack and the cylinder liner account for 50% of the power loss in power cylinder system, which is about half of the total engine mechanical losses [2]. Thus, reduction of ring/liner friction can improve fuel economy significantly. Since ring/liner friction is largely determined by the ring/liner lubrication, the lubrication performance of piston ring-pack need to be well investigated. Meanwhile, the ring dynamics behavior determines inter-ring gas pressure and ring dynamic twist, which are crucial to the ring/liner lubrication, thus should be thoroughly studied.

Wear inevitably occurs on the ring/liner and ring/groove interface due to the pair's contact and relative sliding. As a result of wear, the geometric and material properties of rings, liner and piston grooves are changed, which could alter the performance of the power cylinder system. Excessive wear induces unpredictable engine performance and even failure. In order to study the wear, one has to have a good understanding of the ring-pack lubrication and dynamics.

Blow-by gas flow refers to the undesired gas flow from the combustion chamber to the crankcase. As a result, some unburned working charge may leak from the combustion chamber and make no contribution to producing work. During the power stroke, the blow-by gas leakage will decrease the in-cylinder pressure and hence diminish the engine power. Blow-by gas flow is strongly associated with the performance of piston ring-pack, especially the ring dynamics, as they determine the parameters of gas flow passages.

Engine oil consumption is recognized to be a significant source of pollutant emissions. Unburned or partially burned oil in the exhaust gases contributes directly to hydrocarbon and particulate emissions. Moreover, chemical compounds in oil additives can poison exhaust treatment devices and severely reduce their conversion efficiency. Oil consumption is arguably the most complicated

problem in the power cylinder system, and it is still the least understood area although a great deal of effort has been made. The key to understand engine oil consumption is the oil transport, i.e. how the oil is transported from lower region to the combustion chamber. Among several possible oil paths, oil paths along the liner and along the piston are two major ones. Oil transport along the liner is largely determined by the ring-pack lubrication, while oil transport along the piston is mainly controlled by the ring-pack dynamics and blow-by gas flow. The study of ring performance can help to understand the oil transport mechanism and lead to effective ways of reducing the oil consumption.

Among the efforts to investigate the piston ring-pack performance, numerical simulation has been advancing in many aspects and playing a very important role. Numerical models can be categorized into static analysis and dynamic analysis. The static analysis refers to the study of the static interaction between a single ring and the power cylinder system, while the dynamic analysis includes ring-pack lubrication modeling, ring-pack dynamics and blow-by simulation during engine operation. In the following sections, the existing modeling works and their limitations are reviewed.

1.2 Static Analysis

Ring design can be divided into two categories: geometry-mechanical designs and material/coating designs. In geometry-mechanical design of single-piece piston rings, there are three key elements, namely ring shape in its free state (called free shape hereafter), cross-section, and ring running-surface profile, and they play key roles in determining the interaction between the ring and the cylinder liner, as well as the ring and the piston groove in operating engine [3, 4].

Without gas pressure effects, the contact pressure distribution between a single piece ring and the bore is determined by the free shape of ring and the bore shape. The bore shape is not perfectly circular (called bore distortion), which is mainly caused by thermal expansion and cylinder head bolting. Meanwhile, the free shape of the ring is seldom found exactly as designed, largely due to plastic deformation in certain stages of manufacture. It is crucial in practice to know the actual contact pressure distribution if given the ring free shape and bore shape.

There are several published analytical studies of ring/bore conformability. A solution for a circular ring conforming to a circular bore with a smaller diameter can be found in Timoshenko and Lessells's work [5], where a formula is given for a variable wall thickness of a ring (of rectangular cross-sections) needed to produce uniform contact pressure on a circular bore. The contact between a circular ring of constant cross-section and a circular bore is non-uniform. An analytical solution to this problem can be found in Feodosyev's work [6]. A more advanced ring/bore conformability study was conducted by Sun [7]. In his study, the ring was modeled as a curved beam under in-plane loads (elastic load, gas load and thermal load) at steady state in any distorted bore. Ma et al. [8] developed several independent models (gap model, cable model and thermal liner model) using commercial software (ANSYS) to study ring/bore conformability, and the effect of thermal stresses on ring/bore conformability was also included.

The assumption of small displacement was made in most of these existing models. In reality, however, the shape change is significant when the ring is compressed to fit into the bore, and the small displacement assumption would introduce noteworthy errors. Meanwhile, all the existing models were developed for ring with symmetric cross-sections. But in practice, most rings are designed to have asymmetric cross-sections. If an asymmetric ring is inserted into the bore, the ring will have linear and angular displacement in all directions, which influences ring/bore interaction and makes the involvement of ring/groove interaction necessary.

It is of practical interest for ring designers to have an analytical tool to calculate the required ring free shape that can provide the desired ring/bore contact pressure distribution. The analytical solution for the free shape of the ring with constant rectangular cross-section to provide uniform ring/bore

contact pressure distribution was given by Prescott et al. [9], and the solution is often quoted by the piston ring industry as the basis of piston ring design. However, there is currently no reliable computational tool to quantitatively determine the free shape for an arbitrary contact pressure distribution.

To control gas or oil transport more efficiently, compression rings are often designed to have static twist angles after being inserted into the piston and cylinder environment. This is accomplished by making the ring cross-section asymmetric. A reliable numerical tool to connect design parameters and ring static twist can facilitate the design process and minimize the number of iterations required to obtain the desired static twist. Very few published studies on the ring static twist calculation are presently available. Dunaevsky et al. [10-12] has serial publications about theoretical models that can be used to calculate the ring static twist. However, the boundary conditions applied in those calculations do not really correspond to the engine applications.

1.3 Dynamic Analysis

The dynamic analysis of the piston ring-pack are usually further categorized into dynamics analysis and lubrication analysis. The major subject of dynamics analysis is to study the axial, radial and twist displacements of a ring during an engine cycle, while the main goal of lubrication analysis is to investigate the ring/liner friction and oil transport along the liner.

1.3.1 Two-Dimensional Models for Ring-Pack Dynamics

During an engine cycle, the ring-pack exhibits complex dynamic behaviors, which change the flow paths for both gases and oil, and influence the lubrication condition in ring/liner and ring/groove interfaces [3, 4]. Numerical modeling has proved to be a useful tool in understanding the piston ring-pack's dynamic behaviors [13-19, 62]. Most of the published models consider the coupling of ring dynamics and gas flow. In these models, although the ring gaps are taken into account for gas flow calculations, the ring is essentially assumed to be a perfect circle for the purpose of modeling its axial and angular dynamics. The major differences between these so-called two-dimensional (2-D) models lie in how ring/groove and ring/liner interactions and gas flows are modeled. It was demonstrated that once these interactions and gas flows are modeled properly, 2-D model can be very useful in analyzing the overall dynamic behaviors of piston ring-pack [18, 19].

1.3.2 Two-Dimensional Models for Ring-Pack Lubrication

Ring lubrication has been modeled by a number of researchers [4, 20-25, 62]. Most of the existing models are based on the axisymmetric assumption, which neglects the variations of ring/liner interaction along the circumference and hence only considers one cross-section. To consider the oil starvation, extensive efforts were made to locate the actual hydrodynamic lubrication region between the ring and the liner by implementing reasonable boundary conditions. Meanwhile, great emphases have been placed on flow continuity of lubrication oil in order to simulate the oil transport along the liner more accurately. With the help of these so-called 2-D models, a great deal of detailed analysis of ring lubrication has been performed and some conclusions have been used successfully in guiding the practical application [19].

1.3.3 Necessity of Three-Dimensional Models for Ring-Pack Performance

Although these 2-D models for piston ring-pack performance have proved to be useful, there exist a number of non-axisymmetric characteristics in the piston, piston rings and cylinder bore that can be crucial to the performance of the ring-pack.

From piston ring point of view, the existence of an end gap and asymmetric cross-section, which is often used to seal oil or gases more efficiently, creates non-uniform internal stress along the ring circumference. As a result, a ring can have axial bending and non-uniform twist along its circumference when it is inserted into the engine and interacts with the surroundings [26]. Furthermore, the flanks of piston rings, especially ones of keystone type, may have waviness along their circumference due to the limitation of the manufacture process.

Piston grooves are distorted due to temperature variation inside the piston and high combustion pressure, and the groove distortion usually exhibits non-uniformity along the circumference. Additionally, piston secondary motion, namely piston tilt and lateral motion, may affect ring behaviors differently from thrust side to anti-thrust side.

Bore distortion, which is unavoidably generated in the process of manufacture and assembly and under the influence of thermal and pressure in operation, can greatly influence the ring/bore conformability. Even with the help of self-tension of the ring, some portion of the ring can not conform to the bore during some parts of the engine cycle. The ring/bore clearance varies significantly along the circumference, and modeling the ring performance is out of the capability of 2-D models.

All of these non-axisymmetric characteristics existing in piston rings, piston, and cylinder bore can result in non-uniform geometrical relationship between the ring and the liner as well as the ring and the groove along the circumference, which can bring in non-uniformity along the circumference in terms of ring/liner and ring/groove interactions as well as the gas and oil flows through the ring/liner and ring/groove interfaces. For certain engines and operating conditions, the localized effects due to these 3-D features may significantly affect the overall behavior of the piston rings, gas and oil flows.

Furthermore, there exists a non-uniform gas pressure distribution along the circumference of the piston lands between the ring gaps. If the variation of gas pressure in the same piston land region is significant, it might generate localized ring motion. Moreover, the gas flow along the piston circumference driven by the pressure difference was found to be one of the main driving forces for the oil motion on the piston [27], and more precise information on this gas flow can provide better input for studying oil transport on the piston.

Understanding the effects of all of the non-axisymmetric characteristics in power cylinder systems requires full resolution of the ring structural response to dynamic loadings and its effects on sealing and lubrication. So far, the modeling work that couples ring structure analysis with dynamics, gas flow and lubrication has been limited in terms of physics considerations and practical applications.

The efforts to model the ring dynamics in 3-D manner are hardly found in the publications. Ejacov et al. [28] simulated the dynamic twist angle of the piston ring-pack along the circumference by using finite element analysis. The ring dynamic twist was found to have influence on the ring lift and inter-ring gas pressure. As for other aspects of the non-axisymmetric features of the power cylinder system and their affect on the on the ring dynamics, very few published works have investigation.

Among those attempts of 3-D lubrication modeling, the work of Hu et al. [29] and the work of Ma et al. [30, 31] are representative. In [29], a combination of a detailed elastic analysis and a complementarity method was used to evaluate the ring/bore conformability in an accurate way. But the assumption of leading edge being fully flooded in the hydrodynamic lubrication was not realistic. Ma et al. [30, 31] implemented a flow-continuity algorithm in the hydrodynamic lubrication sub-model, which well addressed the oil starvation and ensured an accurate oil transport simulation. However, the ring/bore conformability was evaluated by an empirical approximation. Nevertheless, both works revealed significant variations of ring/liner lubrication along the circumference due to bore distortion.

1.4 Objectives of the Thesis Work

As discussed in previous sections, existing numerical simulations of the ring-pack performance have some limitations when more detailed analysis about the ring performance is needed. In this study, numerical models for both static and dynamic analysis will be developed, trying to relax those limitations and therefore explore the effects of non-axisymmetric characteristics of the power cylinder system on the piston ring-pack performance.

1.4.1 Static Analysis – An Analytical Tool for Piston Ring Design

To meet the practical requirements of the ring manufacturers, the static analysis needs to function as an analytical tool for piston ring design, which can be used in the early stage of ring design. The so-called ring design tool should include following functions:

- Given the free shape of a ring, calculate the ring/bore and ring/groove conformability, static twist angle distribution.
- Given the ring/bore contact pressure distribution, calculate the ring free shape.
- Estimate the effects of external forces on ring/bore and ring/groove conformability

1.4.2 Dynamic Analysis

For the dynamic analysis, 3-D models need to be developed in order to address those non-axisymmetric characteristics of the power cylinder system. To avoid the unnecessary complexity of coupling ring dynamics and ring lubrication, two 3-D models are to be developed separately.

Ring-Pack Dynamics model

By coupling the ring dynamics and blow-by gas flow, this model should have the capabilities of predicting

- 3-D displacements of the ring-pack, including ring flutter, ring collapse.
- Inter-ring gas pressure, its circumferential variation and induced gas flow
- Effects of the non-axisymmetric features of the power cylinder system on ring-pack dynamics

Ring-Pack Lubrication Model

To develop a 3-D ring-pack lubrication model, following efforts have to be conducted

- Developing a mass conserved hydrodynamic lubrication sub-model
- Coupling ring structure response with the ring/liner lubrication

- Predicting oil transport along the liner

Because oil evaporation will change the oil film thickness on the liner to some extent, advanced ring-pack lubrication model should include the effects of oil evaporation. Meanwhile, modeling oil evaporation itself is one of the most critical works for oil consumption analysis. Due to the fact that lubricant oil is a mixture composed of several distinct hydrocarbon species each with its own boiling point and associated vapor pressure, the composition of oil on the liner, which has significant temperature variation along its axial direction, will be different from location to location. The movement of piston ring-pack may transport oil from one location to another along the liner, and thus can change the oil composition. For simulating the oil evaporation on the liner, it is therefore very crucial to consider the effects of oil transport by the ring movement on the oil composition on the liner. When the ring-pack lubrication model is successfully developed, the oil transport along the liner is a precious result and can be used in modeling oil evaporation on the liner. Therefore, a model for oil evaporation on the liner is of interest and should be developed in current thesis work.

Being a sub-model of the ring-pack lubrication model, the prospective oil evaporation model should have following features:

- Model the oil as a mixture of distinct hydrocarbon species.
- Predict the rate of oil evaporation on the liner
- Use the information of oil transport along the liner from the lubrication model to calculate the change of oil composition
- Estimate the influence of the oil evaporation on oil film thickness

The combination of above models for static and dynamic analysis will be a comprehensive numerical package that can be used to study the piston ring-pack performance. Its functions will range from ring design all the way to ring performance analysis, and largely facilitate the investigation of the piston ring-pack performance.

(This page intentionally left blank)

Chapter 2 Static Analysis – An Analytical Tool for Piston Ring Design

2.1 Introduction

The goal of this work is to develop a comprehensive analytical tool to address structure related issues in the piston ring design. A full 3-D finite beam element model is adopted with incorporation of an asperity contact sub-model describing the interaction between the ring and the bore as well as the ring and the groove.

In this chapter, the model development is detailed firstly. In the model development, the 3-D finite element beam model is described. Then, a step-by-step approach is adopted to calculate the ring/bore and ring/groove conformability if the free shape of a ring is given. As supplements to the conformability calculation, modeling lapping process and thermal stress effects are introduced to meet the requirements of practical application. Then a method that can be used to determine the ring free shape as to achieve a specific ring/bore contact pressure distribution is developed. The calculation of ring ovality is introduced at last.

After the model development, the model is applied to some practical examples and in depth discussions are carried out. Some of the model results are compared with the experimental data.

2.2 Model Development

2.2.1 Three-Dimensional Finite Beam Element Analysis

A 3-D finite beam element model is employed to relate the loads acting on the ring and the deformation of the ring. The ring is first discretized into beam elements. For each beam element, as shown in Figure 2-1 the *ith* element, there are twelve degrees of freedom (u'_1~ u'_{12}, called DOF hereafter), including six linear displacements and six angular displacements. Corresponding to each DOF, there is one load (s'_i), which represents force for linear displacement or moment for angular displacement. The finite element formula relating displacements with loads is:

$$K'^{i}\, U'^{i} = S'^{i} + S_I'^{i} \tag{2.1}$$

where K'^{i} is the stiffness matrix (12×12) for the *ith* element, U'^{i} the displacement vector (12×1), S'^{i} the load vector (12×1), and $S_I'^{i}$ the initial load vector (12×1). The detailed mathematical description of the finite beam element model can be found in [28].

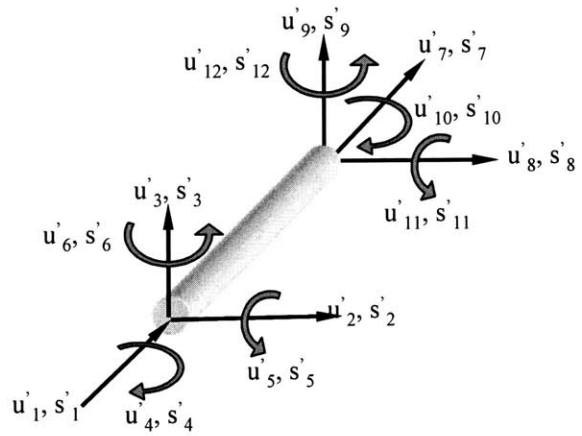

Figure 2-1 Degrees of freedom and loads on a beam element

Before applying Equation (2.1) to structural analysis, it is worthwhile to transform the coordinate system used above into more convenient one. In this study, the radial, tangential and axial directions of a ring are chosen as the final coordinate system for each node. As sketched in Figure 2-2, where "o" is the center of the ring, the coordinate systems (x_1', y_1', z_1') and (x_2', y_2', z_2'), which are used in Equation (2.1) for node 1 and node 2, are transformed to system (x_1, y_1, z_1) and (x_2, y_2, z_2), respectively. For a symmetric ring, z_1 and z'_1 coincide with each other, and so do z_2 and z'_2, as shown

in Figure 2-2. However, for an asymmetric ring, they do not coincide. After the coordinate transformation, Equation (2.1) is converted to

$$K^i U^i = S^i + S_I^{\ i} \tag{2.2}$$

where K^i is the stiffness matrix for *ith* element in the new coordinate systems, U^i the new displacement vector, S^i the new load vector, and $S_I^{\ i}$ the new initial load vector.

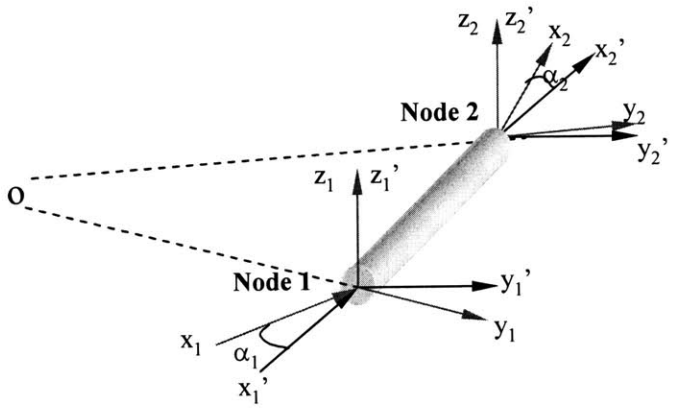

Figure 2-2 Coordinate transformation

The finite element formulae for all beam elements are assembled into one formula and the final finite element equation for the entire ring is:

$$KU = S + S_I \tag{2.3}$$

For each node, there are six DOFs. If a ring is discretized into N nodes, the total number of DOFs is 6N. Therefore, the displacement U and load S and S_I are all 6N×1 vectors, and the stiffness matrix K for the entire ring is 6N×6N. Equation (2.3) is thus in fact a set of 6N linear equations. There are usually m boundary conditions, which means m out of 6N DOFs are known and correspondingly m out of 6N loads are unknown. Therefore, the total number of unknowns is 6N and the governing equations can be solved in closed-form. If both DOFs and loads are unknowns, additional relations between DOFs and loads are needed in order to close the governing equations, for instance the asperity contact model that will be introduced later. Matrix K is symmetric and banded, which enables very efficient numerical procedures.

2.2.2 Conformability Calculations

Different applications need different ring/bore contact pressure distributions that are achieved by using different ring free shapes. For a ring with a symmetric cross-section (called symmetric ring hereafter), ring/bore contact pressure is related only to the displacement in the ring plane since there is no twist displacement. For a ring with an asymmetric cross-section (called asymmetric ring hereafter), however, the ring/bore conformability is also affected by the twist displacement. There are various ways to calculate the ring/bore conformability. The calculation procedure used in this study, applicable to both symmetric rings and asymmetric rings, consists of two stages. The first stage is to force the ring to coincide with a nominal circular bore, and this stage is the same for both types of ring. The second stage considers the realistic constraints applied on the ring. An asperity contact model is applied to ring/bore conformability calculation for symmetric rings in the second stage. For asymmetric rings, in addition to the ring/bore asperity contact models, the axial constraint is applied.

Stage One: Fitting the Ring to a Circular Bore with Consideration of the Large Displacement Issue

The change of the shape of a ring from its free state to the inserted state is quite significant. To meet the small displacement requirement of the FEA, special attention has to be paid to the large displacement issue. The step-by-step method that is widely used in FEA to solve large displacement problem is adopted in this study. Because the ring free shape is normally symmetry and the bore is circular, the analysis hereafter will be conducted on half of a ring.

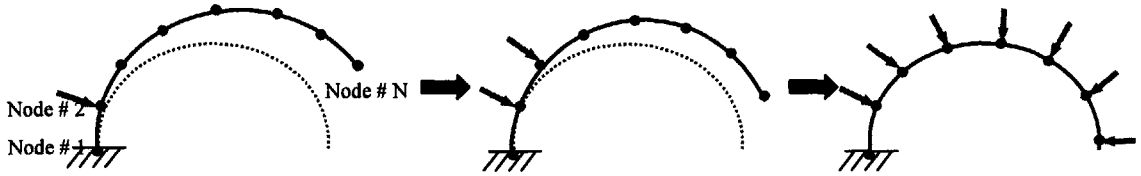

Figure 2-3 Step-by-step procedure of fitting a ring to a circular bore

Figure 2-3 illustrates the step-by-step procedure developed in this study. The solid line with nodes is the ring, and the dotted line denotes a nominal circular bore. At the beginning, the node at the back point (node #1, opposite to gap) is fixed at a point on the virtual bore. The constraints (boundary conditions) applied to the nodes are as follows: because of the symmetry, node #1 is prevented from displacing in all the direction (six constraints); for other nodes, only axial displacement and twist angle are constrained. The reason to do this is mainly for numerical convenience when dealing with asymmetric rings (symmetric rings do not have axial displacement and twist angle displacement).

The above constraints are applied consistently throughout the entire calculation process, while, at each calculation step, new constraint in the radial direction will be added.

At step one, node #2 is compelled by a radial force to move to coincide with the bore, while node #1 is fixed and the other nodes are free to move in the ring plane. The radial displacement of node #2 is determined according to its initial and final positions. This known radial displacement of node #2, plus those zero-displacement constraints applied to all the nodes can be viewed as boundary conditions. The stiffness matrix is evaluated based on the ring free shape. FEA resolves the reaction forces and moments for the constrained DOFs as well as the displacements for unconstrained DOFs of all the nodes. The stiffness matrix is then recalculated according to the updated ring shape, and the reaction forces and moments are saved as the initial loads for step two. With all of the old constraints maintained, a new constraint is applied to node #2 in the radial direction at this step.

At step two, node #3 is forced to coincide with the bore. The radial displacement of node #3 is determined based on its position at the end of step one and current position. FEA computes the reaction forces for constrained DOFs and the displacement for unconstrained DOFs for all of the nodes. Once again, stiffness matrix is recalculated according to the updated ring shape, and the reaction forces and moments are saved as the initial loads for the next step. The same procedure iterates for all nodes one by one, until eventually all of the nodes coincide with the bore.

Stage Two for Symmetric Ring: Ring/bore Asperity Contact Analysis

At the end of stage one, the radial reaction forces at some nodes may be pointing outward, which is not practically true in the situation when a ring is fitted into the bore. In stage two, all of the radial loads artificially applied in stage one are released and the interaction between the ring and the bore is investigated. To study the contact between the ring and the bore, complementarity analysis is usually conducted [7]. In this study, however, asperity contact analysis is implemented for the first time, and it proves to be more efficient and more robust. To conduct asperity contact analysis, FEA is performed again, based on the ring shape at the end of stage one and with the reaction forces set to be the initial loads. The following finite element equation that is similar to Equation (2.3) is applied:

$$KU = S(U) - S_I \tag{2.4}$$

where $S(U)$ relates the load vector S with the displacement vector U, and S_I is the initial load vector. For symmetric rings, the force on each node is in the radial direction and its value is (for *ith* node)

$$s^i_{rad} = \int_{running\ face} P_c[h_{liner}(u^i_{rad}, x)]dx \tag{2.5}$$

where P_c is the contact pressure between the bore and any point on the ring running-surface, and is a function of the clearance between the point and the bore h_{liner} The clearance h_{liner} is in turn a function of the radial displacement of the *ith* node u^i_{rad} and the axial location of the point on the running-surface x. An asperity contact model is employed to calculate the contact pressure P_c. As will be described, the asperity contact pressure is a nonlinear function of the clearance. Therefore, Equation (2.4) is a set of nonlinear equations. Newton's method is used to solve these equations. Because the ring/bore radial force is only a function of the ring/bore clearance that is determined by the radial displacement, the Jacobian matrix in Newton's method is still symmetric and banded, which enables very efficient numerical approaches.

Stage Two for Asymmetric Ring: Ring/bore and Ring/groove Asperity Contact Analysis and Static Twist Calculation

If the ring cross-section is asymmetric, at the end of the stage one, there are forces and moments that maintain the constraints, namely, all the forces and moments on node #1, the radial forces and the twist moments on the other nodes. These constraints are artificially applied and therefore should be removed. Once the artificial loads are removed, the ring cross-section will twist and lift, and the ring will have interactions with the bore and groove. The so-called static twist is an important ring parameter and should be determined in the design process. However, the magnitude of the static twists largely depends on the axial constraints applied to the ring.

Figure 2-4 Different constraints for twist measurement: (a) Fix Lower OD, (b) Fix Lower ID

Axial constraints that are similar to those used in practical measurement of static twist are shown in Figure 2-4a and Figure 2-4b, where one vertex of the cross-section, either lower OD (outer diameter) or lower ID (inner diameter) depending on the sign of asymmetric angle, is fixed in the

axial direction, while the centroid is allowed to move upwards. An equation similar to Equation (2.4) is applied to resolve the displacements. If the twist angle at every node is taken as a DOF, the axial lift should not be considered as a DOF anymore since it can be determined by the twist angle. The ring/bore contact force is related not only to the radial displacement, but also to the twist angle at every cross-section. Meanwhile, the twist moment is related to both radial force and axial force.

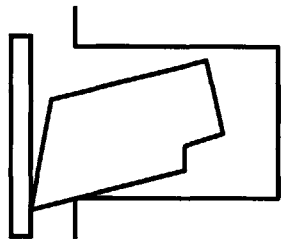

Figure 2-5 Groove constraint

There is another type of constraint that is more relevant to real engine applications. As sketched in Figure 2-5, the upper and lower groove flanks provide the axial constraints. After all the artificial loads applied at stage one are removed, the ring interacts with the bore and groove. Ring cross-sections may touch the groove upper flank or/and lower flank. The displacements can still be resolved by Equation (2.4), where the ring/bore contact force at *ith* cross-section is related to the radial displacement u^i_{rad} and twist angle u^i_{twist} at this cross-section through the following expression:

$$s^i_{rad} = \int_{running\ face} P_c[h_{liner}(u^i_{rad}, u^i_{twist}, x)]dx \tag{2.6}$$

Similarly, the axial forces from both upper and lower groove flanks are related to both the axial displacement u^i_{axial} and twist angle u^i_{twist}, while the twist moment is related to twist angle, radial displacement and axial displacement:

$$s^i_{axial} = \int_{upper} P_c[h_{groove}(u^i_{axial}, u^i_{twist}, x)]dx + \int_{lower} P_c[h_{groove}(u^i_{axial}, u^i_{twist}, x)]dx \tag{2.7}$$

$$\begin{aligned} s^i_{twist} = & \int_{running\ face} P_c[h_{liner}(u^i_{rad}, u^i_{twist}, x)]xdx + \int_{upper} P_c[h_{groove}(u^i_{axial}, u^i_{twist}, x)]xdx \\ & + \int_{lower} P_c[h_{groove}(u^i_{axial}, u^i_{twist}, x)]xdx \end{aligned} \tag{2.8}$$

where the h_{groove} is the clearance between any point on the ring's upper or lower side and the groove flanks. The Jacobian matrix in Newton's method that is employed to solve the set of nonlinear equations is more complex in this case than in the case of the symmetric ring. Nevertheless, the Jacobian matrix is still symmetric and banded.

2.2.3 Bore Distortion Consideration

The calculation of the conformability between a ring and a distorted bore is performed after the ring is inserted into the circular bore, along with the asperity contact analysis. Since the bore distortion is not symmetric, and even with symmetric bore distortion, depending on where the ring gap is located, the conformability between the ring and the bore can be asymmetric. As a result, the calculation cannot be conducted on half of the ring anymore. To calculate the conformability between a ring and a distorted bore, the loads applied on the half ring after the ring is inserted into the circular bore are assigned to the other half. In asperity contact analysis, bore distortion is taken into account in a straightforward way when the ring/bore clearance is estimated.

2.2.4 Modeling Ring Lapping Process

In this work, it was recognized that the analysis of the ring/bore interaction requires consideration of two length scales, namely, the deviation of the radius of ring free shape from the bore radius, whose magnitude is in the order of a millimeter, and the face profile whose magnitude is in the order of micrometers. One may never obtain the targeted contact distribution between a ring and a bore if the face profile is not well controlled because the contact or lubrication forces between the ring and the liner are very sensitive to the ring/liner clearance. A difference in clearance of few microns can change the contact patterns completely.

In reality, control of the ring free shape and ring face profile to micrometer level accuracy is often achieved by lapping the ring at the final step of the manufacturing process. The lapping process involves putting a stack of rings into a bore with the nominal bore size of the engine and then forcing either the bore or the rings to move axially back and forth to form the final face shape. After lapping, the rings are inspected and are only considered to be qualified if the inspectors see shiny contact signs on the ring surface all around the circumference.

It is important to simulate the lapping process for several reasons. First, this analytical tool for ring design is not complete if this important process is not included. Second, examining the face profile before and after lapping and comparing with the model prediction can give us a verification of the model prediction. Third, after establishing the confidence in the model prediction on lapping, the

model can be incorporated in the design process to a greater extent. Finally, for the subsequent modeling work to be conducted by the authors on the ring dynamics and lubrication in a distorted bore, it is crucial to use not only a realistic free shape but also the face profile.

The lapping process is simulated by using a simplified wear model in which the wear rate of the ring running-surface in the radial direction is proportional to the contact pressure between the ring and the bore. The face evolution is then calculated step by step using first order explicit scheme. With set criteria for the end of the lapping process, the simulation predicts the final lapped face profile along the circumference. Both symmetrical and asymmetrical ring cross-sections are considered in modeling the lapping process. As expected, ring twist affects the final lapped face profile significantly.

2.2.5 Modeling the Effect of Thermal Stresses

Piston rings producing tip contact concentration under thermal stresses was first studied by Mierbach [32]. In general, during engine operation, the temperature increase of the ring is higher at ring ID than at ring OD, and the temperature difference tends to decrease the curvature of the piston ring. As a result, high contact pressure and thus heavy wear usually occurs around the ring tip. In this study, the ring temperature was assumed to vary only along the ring radial direction and the temperature variation along the circumference was neglected. The effect of thermal stresses on ring shape is equivalent to the effect that would result from applying a bending moment on the ring tip in the axial direction, which in this study is called "thermal moment".

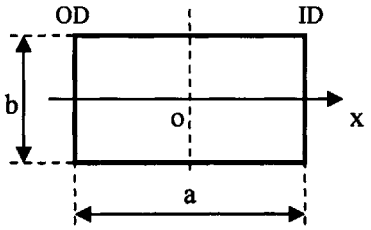

Figure 2-6 Coordinate of the ring cross-section with rectangular shape

For a ring with a rectangular cross-section shown in Figure 2-6, the thermal moment caused by the non-uniform temperature change can be calculated by the following formula

$$M_t = \int_{-\frac{a}{2}}^{\frac{a}{2}} x\alpha\Delta T_x Ebdx \tag{2.9}$$

where ΔT_x is the temperature change compared to the design temperature at location x along the radial direction, α the thermal expansion coefficient, and E the Young's modulus. A linear temperature distribution is assumed along the ring radial direction in this study and the resultant thermal moment is

$$M_t = \frac{1}{12}\alpha E b a^2 (\Delta T_{ID} - \Delta T_{OD}) \tag{2.10}$$

where ΔT_{ID} and ΔT_{OD} are the temperature changes at the ID and OD, respectively.

2.2.6 Free Shape Calculation (for Symmetric Rings)

The reverse procedure of the conformability calculation is employed to calculate the ring free shape if the contact pressure distribution is specified. Before the calculation, specified radial forces are applied to all of the nodes. As shown in Figure 2-7, forces are removed one by one, starting from node #N all the way to node #2. After each removal, ring shape and reaction forces are updated and the new stiffness matrix is calculated. By the time the force applied on node #2 is removed, the ring shape is considered to be the sought final free shape.

This procedure can be applied to an arbitrarily assigned contact pressure distribution. As long as the specified load at the beginning is self-balanced, which is physically required, the calculated free shape can produce the desired contact pressure distribution once it is inserted into the bore.

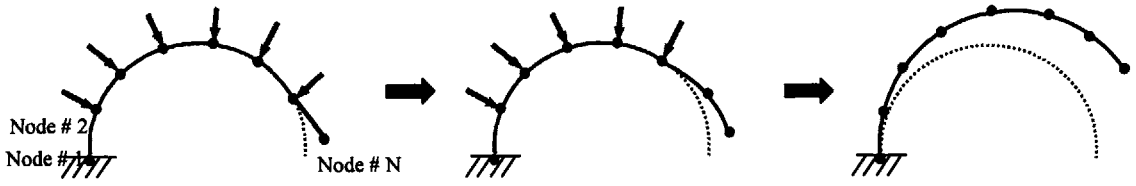

Figure 2-7 Step-by-step procedure of free shape calculation

2.2.7 Ovality calculation

In ring manufacturing, the "ovality" is usually used to characterize the ring/bore conformability around the ring tips. To measure the ring ovality, the ring is fitted into a flexible band and the band shrinks until the ring gap is closed. The difference between the diameter in the axis passing the back

point and the closed gap point, and the diameter in the perpendicular direction is defined as the ovality. To calculate this parameter, the measurement process should be simulated. Assuming contact pressure between the flexible band and the ring is uniform along the circumference, to model this case, we can remove all of the forces artificially applied on the ring at the end of stage one of ring/bore conformability calculation, and then apply uniform forces with magnitude that can yield the same tangential load as that provided by the artificial forces. By doing so, the ring gap may not be closed, or the two gap tips may overlap. Therefore, the magnitude of the uniform force has to be adjusted gradually until the gap is just closed. Once the gap is closed, the ovality can be calculated according to the positions of the node points on the ring.

2.2.8 Asperity Contact Model

As mentioned in previous sections, the forces between a ring and a bore, and between a ring and a groove flank, are assumed to be generated by asperity contact. An asperity contact model is therefore needed. For this specific application, an approximate formula that relates the contact pressure with clearance and roughness is sufficient. For computational convenience, the fitting formula from Ref. [29] based on the Greenwood & Tripp's theory [33] was used for rough surfaces whose roughness heights have a Gaussian distribution:

$$P_c = \begin{cases} 0 & h/\sigma > 4 \\ K_c(4 - \frac{h}{\sigma})^z & h/\sigma < 4 \end{cases} \tag{2.11}$$

where P_c is the contact pressure, σ is the combined surface roughness, h is the nominal clearance between the ring running-surface and the bore or between the ring side and the groove flank, K_c is a coefficient that depends on asperity and material properties of the rings and the bore, and z is a correlation constant.

2.3 Sample Results

Several examples are given in this section to demonstrate the capabilities of this analytical tool. Except the bore distortion case, all of the calculations were conducted by using 180 nodes. The circumferential location, from gap to back point, is labeled from 0 to 180 degrees in the figures. The sign convention for the twist angle and groove tilt angle is as follows: the angle formed by ID moving up and OD moving down is negative. The definitions of the cross-section parameters are illustrated in Figure 2-8, where the principle angle shown is negative.

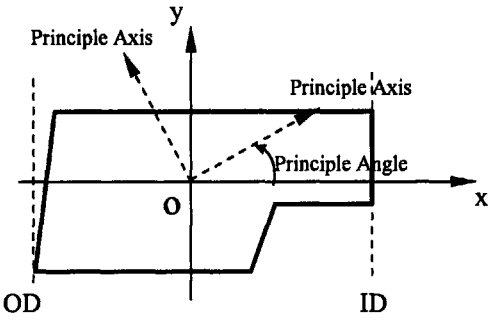

Figure 2-8 Definition for parameters of ring cross-section

2.3.1 Conformabilities of the Second Ring in a Heavy-Duty Diesel Engine

The first ring (ring #1) used to demonstrate the capabilities of the tool is the second compression ring of a heavy-duty diesel engine. The main parameters describing the ring are listed in Table 2-1. The ring cross-section has a cut at the lower ID and therefore has a negative principle angle. As a result, the ring has negative static twist angle once it is compressed.

Table 2-1 Parameters of ring #1

Young's Modulus	130 GPa
Bore Size	131 mm
Moment of Inertia	I_{xx}= 28.43 mm^4 I_{yy}= 9.98 mm^4
Torsional Factor	J = 23.72 mm^4
Principle Angle	-9°
Tangential Load	28.6 N

The "Fix Lower OD" calculations were conducted under the conditions with and without lapping process. The lapping calculation was stopped when the maximum clearance between ring and bore was less than two times the combined roughness (0.3μ). The distributions of ring/bore contact pressure before and after the lapping process are shown in Figure 2-9. It can be seen that, before lapping, the ring does not conform to the bore around the ring tip. The lapping process causes the ring to conform the bore around the entire circumference, and makes the contact more uniform. A plot of the lapped radial thickness on the running-surface of the whole ring is shown in Figure 2-10, where 0 in the "Axial Location" axis is the lower edge of the ring running-surface and the gap location is slightly away from the zero in the "Circumferential Location" axis. From Figure 2-10, one can also determine the length along the ring face axial direction to which the wear reached due to the lapping.

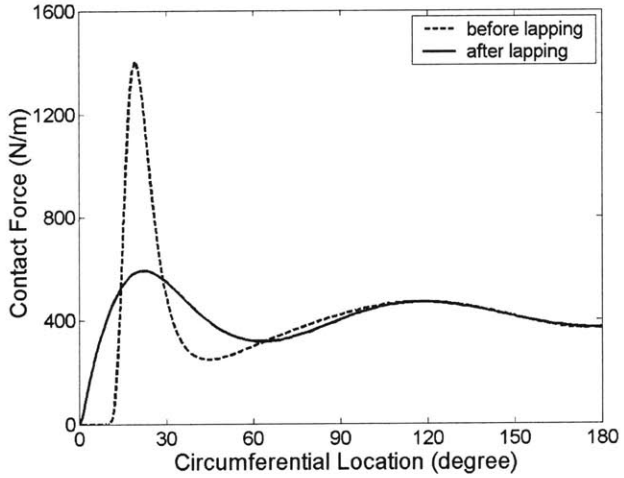

Figure 2-9 Ring/bore contact force distribution of ring #1 before and after lapping

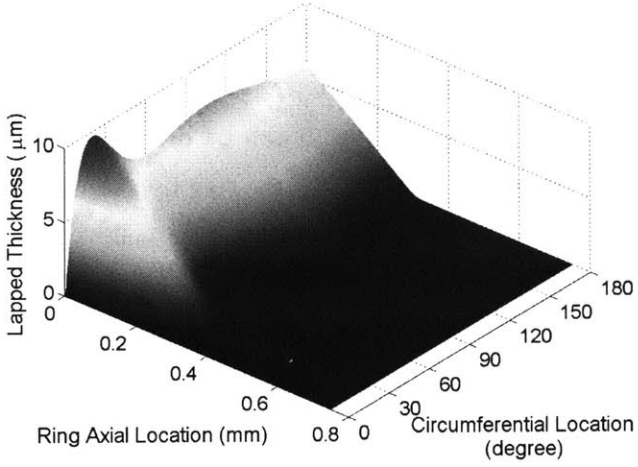

Figure 2-10 Lapped thickness on the running-surface

Conformability analysis was also performed under the groove constraint condition. The corresponding piston groove has negative tilt angle of 0.2 degrees due to thermal deformation of the piston. The calculated static twist angle distribution is depicted in Figure 2-11, where the measured wear angle at the ring running-surface after 1500 hours test is shown as well. The calculated twist angle distribution exhibits the similar trend as that of the measurement. Moreover, the calculated results show good agreement with measurements in terms of their magnitude.

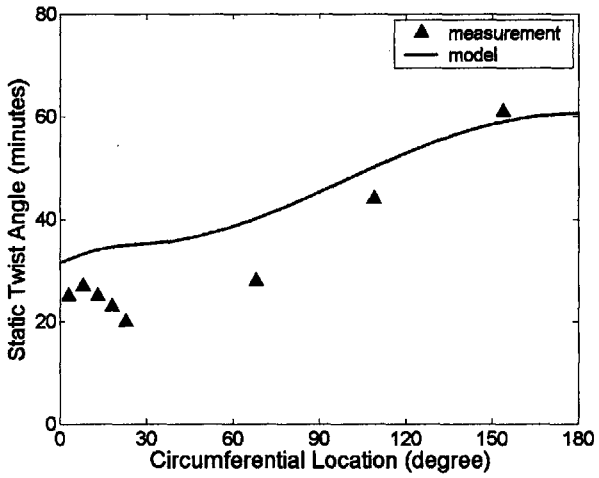

Figure 2-11 Static twist angle of ring #1

When an asymmetric ring is compressed under the groove constraint, in addition to the radial displacements on all cross-sections, there are twist angle and axial lift displacements. The twist angle and axial lift vary with the height of the groove. For demonstration purposes, ring #1 was inserted into an unrealistic groove with large height, which allows the ring/groove clearance to be 1mm. Figure 2-12 shows the 3D shape of the ring after being inserted into the bore and groove configurations, with twist angle and axial lift enlarged by 20 times. It can be detected that the centroids of the ring cross-sections do not remain in a single plane, with the ring tip and back point having higher lifts. Accordingly, these two locations contact the upper groove flank, while somewhere in-between contacts the lower flank. In the real piston groove configuration, the 3D shape of the ring and its interaction with the groove are similar to what is shown in Figure 2-12. Since the ring under investigation has a larger negative twist than the groove tilt, all of the contact occurs at the upper ID or lower OD.

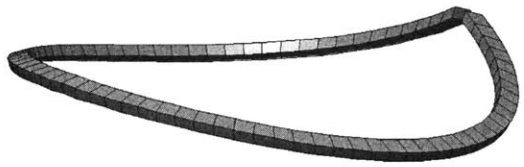

Figure 2-12 3D shape of compressed ring with axial lift and static twist angle (twist angle and axial lift are enlarged by 20 times)

2.3.2 Ring/Groove Interactions under Dynamic Loading

Using this design tool, one can carry out preliminary studies on the interaction between a ring and its groove under dynamic loading. In engine operating conditions, the inertial force, friction and gas pressure play key roles in determining the ring's dynamic behavior. In this tool, all of the forces can be specified as external axial forces acting on the centroid of ring cross-sections plus some necessary twist moments. Under the impact of the axial force, the ring can be pushed up or down, and ring upper or lower sides will make contact with the groove flanks. This model is capable of providing information such as where the ring is contacting the groove and how intense the contact pressure is. This would be helpful for ring designers in the design process and also for engineers to perform wear analysis. Using the wear measurements and model results for the ring #1, the following analyses were carried out to illustrate the capability of the model. All of the comparisons were conducted for the most severe contact between the ring and the piston groove. Although friction and gas pressure also play key roles in ring dynamics, they were not considered in the analysis due to the fact that the maximum contact force between the groove and the second compression ring with negative static twist is mainly determined by inertial force.

Corresponding to the maximum engine speed of 2300RPM in the engine testing cycle, the maximum upward inertial force on the second ring is about 224N. With this axial force applied on, the ring is pushed up and a greater portion of the ring upper side touches the groove upper flank. Figure 2-13 shows the contact force between the ring upper ID and the groove upper flank. It needs to be pointed out that the entire upper ID edge touches the groove, even though the contact forces at some locations are too small to be discerned in the figure. The dynamic contact pressure can cause wear, especially on the tip location where the contact is most intense. The photo of the wear pattern of the ring upper side close to the tip is shown in Figure 2-14, from which the most severe wear can be observed at the ID of the ring tip. Wear was also found at the upper ID of other portion, with lower intensity than that at the tip. It can be concluded that the model results well reflect the wear pattern.

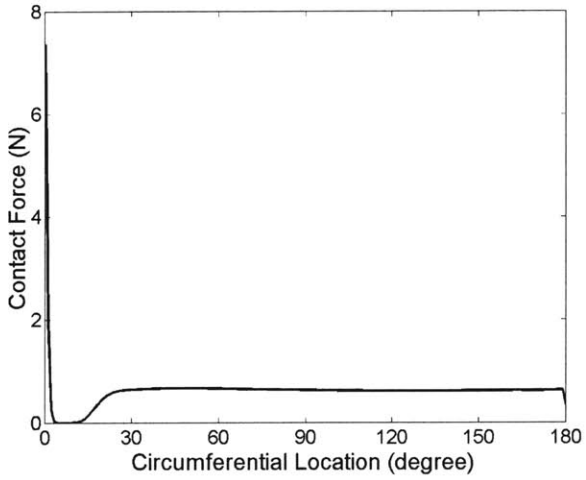

Figure 2-13 Upper ring/groove contact force under the influence of the maximum upward inertia force

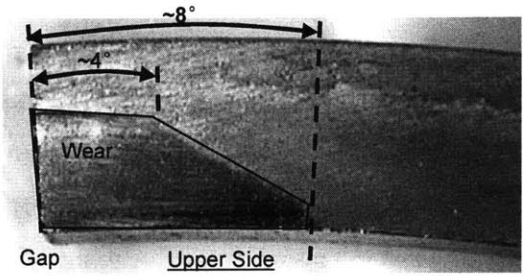

Figure 2-14 Photo of the wear pattern of ring upper side

The maximum downward inertial force at the 2300RPM condition is about 125N. Corresponding to this force, the calculated contact force between the lower OD edge of the ring and the lower flank of the groove is depicted in Figure 2-15. Most of the ring touches the groove except the portion close to ring tip. Given that this calculation is conducted under the condition of maximum downward inertial force, it can be concluded that the portion close to tip will never touch the groove lower flank and thus the wear should not be found underneath it. Figure 2-16 shows the wear photo of the ring lower side around the tip and wear was not detected until eight degrees from the tip. Although the exact location of the start point of the wear does not match the start point of the contact force in the model results, they do exhibit the same no-contact phenomenon around the ring tip. The discrepancy is mainly caused by the fact that the original ring without wear was used in the model calculation. The

no-contact phenomenon around ring tip may be undesirable in ring design since it means gas and oil leakage. To avoid it, parameters of ring cross-section such as principle angle should be chosen carefully, and the analytical tool developed in this study can be used to estimate the ring/groove conformability in the ring design process.

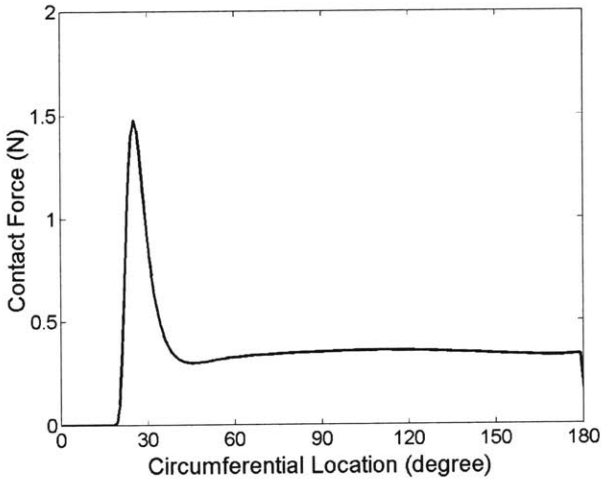

Figure 2-15 Lower ring/groove contact force under the influence of the maximum downward inertia force

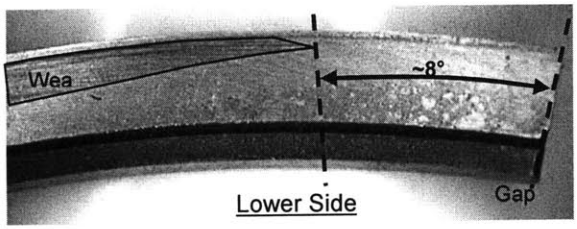

Figure 2-16 Photo of the wear pattern of ring lower side

The twist angle distributions under both extreme conditions tested above are plotted in Figure 2-17, where one can see that the twist angle decreased compared to that of the static condition, also shown in this figure. Meanwhile, the magnitudes decreased uniformly along the ring circumference. It can be conclude that the dynamic twist is almost uniform along the ring circumference.

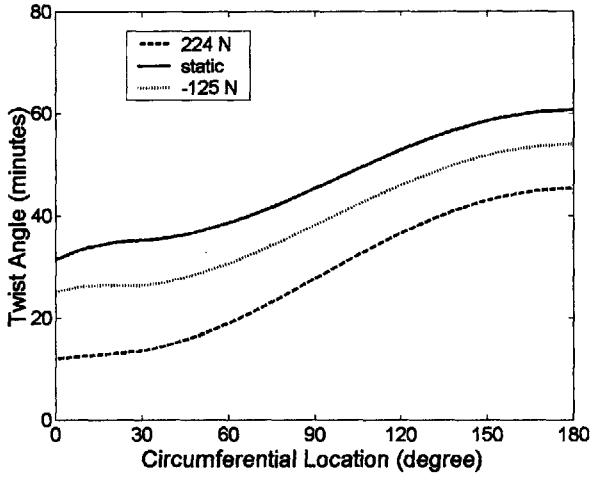

Figure 2-17 Twist angles of ring #1 under the influence of inertia forces

Table 2-2 Parameters of ring #2

Young's Modulus	130 GPa
Bore Size	90 mm
Moment of Inertia	$I_{xx} = 10.67\ mm^4$
Tangential Load	14 N

2.3.3 Ring Free Shape Calculation

A symmetric ring (ring #2), of which the key parameters are listed in Table 2-2, was used to demonstrate the free shape calculation. A uniform contact pressure distribution and a sinusoidal contact pressure distribution were specified, and the calculated free shapes at the axis passing through the centroids of all cross-sections are shown in Figure 2-18. In order to prove that these shapes can give the desired contact pressure distributions, the conformability calculations were performed and the contact pressure distributions are sketched in Figure 2-19. According to the method used in the free shape calculation, it is possible to calculate any contact pressure distribution for any bore shape. For example, a free shape can even be computed to give a uniform contact pressure distribution for a distorted bore.

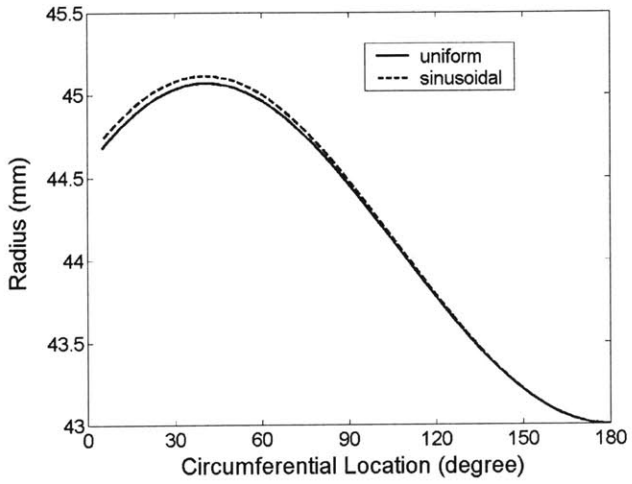

Figure 2-18 Free shapes for uniform and sinusoidal tension distributions

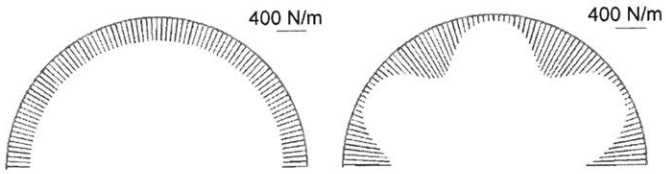

Figure 2-19 Calculated uniform and sinusoidal tension distributions for calculated ring free shapes

Table 2-3 Parameters of bore distortion

Order	2^{nd}	3^{rd}	4^{th}
Magnitude (μm)	30	20	5
Phase (degree)	30	60	90

2.3.4 Bore Distortion and Ring Conformability

Bore distortion and its impact on the oil consumption has always been a subject of intensive investigation. It is crucial for the ring designer to estimate the conformability between the ring and the distorted bore. This design tool can be used for arbitrary bore shapes. Here, a bore shape with up to fourth order distortion that is generated by the following equation is used for illustration:

$$dB = \delta_2 \cos[2(\theta + \alpha_2)] + \delta_3 \cos[3(\theta + \alpha_3)] + \delta_4 \cos[4(\theta + \alpha_4)] \qquad (2.12)$$

where, dB is the change in bore radius, θ the circumferential location (with a value of 0 at the ring gap location), δ_i the magnitude of the *ith* order bore distortion, and α_i the corresponding phase angle relative to the gap location. The 0^{th} and 1^{st} orders are not included in the expression because the 0^{th} order bore distortion is simply a uniform expansion or shrinkage in the bore diameter and the 1^{st} order is just a shift of the center. The magnitudes and phase angles used in this study are shown in Table 2-3. Ring #2 with uniform contact pressure distribution, of which the free shape was calculated previously, was used for this calculation. The calculated ring/bore contact force and clearance distributions are sketched in Figure 2-20, with the distortion magnitude enlarged by 200 times. Under this bore distortion and ring tension, the maximum clearance between ring and bore is as high as 17μm.

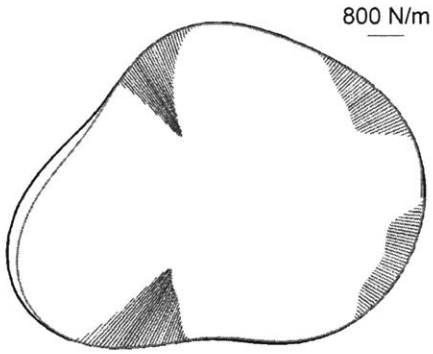

Figure 2-20 Ring conformability with distorted bore (distortion enlarged by 200 times)

From the structural point of view, there are two crucial parameters for ring/bore conformability, namely the tangential load and the bending rigidity (EI, Young's modulus times moment of inertia). Higher tangential loads and smaller bending rigidities give better conformability. If the ring material is determined, the bending rigidity changes with the moment of inertia of the cross-section. Figure 2-21 shows, for the bore characterized in Table 2-3, a map of ring conformability using rings with various combinations of tangential load and moment of inertia. The conformability in the figure was quantified as the maximum clearance between the ring and the bore. Compared to a ring with a certain tangential load and a certain moment of inertia, a ring with lower tangential load and smaller moment of inertia may give the same conformability. Alternatively, a ring with the same tangential load but with smaller moment of inertia can provide better conformability. This mechanism is important for ring designer to determine the key parameters of the ring in order to achieve specific goals, such as reducing friction while maintaining the same conformability, or enhancing the conformability without increasing the ring tension and thus the friction.

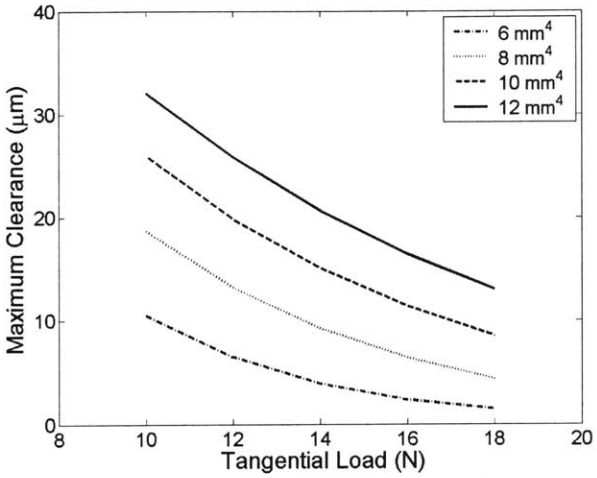

Figure 2-21 Map of ring conformability

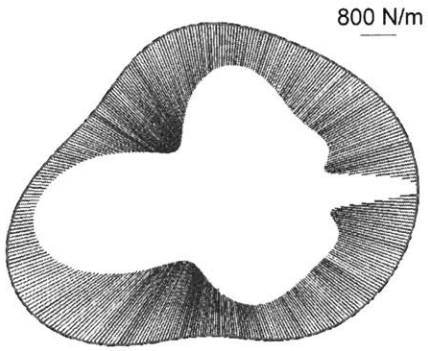

Figure 2-22 Ring conformability with distorted bore under gas pressure effect

Another crucial factor affecting ring conformability is the gas pressure during engine operation. The gas pressure effects on ring conformability are perhaps most pronounced for the top ring, as it is directly exposed to the combustion pressure. To illustrate the gas pressure effects, a net pressure of 5bar was applied to the back of the ring for the case shown in Figure 2-20. The contact force between the ring and the distorted bore is plotted in Figure 2-22. It can be seen that the ring makes contact with the distorted bore along the entire circumference under the influence of the gas pressure. Furthermore, this example shows the profound implication on the bore distortion effects on oil consumption as explained in the following. The ring/bore conformability without the pressure effects, shown in Figure 2-20, can be considered as the case in the intake stroke of an engine cycle. The reduced

conformability of the ring may allow large amounts of oil, if available, to pass the top ring and to stay on the cylinder liner during the intake stroke. During the compression stroke, the ring conforms completely to the bore under the influence of the gas pressure. As a result, the excessive oil left on the liner during the intake stroke may be scraped up by the top ring. The scraped oil accumulates on the upper side of the ring and part of it may flow to the crown land and directly contribute to oil consumption. Therefore, the difference between the ring conformability during the intake and compression stroke may be considered as one of the main mechanisms causing higher oil consumption with larger bore distortion, as discussed by Tian [4].

Table 2-4 Parameters of ring #3

Young's Modulus	168.5 GPa
Bore Size	105 mm
Moment of Inertia	$I_{xx} = 19.82\ mm^4$
Tangential Load	26.9 N
Thermal Expansion Coefficient	13×10^{-6} /C°

2.3.5 Thermal Stresses and Ring Tip Wear

The effect of thermal stresses on the ring/bore conformability was studied on the top ring of a diesel engine (ring #3), of which the key parameters are listed in Table 2-4. To compensate for the effect of thermal stresses, the ring was designed purposely to have lower contact pressure around the tip location. Even with this design, the ring still exhibits heavier wear around tip than the other portion after a certain amount of testing hours, and the cause was believed to be the effect of thermal stresses. Several values of the temperature difference between ring ID and OD (0°, 20°, 30°) were tested and the ring/bore contact pressure distributions are shown in Figure 2-23. It can be seen that under the effect of thermal stresses, the contact pressure around the tip location increased significantly. The high contact pressure around the ring tip would cause severe wear, which can be detected in the photo of wear pattern shown in Figure 2.24.

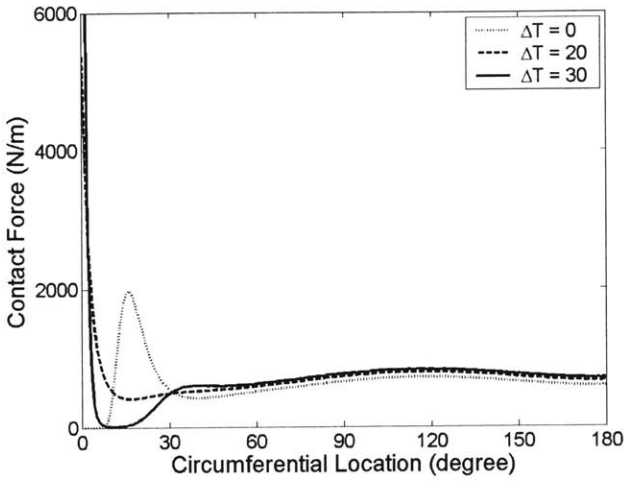

Figure 2-23 Thermal stress effect on ring/bore conformability

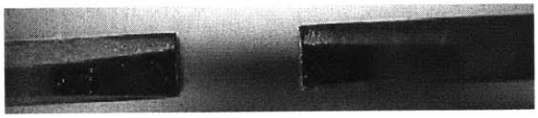

Figure 2-24 Wear pattern of ring running-surface

2.3.6 Heavy Contact around Ring Tip during Cold Start of Aluminum Engines

This analytical tool can also be used to study the ring/bore conformability under cold start conditions for aluminum engines. During engine cold start process, the environmental temperature is lower than the design temperature and the cylinder liner of the aluminum block shrinks more than the ring. Meanwhile, the piston temperature has not increased much and the temperature difference between the ring ID and OD is not profound. Therefore, the effect of thermal stresses is not a factor. In this study, ring #2 with uniform contact pressure distribution was inserted into bores with diameters smaller than the normal bore size (shrinking 20 μm and 40 μm), and the contact pressure distributions are shown in Figure 2-25. It can be seen that the contact pressure around the gap increased with bore shrinkage. As a result, severe wear and even scuffing could happen around the ring gap during engine cold start process.

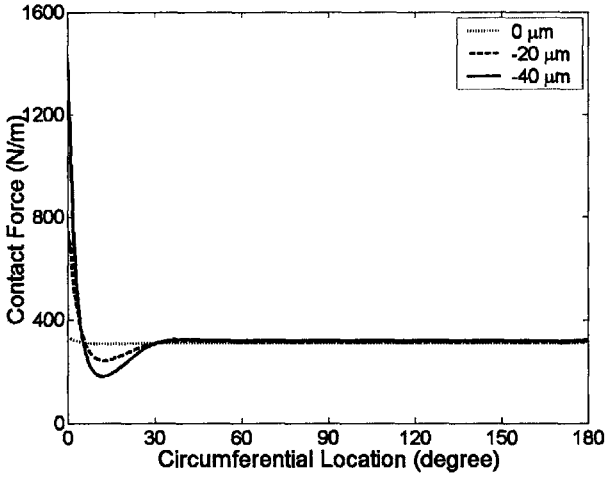

Figure 2-25 Bore shrinkage effect on ring/bore conformability

2.3.7 Ovality Calculation

The ovality calculation was tested on the top ring of a HD diesel engine (ring #4). Its key parameters are listed in Table 2-5. The calculated ovality is -0.247 mm, which agrees well with the measured value (-0.23 mm). The simulated shape of the ring inside the flexible band and that of the measurement are compared in Figure 2-26, and they match each other well.

Table 2-5 Parameters of ring #4

Young's Modulus	168.5 GPa
Bore Size	131 mm
Moment of Inertia	$I_{xx} = 32.94\ mm^4$ $I_{yy} = 12.38\ mm^4$
Torsional Factor	$J = 29.65\ mm^4$
Principle Angle	2.7°
Tangential Load	30.1 N

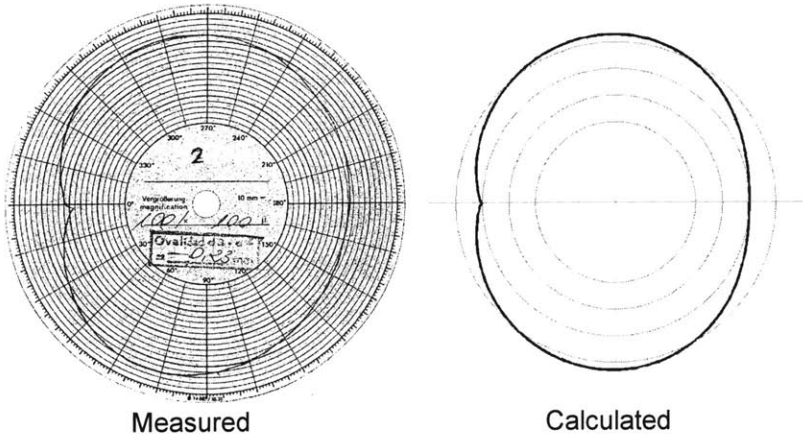

Figure 2-26 Ring shape inside the flexible band

2.3.8 Twist Chamfer Effects on Ring Static Twist

A ring with an asymmetric cross-section will have static twist angle when it is compressed and inserted into the engine. The asymmetric cross-section is usually made by cutting one of the two corners at the ID of a ring with rectangular cross-section shape, and as a result a chamfer is machined. The existence of the chamfer will induce the deviation of the principle axes of the cross-section from the ring axes, and at the same time reduce the moments of inertia of the cross-section. In a practical design process, the size of the chamfer is an important design parameter as to satisfy specific design purposes, such as to achieve static twist angle. To understand the effects of the chamfer size on the ring static twist, several cases were tested as following.

Table 2-6 Parameters of ring #5

Young's Modulus	130 GPa
Bore Size	131 mm
Moment of Inertia	$I_{xx} = 31.25\ mm^4$ $I_{yy} = 11.25\ mm^4$
Torsional Factor	$J = 28.17\ mm^4$
Tangential Load	30 N
Cross-section	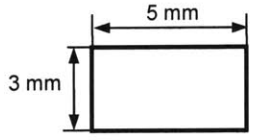

A ring originally with rectangular cross-section was chosen to conduct the study. Its key parameters are listed in Table 2-6. Its free shape that will generate uniform ring/bore contact pressure distribution was calculated by the model according to its tangential load. Several chamfers on the lower ID corner are designed through cutting isosceles right triangles with legs as 0.5mm, 1.0mm, 1.5mm and 2.0mm, respectively (as shown in Figure 2-27). The corresponding principle angles (defined in Figure 2-8) are -1.15, -4.03, -8.05 and -12.75 for chamfer 1, 2, 3 and 4, respectively.

The first study was conducted by using the same free shape as that of the original rectangular ring. The calculated twist angle distributions under "Fix Lower OD" condition are shown in Figure 2-28. It can be seen that the twist angle increases with the size of the triangle. The main reason behind this trend is that the magnitude of the principle angle increases with the size of the triangle cut.

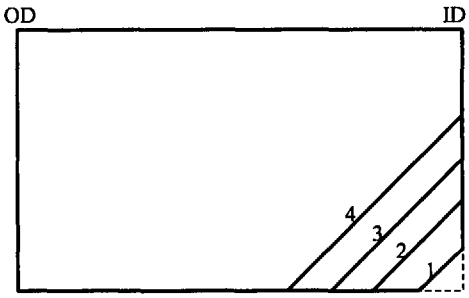

Figure 2-27 Ring cross-section shapes with different chamfer size

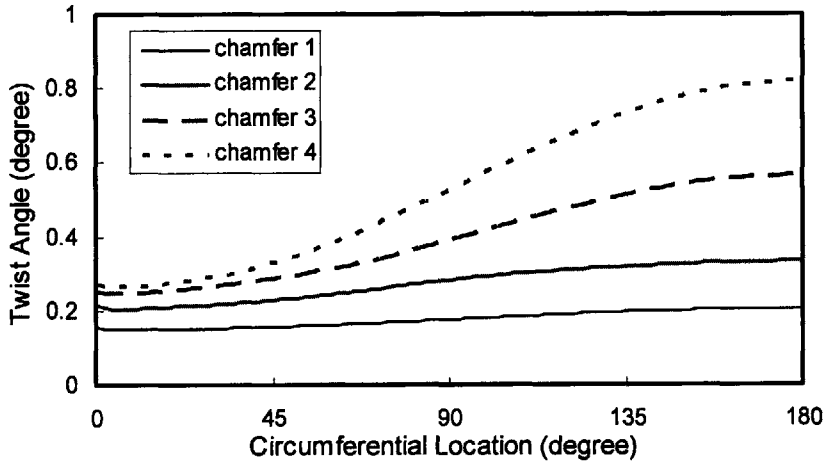

Figure 2-28 Ring twist angle distributions for rings with different chamfers and the same free shape

As a result of the cut, the tangential load of the ring changes and it decreases with size of the triangle (29.09, 26.99, 24.02, 20.40 N for chamfer 1, 2, 3, 4 respectively). In practical design, however, the change of the ring tension is not desired since the tension is one of the key parameters for leakage control. In order to maintain the same tension, the ring with a chamfer has to have a larger free shape. The twist angle distributions of the rings with different chamfer and free shape, but with the same tension, are shown in Figure 2-29. Compared to the case with the same free shape, the twist angle of the case with the same tension is greater.

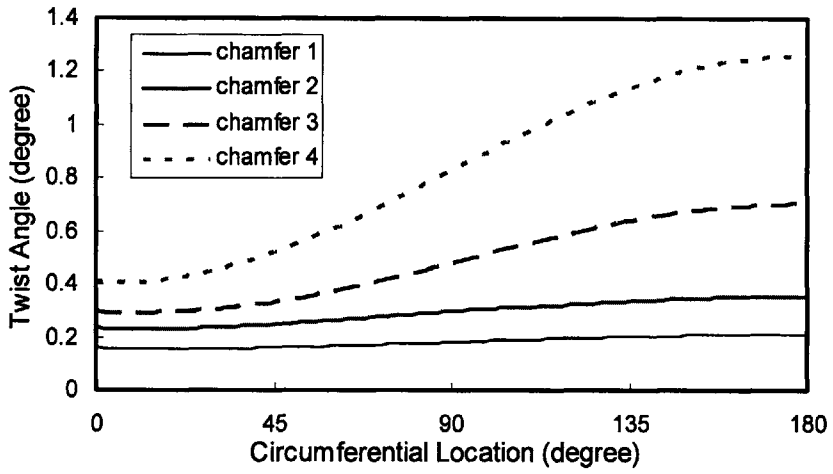

Figure 2-29 Ring twist angle distributions for rings with different chamfers and the same tension

2.4 Conclusions

The interactions between a single-piece piston ring and the cylinder bore as well as between the ring and the groove are complex 3-D phenomena. By employing 3-D finite beam element model and a physics-based asperity contact model, the analytical tool developed in this study is capable of addressing the structural complexities that arise from the interactions. The practical applications show that the model is robust and functional, and the predicted results agree well with the measurements. Therefore, this analytical tool can be integrated in the design process of the single-piece piston ring.

The complex interactions between a single-piece piston ring and the piston groove as well as between the ring and the cylinder liner, which were revealed by this study, play crucial roles in ring dynamics and ring lubrication. Most existing models for ring lubrication and dynamics that only simulate one cross-section of the ring are not capable of considering the variations along the ring circumference. Based on the numerical methodologies established and the confidence built in this study as how to deal with the ring structural analysis inside the power cylinder system, it is possible to develop 3-D models of the dynamics and the lubrication for piston ring pack, which are the foundations for numerical study of oil consumption, ring friction, ring wear and blow-by gas flow in internal combustion engines.

Chapter 3 Modeling Ring-Pack Dynamics and Gas Flow

3.1 Introduction

In this chapter, a three-dimensional model for ring dynamics and blow-by gas flow is developed to address non-axisymmetric characteristics of the power cylinder system. This model considers a typical piston ring-pack composed of two compression rings and a twin-land oil control ring, which is used in most diesel engines and some gasoline engines.

During an engine cycle, three rings move axially and radially under the influences of inertial force and gas pressure, and under the constraints imposed by the cylinder liner and piston grooves. In this model, ring is discretized into straight beam elements. The same 3-D finite element analysis used in the static analysis (Chapter 2) is employed to address the structural response of each ring to external loads. Physics-based sub-models are developed to simulate each ring's interactions with the piston groove and the liner. Gas flows driven by the pressure difference along both the axial and circumferential directions are modeled as well. Given the engine operating conditions, cylinder pressure and other information such as piston secondary motion and bore distortion, this model predicts the inter-ring gas pressure and both the linear and angular displacements of the three rings at various circumferential locations for every computation step. Other useful information, for instance the gas flow rate, the ring/liner and ring/groove asperity contact pressure, are also outputted.

In the following sections, the key elements of the model will be discussed first. Then, the model is applied to a heavy-duty diesel engine and emphases are given to the situations where the localized effects are important in understanding the overall ring dynamics and gas flows.

3.2 Model Development

3.2.1 Discretization of the System

The system is divided circumferentially into cross-sections. To facilitate the numerical process, the discretization follows the same pattern at all axial positions. Due to the presence of ring gaps, the system can not be evenly discretized in the circumferential direction. As shown in Figure 3-1, the locations around the ring gaps need to be treated differently. After the discretization process, the three rings are divided into straight beam elements, while the gas regions between the back of the ring and the groove, and between the cylinder liner and the piston land, are discretized into gas elements. The system variables at the intersection between the dashed line and the system in Figure 3-1 are the unknowns to be solved.

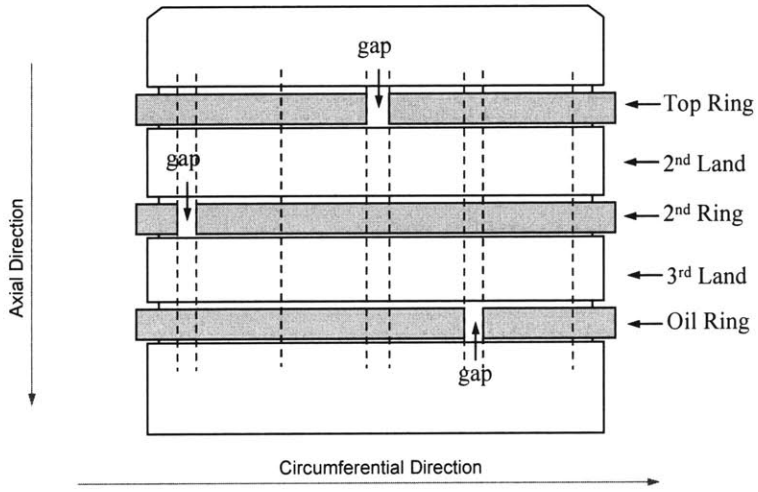

Figure 3-1 Discretization of system

3.2.2 Identification of the System Variables

Figure 3-2 sketches one cross-section of a power cylinder system. In addition to three rings, there are cavity regions surrounded by the rings, the liner and the piston. This 3-D model allows various dynamics behavior for different cross-sections and non-uniform gas pressure along the system circumference. The variables of the entire system are the circumferential extension of the variables in one cross-section as shown in Figure 3-2.

For each ring cross-section, six degrees of freedom (DOFs) can depict its dynamic behaviors, namely three linear displacements and three angular displacements as shown in Figure 3-3. If we assume that the temperature of the entire system does not change with time, the pressure is the only

variable for the gas inside one cavity region. Since gas pressure inside the crown land can be assumed to be equal to the cylinder pressure, and the pressure below the oil control ring is assumed to be the crank case pressure, there are only five gas regions to be investigated, which are denoted in Figure 3-2 as G1 ~ G5. Therefore, the number of variables in one cross-section as depicted in Figure 3-2 is 23. If the system is discretized circumferentially into N cross-sections, there are totally 23N variables.

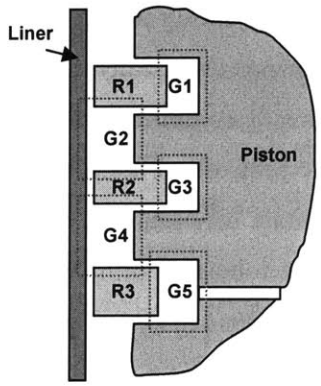

Figure 3-2 Sketch of a cross-section of the system

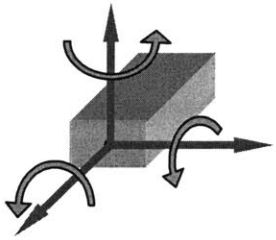

Figure 3-3 Degrees of freedom at ring cross-section

3.2.3 Force Analysis for Rings

A ring interacts with the gas, piston groove and cylinder liner. To model the ring dynamics, one has to simulate the forces and moments from all of the interactions. The ring surface can be divided into three kinds of regions: the interface between the ring and the groove flanks, the interface between the ring running-surface and the cylinder liner, and the portion of the ring surface which is exposed to various gas zones. The forces existing at the ring/groove interface and ring/liner interface are further illustrated below.

Ring/Groove Interface

Three types of force may exist at the ring/groove interface: gas pressure, oil pressure, and asperity contact force. When the ring is away from the groove flank and oil film, there is a pressure driven gas flow between the ring ID and OD. The corresponding pressure distribution can be calculated based on the assumption of fully developed, quasi-steady and locally-parallel flow (Poiseuille flow) [13]. When the ring is in contact with the oil film, the gas flow stops and the oil pressure is generated. Although oil squeezing and suction between the ring and the groove may have a significant impact on ring dynamics, simulation of these phenomena can greatly increase the calculation time and including such a complex sub-model inside the already complicated 3-D dynamics model is not realistic at the moment. In this study, only hydrostatic pressure of the oil is considered. As the ring moves even closer to the groove flank, asperity contact between ring and groove occurs, resulting in asperity contact force. By neglecting ring/groove relative motion in the radial direction, all of the forces existing between ring and groove are considered to be perpendicular to the ring surface.

Ring/Liner Interface

Similar to the ring/groove interface, the forces existing between the ring running-surface and the cylinder liner can be gas pressure, oil pressure and asperity contact force. As shown in Figure 3-4, if the oil is attached to the ring, the ring running-surface is divided into three regions. The force in the region where the oil attached to the ring can be calculated by a hydrodynamic lubrication sub-model. To avoid the complexity of detailed hydrodynamic lubrication at the moment, a simplified hydrodynamic lubrication model that will be described in Chapter 3.2.5 was developed to provide rational lubrication forces such as axial friction and radial supporting force. The radial forces applied on the other two regions can be estimated by the gas pressure P_1 and P_2. When the oil is not attached to the ring, only gas pressure acts on the ring running-surface, and the radial force due to the gas pressure can be calculated in a simplified manner analogous to that of ref. [18]: the ring running-surface is divided into two regions by the point that has minimum ring/liner clearance; above the minimum point, the pressure is assumed to be the same as that of the land region above the ring; underneath the minimum point, the pressure of the land region below the ring is assumed. When the ring touches the liner, in addition to the gas pressure and oil pressure, there are asperity contact force in the radial direction and the induced friction force in the axial direction. The asperity contact force is calculated by the asperity contact model described in Chapter 2.2.3., while the friction force is evaluated by multiplying the asperity contact force with a friction coefficient of boundary lubrication (0.1 is used in this study).

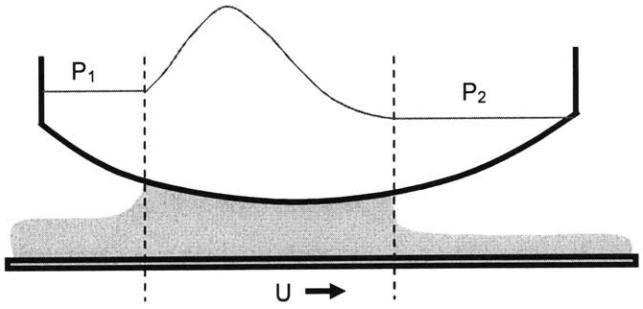

Figure 3-4 Pressure distribution in ring/liner interface

3.2.4 Gas Flow Analysis

In the power cylinder system, there are gas flows in radial, axial and circumferential directions due to the pressure difference between adjacent gas zones. The gas flows can be categorized into channel flow and orifice flow. As illustrated in Figure 3-5, the possible channel flow pathways include the clearance between the ring side and groove flank in radial direction, between the ring running-surface and the liner in axial direction, between the ring back and the groove in circumferential direction, and between the piston land and the liner in circumferential direction. While the gas flow through the ring end gaps can be considered as orifice flow. The modeling approaches for channel flow and orifice flow are described in Chapter 3.2.6 and 3.2.7, respectively.

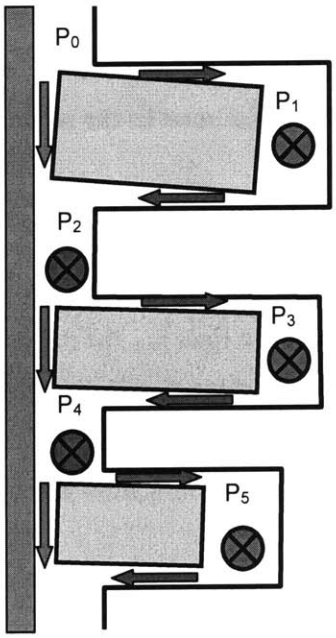

Figure 3-5 Possible channel flow pathways in the system

In this system, one gas zone is connected to several other gas zones, and the gas flow network needs to be well identified. For instance the gas zone between the piston second land and the liner in the ith cross-section, there are totally six possible gas flows that directly related to it (Figure 3-6): the non-conformability between the top ring the liner can induce the axial gas flow m_1; the non-conformability between the second ring and the liner will open the path for axial flow m_6; the clearance between the lower side of the top ring and its groove facilitates the radial gas flow m_2; the clearance between the upper side of the second ring and its groove allows the radial gas flow m_5; the gas zone of the second land at ith cross-section is connected to that of the (i-1)th and (i+1)th cross-sections, hence the circumferential gas flow m_3 and m_4 are always there.

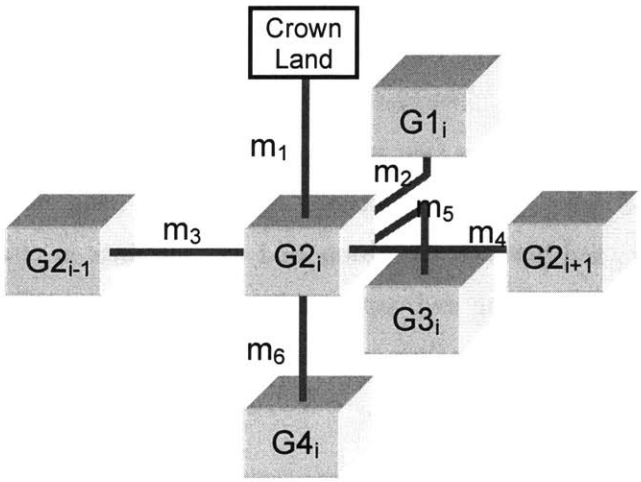

Figure 3-6 Gas flow network for the gas zone in the second land of the ith cross-section

3.2.5 Simplified Hydrodynamic Lubrication Model

The hydrodynamic lubrication between the ring and the liner is simplified to be the case shown in Figure 3-7. Given the oil film thickness on the liner h_{oil}, the region where the oil is attached to the ring running-surface is determined by the point where the ring has the minimum ring/liner clearance and the point at the leading half where the ring/liner clearance is $2h_{oil}$. Once the oil wetting region is found out, classical one-dimensional hydrodynamic lubrication theory can be applied to determine the corresponding lubrication forces.

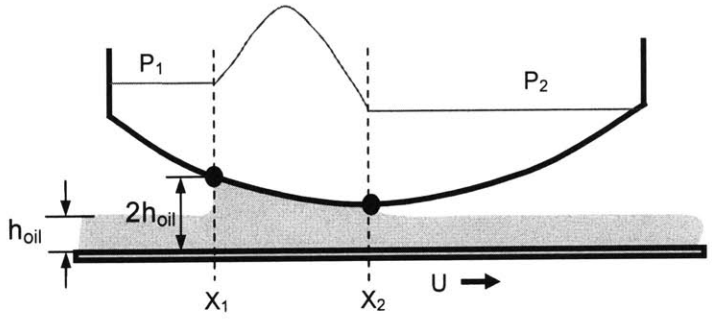

Figure 3-7 Simplified configuration of ring/liner lubrication

For a steady state hydrodynamic lubrication system shown in Figure 3-7, volumetric flow rate through a unit width of any section can be wrote as

$$q = -\frac{h^3}{12\mu}\frac{\partial p}{\partial x} + \frac{U}{2}h \tag{3.1}$$

Then the pressure gradient can be expressed as a function of the flow rate

$$\frac{\partial p}{\partial x} = \frac{12\mu}{h^3}\left(\frac{U}{2}h - q\right) \tag{3.2}$$

Integration of the pressure gradient from x_1 to x_2 should be equal to the pressure difference between x_2 and x_1,

$$\int_{x_1}^{x_2} \frac{12\mu}{h^3}\left(\frac{U}{2}h - q\right)dx = p_2 - p_1 \tag{3.3}$$

In Equation (3.3), the volumetric flow rate q is the only unknown, and it is ready to be written as

$$q = \frac{\int_{x_1}^{x_2} \frac{6\mu U}{h^2}dx - (p_2 - p_1)}{\int_{x_1}^{x_2} \frac{12\mu}{h^3}dx} \tag{3.4}$$

After the flow rate is obtained, the pressure gradient can be calculated by Equation (3.2), and the pressure distribution, the supporting force and its moment on the ring running-surface are sequentially solved. The shear stress applied on the ring that can be integrated to get the hydrodynamic friction force is

$$\tau = \frac{\mu U}{h} - \frac{h}{2}\frac{dp}{dx} \tag{3.5}$$

3.2.6 Gas Flow through the Channel

As mentioned in Chapter 3.2.3 and 3.2.4, the channel gas flow is a key physical phenomenon in determining the force around the ring and the pressure of the gas zones. As suggested in [14], this kind of gas flow can be simulated based on the assumption of fully developed, quasi-steady and locally-parallel flow (Poiseuille flow).

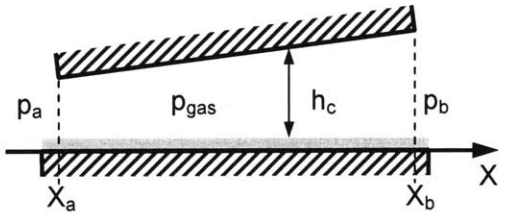

Figure 3-8 Configuration of channel flow

For a Poiseuille flow through the channel shown in Figure 3-8, which is applicable to both ring/liner and ring/groove interface, the volumetric flow rate through a unit width of any section can be written as

$$q = -\frac{h_c^{\,3}}{12\mu_{gas}}\frac{\partial p_{gas}}{\partial x} \tag{3.6}$$

where

$$h_c = h - h_{oil} \tag{3.7}$$

Then the pressure gradient can be expressed as a function of the flow rate

$$\frac{\partial p_{gas}}{\partial x} = -\frac{12\mu_{gas} q}{h_c^{\,3}} \tag{3.8}$$

Integration of the pressure gradient from x_a to x_b should be equal to the pressure difference between x_a and x_b,

$$\int_{x_a}^{x_b} -\frac{12\mu_{gas} q}{h_c^{\,3}} dx = p_b - p_a \tag{3.9}$$

In Equation (3.9), the volumetric flow rate q is the only unknown, and it is ready to be written as

$$q = -(p_b - p_a) \Big/ \int_{x_a}^{x_b} \frac{12\mu_{gas}}{h_c^{\,3}} dx \tag{3.10}$$

From Equation (3.8) and (3.10), we obtain

$$\frac{dp_{gas}}{dx} = (p_b - p_a) \Big/ h_c^{\,3} \int_{x_a}^{x_b} \frac{dx}{h_c^{\,2}} \tag{3.11}$$

Approximate the gas density as

$$\rho_{gas} = \frac{p_a + p_b}{2RT} \tag{3.12}$$

we obtain the mass flow rate per unit length along the circumferential direction:

$$\dot{m}_{gas} = (p_a^{\,2} - p_b^{\,2}) \Big/ 24\mu_{gas} RT \int_{x_a}^{x_b} \frac{dx}{h_c^{\,3}} \tag{3.13}$$

where T is the gas temperature, the gas viscosity is obtained by $\mu_{gas} = 3.3\times10^{-7}\times T^{0.7}$ according to [14]. The units of T and μ_{gas} are Kelvin and Pa-s, respectively.

The axial force and the corresponding moment generated by the gas pressure can be expressed as

$$F_{gas} = \int_{x_a}^{x_b} p_{gas}\,dx = p_b(x_b - x_a) - \int_{x_a}^{x_b}(x - x_a)\frac{dp_{gas}}{dx}dx \tag{3.14}$$

$$M_{gas} = \int_{x_a}^{x_b} p_{gas}\,x dx = \frac{1}{2}p_b(x_b^{\,2} - x_a^{\,2}) - \frac{1}{2}\int_{x_a}^{x_b}(x^2 - x_a^{\,2})\frac{dp_{gas}}{dx}dx \tag{3.15}$$

3.2.7 Gas Flow through a Ring Gap

The geometric configuration formed by a ring gap, the piston and the liner is shown in Figure 3-9. As can be detected, the ring gap is a common flow path connecting several gas zones. The pressure difference among these gas zones will induce complicated gas flows through the gap. Since the detailed gas dynamics is beyond the scope of this study, a simplified model is used.

The gas inside the ring gap and its open areas to three adjacent areas are shown in Figure 3-9. Among the three open areas, the one open to the gas zone inside the groove is much larger than the other two. Therefore, the gas pressure inside the gap can be assumed to be the same as that inside the groove. Then the gas flows between the gas zone on the piston lands and the gas inside the gap, $\dot{m}_{1-0}$ and $\dot{m}_{3-0}$ can be estimated by the isentropic orifice flow [34]:

$$\dot{m}_{gap} = \frac{C_D A_{gap} P_U}{\sqrt{RT_U}} f_m \tag{3.16}$$

where

$$f_m = \begin{cases} \gamma^{\frac{1}{2}}\left(\dfrac{2}{\gamma+1}\right)^{\frac{\gamma+1}{2(\gamma-1)}} & \dfrac{P_D}{P_U} \le \left(\dfrac{2}{\gamma+1}\right)^{\frac{\gamma}{\gamma-1}} \\ \left(\dfrac{P_D}{P_U}\right)^{\frac{1}{\gamma}}\left\{\dfrac{2\gamma}{\gamma-1}\left[1-\left(\dfrac{P_D}{P_U}\right)^{\frac{\gamma-1}{\gamma}}\right]\right\}^{\frac{1}{2}} & \dfrac{P_D}{P_U} > \left(\dfrac{2}{\gamma+1}\right)^{\frac{\gamma}{\gamma-1}} \end{cases} \tag{3.17}$$

and

$$C_D = 0.85 - 0.25\left(\frac{P_D}{P_U}\right)^2 \tag{3.18}$$

Equation (3.18) is obtained by fitting the experimentally-measured data [34].

Once the gas flows between the piston lands and the gap are calculated by above orifice flow model, the gas flow between the groove and the gap ($\dot{m}_{2-0}$) can be estimated by applying the mass conservation law and assuming the mass change of the gas inside the gap is negligible: $\dot{m}_{2-0} = -(\dot{m}_{1-0} + \dot{m}_{3-0})$

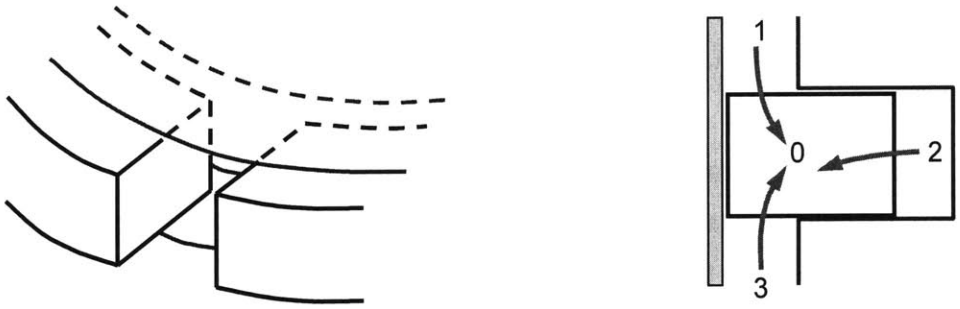

Figure 3-9 Configuration of gas flows through the ring gap

3.2.8 Governing Equations

Appling mass conservation and ideal gas law in one gas zone yields the following equation:

$$\frac{V}{RT}\frac{dP}{dt} + \frac{P}{RT}\frac{dV}{dt} = \sum \dot{m}_i \tag{3.19}$$

where, V is the gas volume, which changes with the piston secondary motion, P the gas pressure, and $\dot{m}_i$ the rate of gas flow into the gas zone through the ith path.

The rings in this study are not considered to be rigid bodies, and therefore their dynamic response to the external loads must be resolved by structural analysis. The 3-D finite beam element model introduced in Chapter 2 is employed to achieve this task. When dealing with the dynamic behavior of a ring, adding the inertial term into Equation (2.3) yields the following dynamic equation:

$$M\ddot{U} + KU = S - S_I \tag{3.20}$$

where, M is the mass matrix of ring structure, $\ddot{U}$ a vector consisting of the second order derivative of the displacements. In this formula, the velocity-dependent damping term $C\dot{U}$ is omitted and can be considered to be included in the load vector S if necessary.

Applying Equation (3.19) to all of the gas zones and Equation (3.20) to three rings yields the governing equations for the system under investigation. If the power cylinder system is discretized into N cross-sections, the equation set can be summarized as follows:

$$\frac{V_n}{RT_n}\frac{dP_n}{dt} + \frac{P_n}{RT_n}\frac{dV_n}{dt} = \sum \dot{m}_{n,i} \qquad (n = 1\sim 5N) \tag{3.21}$$

$$M_m\ddot{U}_m + K_mU_m = S_m - S_{I,m} \qquad (m = 1, 2, 3) \tag{3.22}$$

It needs to be pointed out that Equation (3.22) for each ring (different "m") is essentially a set of 6N equations. Therefore, the total number of governing equations represented by Equation (3.21) and (3.22) is 23N, which is equal to the amount of the system variables.

3.3 Computation Algorithm

To solve the governing Equations (3.21) and (3.22), the following implicit integration scheme is implemented to achieve numerical stability:

$$\frac{P_n^t(2V_n^t - V_n^{t-\Delta t})}{\Delta t R T_n} = \sum \dot{m}_{n,i}^t + \frac{P_n^{t-\Delta t} V_n^t}{\Delta t R T_n} \quad (n = 1 \sim 5N) \tag{3.23}$$

$$(\frac{M_m}{\Delta t^2} + K_m)U_m^t = S_m^t + \frac{M_m}{\Delta t^2} U_m^{t-\Delta t} + \frac{M_m}{\Delta t} \dot{U}_m^{t-\Delta t} - S_{l,m} \quad (m = 1, 2, 3) \tag{3.24}$$

The above equations are nonlinear and Newton's method with a globally convergent algorithm was used to solve them numerically. The Jacobian matrix in the Newon's method is doubly bordered band diagonal, and special numerical approaches described in [35] are employed.

3.3.1 Interaction of the System Variables

When using Newton's method, the Jacobian matrix must be evaluated. To obtain the entries in the Jacobian Matrix, we need to know how one variable changes with other variables. The interaction map of the system variables is sketched in Figure 3-10, where for simplifications the six DOFs of a ring cross-section are denoted as one symbol. To illustrate the interaction, let's consider the gas pressure in the second land (G2) at ith cross-section. As discussed in Chapter 3.2.4, the gas pressure in the second land can be influenced by gas flows between itself and several adjacent gas zones: the gas behind the first ring (G1), the gas behind the second ring (G3), the gas in the third land (G4), the gas in the second land of (i-1)th cross-section, and the gas in the second land of (i+1)th cross-section. In addition, the dynamics of the top ring and the second ring may change the geometrical shape of gas flow channels and hence influence the gas pressure in the second land.

3.3.2 Labeling of System Variables

As mentioned before, the Jacobian matrix in the Newon's method is doubly bordered band diagonal. In order to make the band width as small as possible, the labeling sequence of the system variable is cross-section by cross-section, and in each cross-section is from the top to the bottom. For instance, the first 23 variables are those in the first cross-section. Among them, the 1^{st} – 6^{th} are the six DOFs of the top ring; the 7^{th} is the pressure inside the top ring groove; 8^{th} is the pressure of the second

land; the 9^{th} – 14^{th} are the six DOFs of the second ring; the 15^{th} is the pressure inside the second groove; the 16^{th} is the pressure of the third land; the 17^{th} – 22^{nd} are the six DOFs of the oil ring; the 23^{rd} is the pressure of the oil ring groove. The 24^{th} – 46^{th} are the variables in the second cross-section, from the DOFs of top ring to the gas pressure inside the oil ring groove. This process repeats until the variables in the last cross-section are labeled.

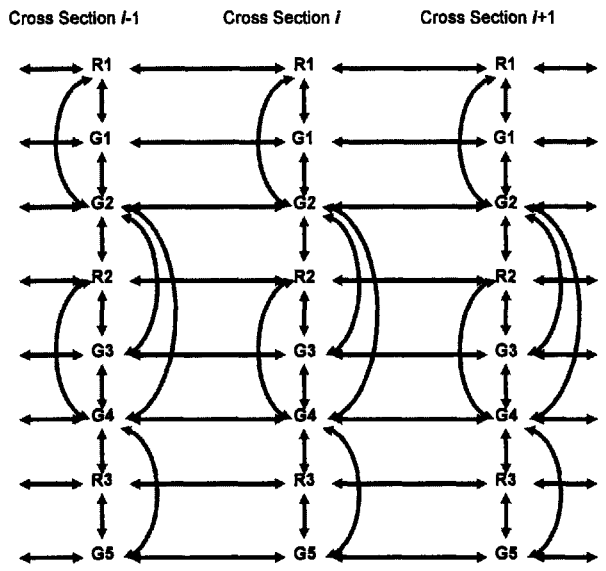

Figure 3-10 Interaction map of system variables

3.3.3 Computational Efficiency

Although it is a 3-D numerical model, the selected physics sub-models and numerical approaches enable a highly efficient numerical system. On author's PC (Pentium 4, 3.00 GHz CPU, 1GB RAM), it takes ten to fifteen minutes for one cycle when running with 0.1 CAD as the time step, and with circumferential discretization of 41 cross-sections.

3.4 Sample Results

This model was developed as a 3-D extension of the existing 2-D model that was described by Tian [13]. As stated in the previous section, most of the modeling approaches in these two models are similar. The comparison between these two models, which is not presented in this thesis, was performed to gain confidence for the 3-D model. For the power cylinder system without those 3-D features such as bore distortion, non-uniform ring static twist, and piston secondary motion, excellent agreement between these two models was obtained.

In the following discussion, the power cylinder system of a heavy-duty diesel engine was used as the example to conduct the calculation and demonstration. The engine has a bore of 131mm and a stroke of 150mm. A cross-sectional view of the piston ring-pack is shown in Figure 3-11. The cut in the upper ID of the keystone top ring gives a positive static twist, and the cut in the lower OD of the second ring creates a negative static twist.

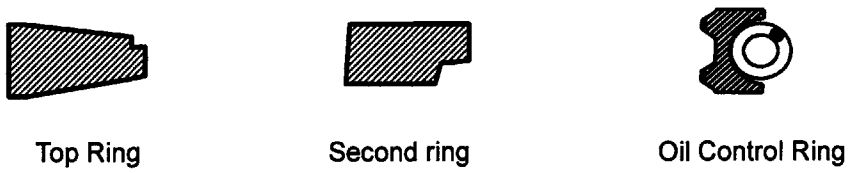

Figure 3-11 Cross-sections of the ring-pack in a heavy-duty diesel engine

One of the reasons to choose this engine was that extensive in-cylinder measurements and finite element analysis for this engine were conducted by Mahle and Volvo. As inputs to the model, piston tilt and lateral motions were measured, while bore distortion and piston deformation were calculated by finite element analysis. The cylinder pressure, inter-ring pressure and ring lifts were measured as well. It needs to be pointed out that comprehensive comparison between model predictions and measurements is not the subject of this work. However, a few key findings that were revealed by both the model predictions and the measurements will be discussed.

With proper initial conditions, the model starts at a specified crank angle degree in the exhaust stroke. The convergence is achieved when the ring positions and inter-ring gas pressures at the start of intake stroke match those at the end of exhaust stroke. Experience with the model indicated that two consecutive full-cycles are usually sufficient to reach the convergence for low-speed condition. Therefore, all of the results shown in this section are from the second full-cycle.

For all of the cases tested in this study, the engine was running hot with speed of 1600 RPM and load of 300Nm. The gap locations were arranged as follows: the gaps of top ring and twin-land oil

control ring were pinned at the thrust side; the second ring gap was pinned at the anti-thrust side. In baseline calculation, all of the real engine parameters were used and operating parameters such as thermal expansion, bore distortion and piston secondary motion were taken into account. For other testing cases, some changes were made to the rings and piston in order to carry out discussion more efficiently.

Several definitions need to be clarified before the results are presented. As shown in Figure 3-12a, the lift of a ring at a specific cross-section is the ring/groove clearance directly below the center of gravity (c.g.). The sign conventions for the ring twist angle, groove tilt angle and the relative angle between the ring side and the groove flank are shown in Figure 3-12b.

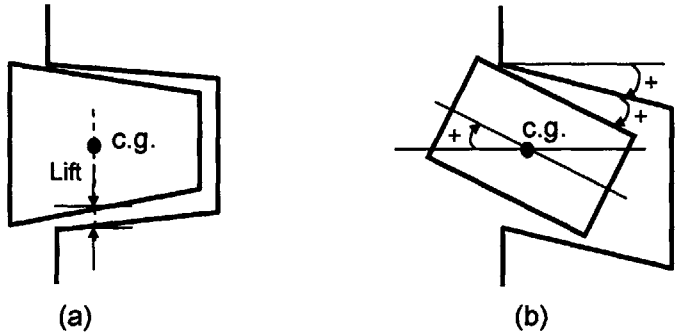

Figure 3-12 Definition of ring axial lift and sign conventions for angles of ring and groove

The calculated inter-ring pressures at the pin side (90 degree from the thrust-side) for the baseline condition are plotted in Figure 3-13. For this engine at this condition, the pressure variation along the circumference is small and the results shown in Figure 3-13 are representative for the entire system.

The lifts of the keystone top ring at three different circumferential locations are shown in Figure 3-14. All of the three locations show a similar behavior in terms of the lift timing. Differences occurred when the ring is seated on the upper flank of the piston groove. The cause of this difference was identified to be piston secondary motion. As illustrated in Figure 3-15, when the ring is seated on the upper flank of groove under the influence of upward inertial force and friction force, which is the case at the early part of intake stroke, the piston is moving towards the anti-thrust side. Since the ring does not move laterally due to the constraint applied by the cylinder bore, it is pushed down at the anti-thrust side, and raised up at the thrust side. At the pin side, however, because there is no relative motion between the ring and groove flank in the radial direction, the ring remains at almost the same axial position. These results are supported by the experimental measurements, which are shown in Figure 3-16.

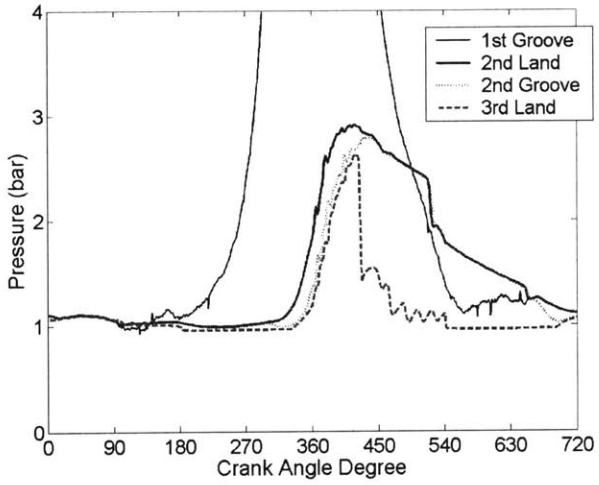

Figure 3-13 Calculated inter-ring gas pressure

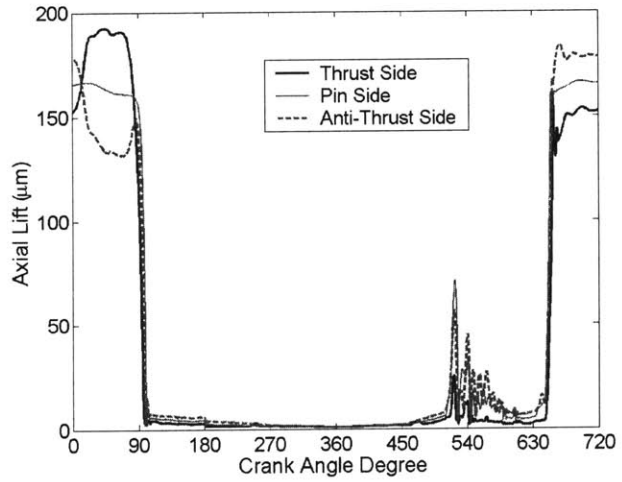

Figure 3-14 Calculated top ring axial lift

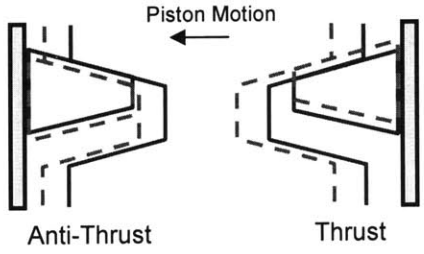

Figure 3-15 Effects of piston secondary motion on the lift of keystone ring

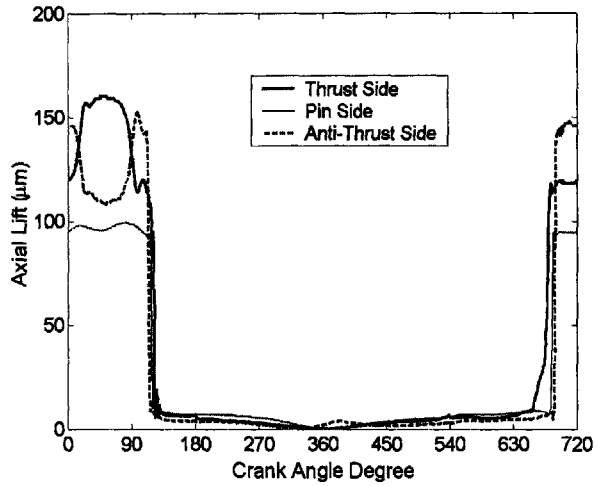

Figure 3-16 Measured top ring axial lift

Figure 3-17 shows the second ring lift at three different locations around its circumference. The lift behaviors differ greatly from each other. At the anti-thrust side that is also the location of the gap, the ring tends to stay at high axial positions. This phenomenon is easy to understand considering the fact that a ring with a negative static twist is bended upwards around the gap when it is inserted into the engine (Chapter 2 and [36]). As a result, the ring experienced severe wear on its upper side and no wear on its lower side around ring gap locations (Chapter 2 and [36]). From Figure 3-17, it can also be seen that the ring at thrust side does not lift as high as the other two locations. Meanwhile, its lowest position is not as low as the other two locations. As revealed in Chapter 2 and [36], the ring has its maximum static twist angle at the back point (180 degree from gap location). Under the constraint of the piston groove, greater ring twist leaves less space for ring to move axially, which explains the smaller lift at the back point. The measured lift of the second ring at the thrust and pin side are shown in Figure 3-18. It can be seen that the maximum lift at the pin side is larger than that at the thrust side, which proves the finding from the model results. It needs to be clarified that the measured lift shown in Figure 3-18 is after being shifted to make the minimum lift to be zero. In reality, when the ring has a static twist that is not equal to the groove tilt angle, the minimum lift should be greater than zero.

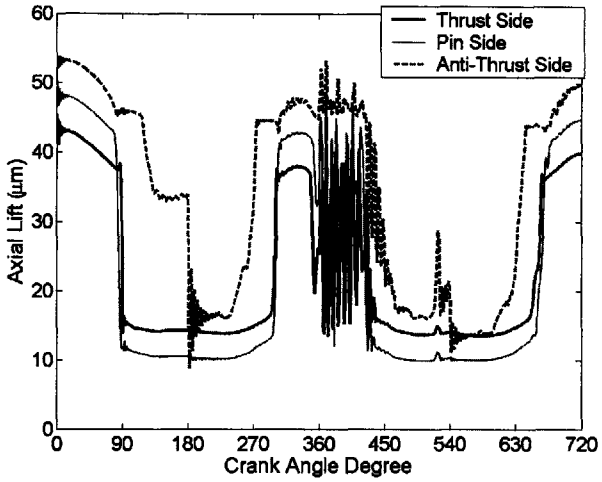

Figure 3-17 Calculated second ring axial lift

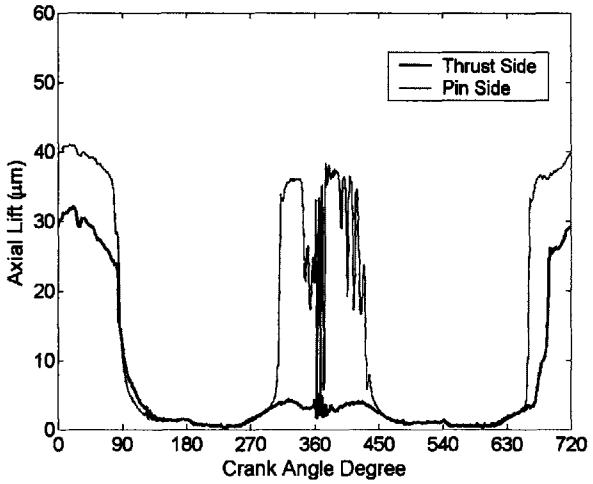

Figure 3-18 Measured second ring axial lift

The negative relative angle between the second ring's upper side and the piston groove flank makes the ring flutter possible [3]. From Figure 3-17 and Figure 3-18, we can see that around combustion TDC, both model results and measurements show evident ring flutter at the pin side. However, although the flutter at the thrust side is also revealed by the model results, it is not found in the measurements. One possible explanation for this phenomenon is that, since the portion of the second ring at the thrust side is directly below the top ring gap, the gas or oil flow across the top ring gap, driven by the pressure difference between the crown land and the second land, could apply significant dynamic pressure on the ring's upper side and push the ring down. Since resolving this

localized flow below the top ring gap may need specific efforts, this dynamic pressure was not simulated in this model. Therefore, the flutter at the thrust side is detected in the model results.

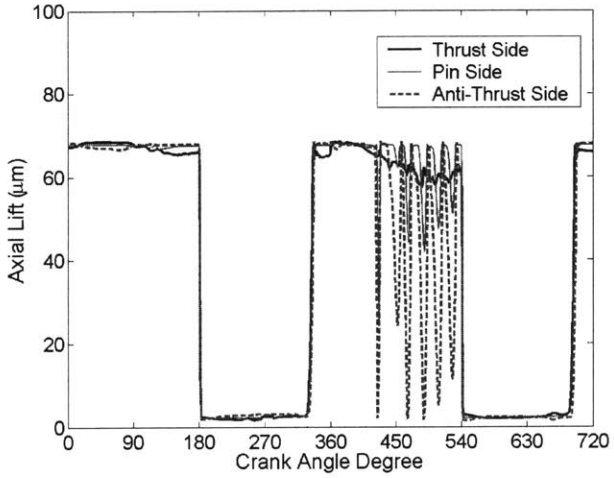

Figure 3-19 Calculated oil ring axial lift

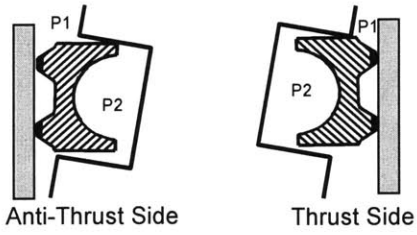

Figure 3-20 Effects of piston tilt motion on the ring/groove relative angles

Figure 3-19 shows the lift of the twin-land oil control ring in three circumferential locations. For most of the engine cycle, all three locations behave similarly. However, during the expansion stroke, this ring has different lift behaviors at three locations. During the early stage of expansion stroke, the entire ring stays at the upper flank of the groove. Starting from 420 CAD, ring flutter occurrs at the anti-thrust side, while at the thrust side the ring remains at the top. Piston tilt motion was found to be responsible for this phenomenon. For a twin-land oil control ring, the high tension and relatively low torsional stiffness make both lands tend to contact the cylinder liner. Therefore, the piston tilt can generate a relative angle between the ring and the piston groove. Under the influence of the upward inertial force and ring/liner friction force, the ring remains on the upper flank of groove at the early stages of expansion stroke. As the gas pressure builds up inside the third land and the upward inertial

force reduces, the gas pressure can push the ring down. From 420 to 540 degrees, the piston tilts toward the thrust side. As shown in Figure 3-20, the ring forms a positive relative angle with the upper flank of piston groove at the thrust side and a negative relative angle at the anti-thrust side. The entire upper side of the ring at the anti-thrust side is exposed to high pressure P1, while lower pressure P2 acts on most part of the ring upper side at the thrust side. As a result, the gas pressure is able to push the ring down at the anti-thrust side and ring flutter occurrs. The corresponding gas flow rate between the twin-land oil control ring and upper flank of the piston groove is plotted in Figure 3-21, as well as the gas flow rate of the other two locations. The significant difference due to ring flutter can be immediately seen.

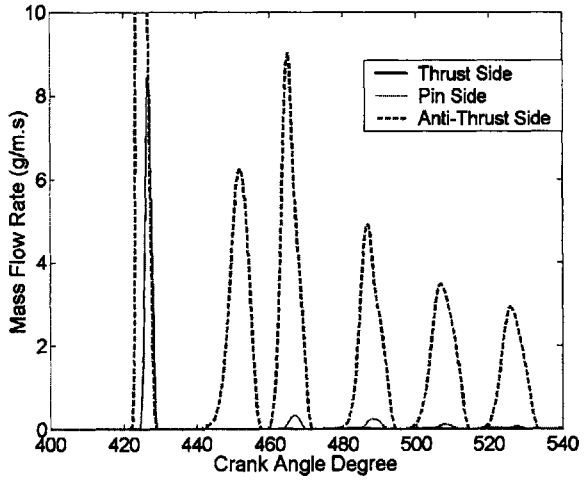

Figure 3-21 Calculated gas flow rate at different locations of oil control ring

The flutter of oil control ring has a direct impact on the gas flow and oil transport between the ring and its groove flanks [3]. In the case of the engine used in this study, without the effects of the piston tilt motion, the ring can not flutter because the negative groove tilt angle creates a positive ring/groove relative angle throughout the engine cycle. To predict the engine blow-by and study oil transport, it is crucial to include the piston tilt effects. The 2-D models can account for the effects of piston tilt motion by assuming a single ring/groove relative angle. However, the limitation is obvious since the variations of ring/groove relative angle and hence the ring dynamic lifts along the circumference are totally neglected. The ability to address the piston tilt effects more accurately is one of the major advantages of the 3-D model.

As mentioned above, the relative angle between the ring and the groove flanks plays a crucial role in determining the ring dynamics and identifying potential ring flutter. A more detailed description of

the ring flutter can be found in [3] and is not repeated here. The second ring used in this study has a negative static twist angle that varies along its circumference, from a small value at gap location to a large value at back point. If the negative groove tilt angle is large enough, some portion of the ring may have a positive relative angle with the groove flank while other portion has a negative angle. This implies that under some conditions, part of the ring may flutter while the rest will not. To investigate the possibility of so-called local flutter, the second ring with new design that has a greater static twist was used, and tilt of second groove was changed such that both positive and negative relative ring/groove angle would be achieved. Two cases with groove tilt angle of 0.6 degree and 0.8 degree respectively were investigated. The lift of the second ring during part of the engine cycle with the groove tilt of 0.6 degree and 0.8 degree are shown in Figure 3-22 and Figure 3-23, respectively. In these figures, the brightness denotes the lift magnitude, with the brighter color indicating greater axial lift. It can be seen from both figures that the ring is not behaving as a rigid body in terms of the flutter motion. The portion around the ring back point (around 180 degrees) shows evident flutter behavior, while the portion around the ring gap location does not flutter at all. It can also be seen that for the 0.6 degree case, the range of circumferential angle over which flutter occurs is wider than that of the 0.8 degree case. To understand this phenomenon, the static twist angle distribution of the second ring is shown in Figure 3-24, with two horizontal straight lines marking 0.6 degree and 0.8 degree, respectively. It can be seen that in the case of groove tilt of 0.6 degree, a greater portion of the ring has a negative relative angle with groove. As a result, the flutter region is wider than that of 0.8 degree case.

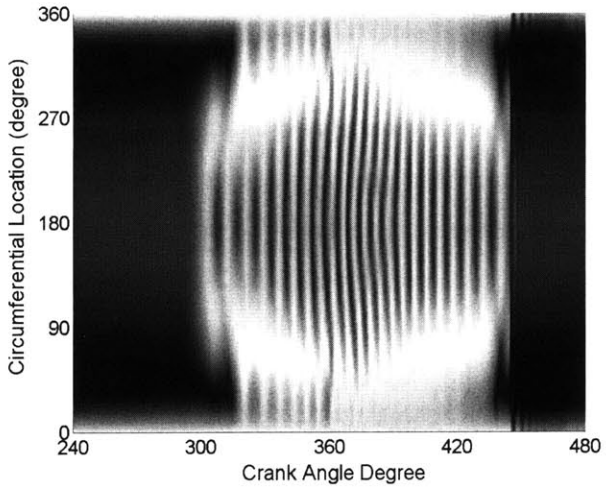

Figure 3-22 Calculated second ring lift with the groove tilt of -0.6 degree (brightness denotes the lift magnitude)

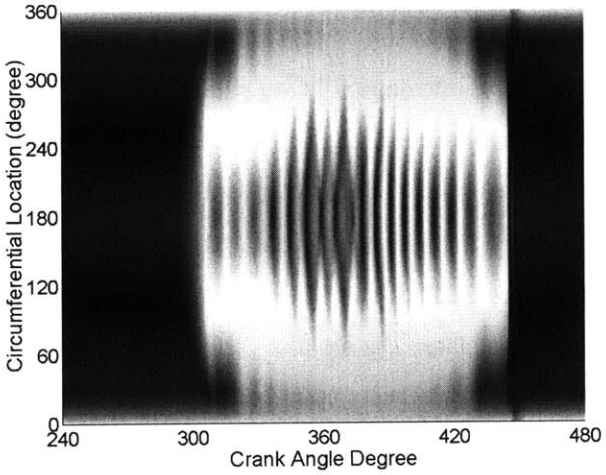

Figure 3-23 Calculated second ring lift with the groove tilt of -0.8 degree (brightness denotes the lift magnitude)

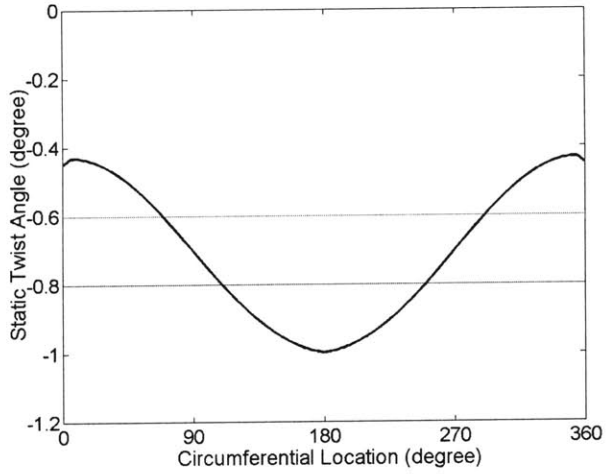

Figure 3-24 Static twist angle of the second ring and groove tilt angle

The pressure distribution along the land circumference is not uniform. The difference of pressure is the driving force for the oil transport along the land circumference, and ought to be well simulated [27]. In this study, the position of the top ring gap and the second ring gap were set in opposite locations along the circumference. For the gas inside the second land, the pressure at the thrust side, which was directly below the top ring gap, should differ from the pressure at the anti-thrust side, which was directly above the second ring gap. Experience with this model shows that the pressure difference along the circumference of the piston land largely depends on the clearance between the

piston land and the cylinder liner. For the baseline case, the average clearance between the second land and liner is about 300μm with consideration of the thermal expansion of both the liner and the piston. The pressures at the thrust side and anti-thrust side as well as their difference are shown in Figure 3-25. It can be seen that the pressure does not vary significantly from side to side, which means that under this land-liner clearance condition, the gas flow is fast enough to create a uniform pressure along the entire circumference. To examine the effects of land-liner clearance, the clearance between second land and liner was arbitrarily changed to 100μm, and for comparison the pressure traces and their difference are shown in Figure 3-26. It can be seen that the pressure difference is significant from the thrust-side to the anti-thrust side. The smaller clearance creates larger flow resistance and therefore increases the time required for the pressure to become uniform. The capability of the current 3-D model to predict the pressure distribution makes it possible to conduct a detailed analysis of circumferential oil transport.

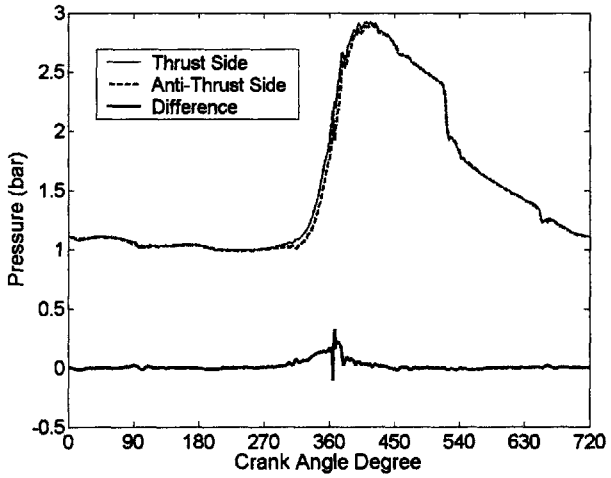

Figure 3-25 Calculated pressures and difference in the 2nd land of baseline

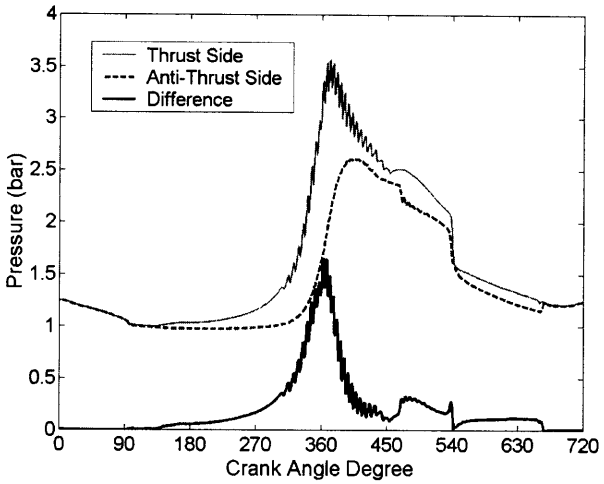

Figure 3-26 Calculated pressures and difference in the 2nd land with small land-liner clearance

3.5 Conclusions

A three-dimensional model for piston ring-pack dynamics and blow-by gas flow was developed in this study. Its ability to predict the variation of ring dynamics and gas flow along the circumference makes it possible to perform more in-depth investigations of ring dynamics and oil transport. The computational efficiency of the model allows fast simulation and hence has appreciable practical value.

Preliminary application of the model to a heavy-duty diesel engine showed significant variations along the system's circumferential direction in terms of the structural dynamic response of the piston ring-pack. Specifically, local ring flutter was detected for the second ring with an asymmetric cross-section and a non-uniform static twist angle distribution. Piston dynamic tilt was found to have a significant influence on the ring performance and gas flow by creating a negative relative angle between the twin-land oil control ring and its groove flanks. Significant variation of gas pressure along the circumference of piston land was also detected when the land-liner clearance is small.

This model provides comprehensive 3-D information for the ring dynamics and gas flow, which can be used to perform other studies such as wear, ring stress, oil transport and oil consumption, especially when localized phenomena are of interests.

Chapter 4 Modeling Ring-Pack Lubrication

4.1 Introduction

The lubrication occurring in the interface between the ring running surface and the liner is a typical tribology phenomenon. It covers from boundary lubrication, to mixing lubrication, and all the way to hydrodynamic lubrication. To model ring/liner lubrication, models corresponding to each lubrication mode have to be developed.

To model boundary lubrication, an asperity contact model is usually implemented to calculate the normal force between two solid surfaces. The normal force is then used to estimate the sliding friction by multiplying a boundary friction coefficient. For hydrodynamic lubrication, a number of hydrodynamic models have been developed to be applicable to the ring/liner configuration. The starved hydrodynamic situation and mass conservation requirements make it difficult to have a well defined model. When mixing lubrication occurs, both boundary lubrication and hydrodynamic lubrication model are used.

In order to have a ring-pack lubrication model that can be used to precisely predict the friction and oil transport along the liner, an advanced hydrodynamic lubrication model should be developed firstly. Then the structural response of the ring-pack to the lubrication force and other external forces has to be resolved to get the final ring/liner lubrication situation.

In this chapter, two separate sections are used to illustrate the ring-pack lubrication model. In the first section, an improved hydrodynamic lubrication model is introduced. Emphasis is placed on the preservation of flow continuity and physical correctness. The second section will illustrate how the lubrication model is coupled with ring structural analysis to set up the ring-pack lubrication model. The ring-pack lubrication model is applied to a light-duty diesel engine, and some sample results are shown.

4.2 Development of a Flow Continuity Algorithm

4.2.1 Background

Experimental evidence has shown that piston rings usually experience lubricant starvation in an engine cycle, which means only a portion of the interface between ring running-surface and cylinder liner is covered with lubrication oil [37-40]. Following this finding, various theoretical attempts have been made to locate the region of full oil film. In a lubrication analysis of a ring-pack conducted by Dowson [20], a simple iterative procedure was used to determine the location of the start of the full film. In Jeng's comprehensive model of starved piston ring lubrication [23], three equations were derived to describe the starved condition, and the starting point of the full film was obtained by solving this system of equations.

As for how to locate the ending point of the full film region, a clear divergence of opinion can be found in the literature, where different boundary conditions were proposed [20, 22-24]. A comprehensive comparison and sensitivity study about those boundary conditions were conducted by Priest [41], and significant differences were reported. Currently, Reynolds exit condition without film reformation is generally used. Around dead centers of a ring in an engine cycle, squeezing motion of the ring become dominant, and the Reynolds exit condition can not be applied. To address this concern, Tian [25] proposed a "film non-separation" exit condition to replace the Reynolds exit condition around dead centers.

The simultaneous prediction of inlet and outlet boundaries can be a complex and time consuming task. In the simulation of journal bearings, a boundary condition called JFO theory, which was initiated by Jakobsson and Floberg [42] and further developed by Olsson [43], can properly treat the cavitation in both film rupture and film reformation location. Because of the complexity of JFO theory, Elrod [44] suggested a "universal" differential equation that is valid both in full film and cavitation regions, and introduced a finite difference algorithm to predict cavitation region automatically. Paydas and Smith [45] improved the stability of "Elrod algorithm" by remove its compressibility effort, and had a successful application in the study of journal bearings.

Ma [46], for the first time, applied the improved "Elrod algorithm" [44] to the study of piston ring lubrication. In order to address the non-axisymmtric characteristics of the ring lubrication, two-dimensional approach was taken. This work was further extended to the study of a complete ring-pack, and proved to be very promising [30, 31]. However, in Ma's models [46, 30, 31], the same assumption as in the journal bearings was used for the oil flow patterns in the partially-filled regions, namely, the partially-filled regions are composed with oil and air streams and each individual stream fully attaches to both surfaces. This assumption may not be appropriate for the following reasons. It

needs to be recognized that ring/liner lubrication is open-loop, contrast to the journal bearings that have a closed loop. If a ring is taken as a reference, the oil is carried by the liner before it enters the full-film region between the ring face and the liner. Therefore, the oil is fully attached to the liner and is separated from the ring face by the air in the partially-filled region (P_1 region in Figure 4-1). Additionally, after oil exits the full-film region (P_2 region in Fig. 1), it is likely that the oil fully attaches to the liner and is being carried away. The streaky patterns that are present in the cavitation regions in journal bearings were never observed in the ring/liner interface under real engine operating conditions [27, 47, 48]. All these experimental works [27, 47, 48] suggested that the in the starved lubrication condition between a ring and liner in real applications, the oil attachment patterns are as depicted in Figure 4-1. Furthermore, in the situation that there is no full-film region between the ring and liner, the oil should be fully attached to the liner and fully detached from the ring face. Oil starvation, complete loss of hydrodynamic lubrication, and reappearance of hydrodynamic lubrication occur frequently within an engine cycle in the ring/liner lubrication, especially when the bore distortion becomes sufficiently large. The assumptions on oil attachment patterns in the partially-filled regions are critical to determining the oil film distribution along the liner and thus need to be handled carefully in order to preserve the oil mass conservation in the interface of ring pack and the liner.

In this work, the universal Reynolds equation used by Ma [46] is adapted to describe ring/liner lubrication. Based on experimental findings, different assumptions from Ma [46] on the oil flow patterns in the partially-filled regions are used. A transition region is introduced between the full-film and partially-filled regions to smooth out the discontinuity between these two regions. In the following, the details of the hydrodynamic lubrication model are described first. It is then used in several unsteady cases to demonstrate its capability of handling difficult lubrication situations such as oil reattachment and oil-squeezing dominant flows. The effectiveness and robustness of the present hydrodynamic lubrication makes it possible to develop a 3-D ring pack lubrication model with consideration of the ring structure response to non-axisymmetric characteristics of the power cylinder system such as bore distortion and piston secondary motion [49].

4.2.2 Model Formulation

Although current hydrodynamic lubrication model will be eventually used in the application of non-axisymmetric calculation, we can still assume locally it is a one-dimensional problem because the dimension in the axial direction of a ring is much smaller than that in the circumferential direction and the oil flow variation along the circumference is much less than in the axial direction.

Governing Equation

The situation of ring/liner lubrication is not the same as that of the journal bearing. As sketched in Figure 4-1, the ring/liner interface can be divided into three regions: leading partially-filled region, fully-filled region, and trailing partially-filled region. Unlike the journal bearing case that has a closed loop, there is no cavitation region that is surrounded by two fully-filled regions. In the partially-filled region, the oil can be assumed to be attached to the liner only. Therefore, the assumption used by the journal bearing that mixture of oil and oil vapor attach to both surfaces is not applicable anymore.

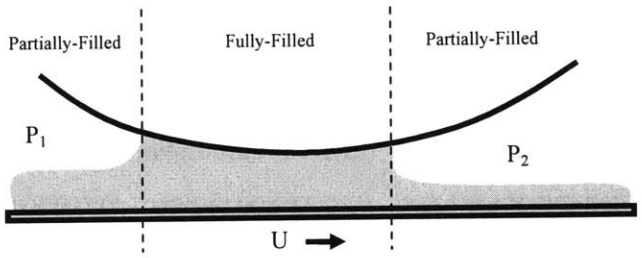

Figure 4-1 Configuration of ring/liner lubrication

In this model, the partially-filled regions and fully-filled region are treated differently. In the fully-filled region, the classical hydrodynamic lubrication occurs and the Reynolds equation can be used to resolve the mass transport and the pressure distribution:

$$\frac{\partial h_{oil}}{\partial t} = \frac{\partial}{\partial x}\left(\frac{1}{12\mu} h_{oil}^{\ 3} \frac{\partial p}{\partial x}\right) - \frac{1}{2} U \frac{\partial h_{oil}}{\partial x} \tag{4.1}$$

While in a partially-filled region, there is no hydrodynamic lubrication, and the pressure is uniform since the oil exposes to the same gas pressure. The only issue to be considered is the oil transport, which is essentially a wave-function problem:

$$\frac{\partial h_{oil}}{\partial t} = -U\frac{\partial h_{oil}}{\partial x} \tag{4.2}$$

As suggested by the method used in the journal bearing lubrication [44], the solution of a single, "universal" differential equation, which will change character in the fully-filled region and the partially-filled regions, is more convenient than dealing with separate equations (4.1) and (4.2). To obtain this universal equation, an index quantity F and a single variable ϕ that has a different definition in a fully-filled region and a partially-filled region are introduced. ϕ and F are defined as follows,

$$\frac{P - P_0}{P_0} = F\phi \tag{4.3}$$

$$\frac{h_{oil}}{h} = 1 + (1 - F)\phi \tag{4.4}$$

$$F = \begin{cases} 1 & \phi > 0 \\ 0 & \phi < 0 \end{cases} \tag{4.5}$$

where P is the pressure , P_0 a standard pressure, h_{oil} the oil film thickness. From Equation (4.3) through Equation (4.5), it can be seen that ϕ is a dimensionless pressure in a fully-filled region, and $(1+\phi)$ is the degree of oil filling in the partially-filled regions. By employing ϕ and F, Equation (4.1) and Equation (4.2) can be written in a single form

$$\frac{\partial}{\partial t}((1 + (1 - F)\phi)h) = \frac{\partial}{\partial x}(\frac{P_0}{12\mu}(1 + (1 - F)\phi)^3 h^3 \frac{\partial(F\phi + 1)}{\partial x}) - \frac{U}{1 + F}\frac{\partial}{\partial x}((1 + (1 - F)\phi)h) \tag{4.6}$$

An inspection of Equation (4.6) reveals that there exists a discontinuity of the oil transported by convection at the separation point between a partially-filled region and a fully-filled region. Inside the partially-filled region, the oil is transported by the liner and the average convection velocity is U. Once the oil enters the fully-filled region, Couette flow occurs, slowing down the average convection velocity to be $U/2$. As a result, a great pressure gradient is needed at the separation point to push the oil out in order to satisfy the flow continuity. Although the physics in the real situation is not clear,

this discontinuity will generate numerical problems. To facilitate the numerical solution, a transition region is introduced between a partially-filled region and a fully-filled region.

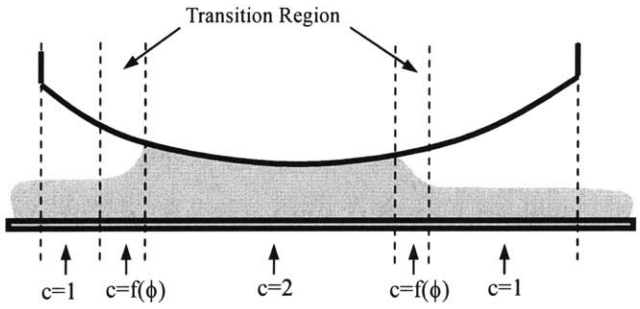

Figure 4-2 Transition regions introduced

As shown in Figure 4-2, the oil gradually attaches to the ring running-surface over the transition region. The starting point of this region is assumed to be the location where the degree of oil filling ($1+\phi$) equals 0.5, which means half of the ring/liner clearance is filled with oil. Inside the transition region, the oil is considered to be so close to the ring that, at some spots, the oil starts to have contact with the ring due to the roughness of the surfaces, but not fully attached. The convection oil transport in the transition region is modeled as

$$\frac{\partial h_{oil}}{\partial t} = -\frac{U}{c}\frac{\partial h_{oil}}{\partial x} \tag{4.7}$$

where c is a coefficient determined by the degree of oil filling, and its value varies from 1 at the starting point of the transition region to 2 at the ending point. In this study, c is expressed as a linear function of ϕ

$$c = f(\phi) = 2(1+\phi) \tag{4.8}$$

If the coefficient ($1+F$) of the convection term in Equation (4.6) is considered as the coefficient c in partially-filled and fully-filled region, an improved "universal" differential equation applicable to all regions can be written as

$$\frac{\partial}{\partial t}((1+(1-F)\phi)h) = \frac{\partial}{\partial x}(\frac{P_0}{12\mu}(1+(1-F)\phi)^3 h^3 \frac{\partial(F\phi+1)}{\partial x}) - \frac{U}{c}\frac{\partial}{\partial x}((1+(1-F)\phi)h) \quad (4.9)$$

where c is the coefficient of convection oil transport for all of the regions, and its general expression is

$$c = f(\phi) = \max(2(1+(1-F)\phi), 1) \quad (4.10)$$

In this universal equation, ϕ is the only variable, which is related to the pressure inside the fully-filled region, or the degree of oil filling inside the partially-filled and transition regions.

Numerical Formulation

Spatial and Temporal Discretization

The spatial computational domain is divided into grids as shown in Figure 4-3. A so-called cell-centred scheme, which stores the value of variable at the center of each cell, is employed. To ensure the computational stability, the implicit scheme is used for temporal discretization.

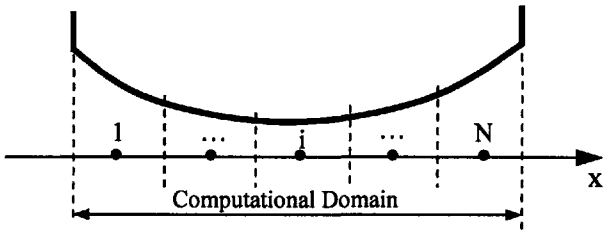

Figure 4-3 Discretization of the computational domain

Finite Volume Method

Finite volume method is used to set up the numerical equations. The basic idea about this method is to apply mass conservation inside a specific grid cell. As shown in Figure 4-4, for the ith grid cell, the net oil flow rate should be equal to the increase rate of the oil inside the cell. The oil flow at the interface between two adjacent cells can be considered to consist of two components: convection flow q^c, and pressure driven Poiseuille flow q^p. In partially-filled and transition regions, there is no pressure driven flow, and only convection flow exists. For the fully-filled region, both pressure driven flow and convection flow exist, and the convection flow is Couette flow. With the help of the versatile variable ϕ and the switch function F, the convection flow rates shown in Figure 4-4 can be calculated by using up-wind scheme as

$$q_{in}^{c} = \frac{U}{c_{i-1}}[1+(1-F_{i-1})\phi_{i-1}]h_{i-1} \tag{4.11}$$

$$q_{out}^{c} = \frac{U}{c_{i}}[1+(1-F_{i})\phi_{i}]h_{i} \tag{4.12}$$

and the pressure driven flows can be written as

$$q_{in}^{p} = \frac{P_0}{12\mu}\left[\frac{(1+(1-F_{i-1})\phi_{i-1})h_{i-1}+(1+(1-F_{i})\phi_{i})h_{i}}{2}\right]^{3}\frac{(1+F_{i-1}\phi_{i-1})-(1+F_{i}\phi_{i})}{\Delta x} \tag{4.13}$$

$$q_{out}^{p} = \frac{P_0}{12\mu}\left[\frac{(1+(1-F_{i})\phi_{i})h_{i}+(1+(1-F_{i+1})\phi_{i+1})h_{i+1}}{2}\right]^{3}\frac{(1+F_{i}\phi_{i})-(1+F_{i+1}\phi_{i+1})}{\Delta x} \tag{4.14}$$

The rate of increase of the oil volume inside the ith grid cell is

$$\dot{v}_i = \frac{[1+(1-F_i)\phi_i]h_i - [1+(1-F_i^{t-\Delta t})\phi_i^{t-\Delta t}]h_i^{t-\Delta t}}{\Delta t}\Delta x \tag{4.15}$$

where the superscript t-Δt denotes the value of previous time step. To satisfy the flow continuity, the total net mass flow rate into this cell must be equal to the rate of the increase of the oil volume, which yields the following governing equation

$$\dot{v} = q_{in}^{c} + q_{in}^{p} - q_{out}^{c} - q_{out}^{p} \tag{4.16}$$

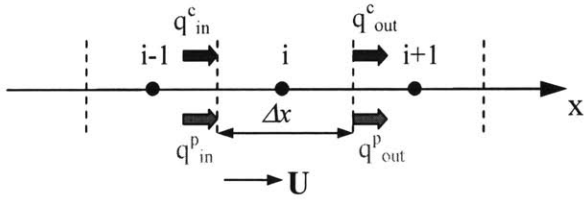

Figure 4-4 Flows associated with a grid cell

Boundary Condition

Two edges of the ring running-surface are the boundary of the computational domain. When finite volume method is implemented at cell 1 and cell N, ϕ at the location in front of node 1 and that at the location behind node N must be defined. Therefore, two extra nodes, node 0 and node N+1, are added to the computation domain, as shown in Figure 4-5. Since the pressure at these two nodes is known to be p1 and p2, respectively, they can be treated as partially-filled node and only the degree of oil filling is of interest.

The state of node 0 can be determined by the inlet oil film transported by the liner. When the inlet oil film thickness is smaller than the ring/liner clearance at the inlet point h_1, the degree of oil filling $(1+\phi)$ at node 0 is determined as h_{inlet}/h_1. When the inlet oil film thickness is greater that h1, the degree of oil filling at node 0 is set as 1. Then, the over-supplied oil will contribute to the oil-scraping that will be described later.

Except the case when the trailing edge of the ring is fully flooded, the state of node N+1 is not used in the calculation, since only the convection oil transport occurs at this point and the employed up-wind scheme ensures that the state of node N+1 will not influence the computation domain. Thus, the boundary condition at the trailing edge is not required in this case. However, when the trailing edge becomes fully flooded, the pressure driven oil flow from node N+1 to node N may occur. Then the state of node N+1 has to be determined. In this study, the degree of oil filly of node N+1 when trailing edge is fully flooded is set as 1.

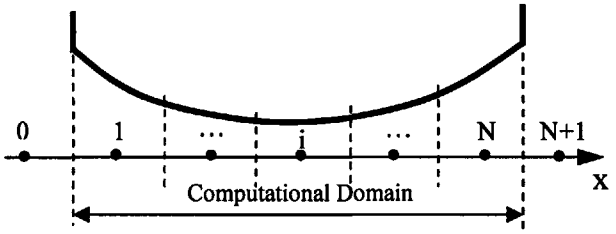

Figure 4-5 Two nodes are added to boundaries

Oil-Scraping

Once the fully-filled region reaches the leading edge of the ring running-surface, the over-supplied oil will be scraped by the ring leading edge. The so-called oil-scraping is an important topic of oil transport. If the oil-scraping of top ring occurs during upstrokes, the amount of scraped oil has a high possibility to contribute to the oil consumption.

To evaluate the oil-scraping, let's focus on the flow continuity at the boundary of the leading edge. As described before, the oil flow rate at a location consists of two parts, convection flow rate q^c and pressure driven flow rate q^p. Then the total flow rate is $q^c + q^p$. If the total flow rate at the boundary of leading edge is obtained, its difference with the available inlet flow rate that carried by the liner motion should be the rate of oil-scraping. That is

$$q_{scrape} = Uh_{inlet} - (q^c_{boundary} + q^p_{boundary}) \tag{4.17}$$

Because it is not clear where the scraped oil ends up to be, for simplification, all the scraped oil is assumed to stay on the ring side and accumulate. From oil consumption point of view, the oil accumulating on the upper side of top-ring can be considered as a crucial source.

Selection of Standard Pressure P_0

As implied by Equation (4.3), if the pressure at a cell is greater than the selected standard pressure P_0, this cell is considered as a fully-filled cell. If it is smaller, a partially-filled cell is identified. Therefore, it is critical to have a wise selection of P_0. In [46], the pressure at leading and trailing edge was assigned to two distinct portions of the computational domain, called upstream and downstream. The separation of the portions was defined as the location of maximum pressure that was tracked at every calculation step. The P_0 at upstream was set as the leading edge pressure, and the trailing edge pressure was assigned to the P_0 at downstream. This method was found by current authors to be viable throughout most part of the engine cycle. However, when the pressure difference $|P_1-P_2|$ is large and the width of the fully-filled region is small, a maximum pressure that is greater than both P_1 and P_2 can not be generated inside the fully-filled region, and numerical problems will be encountered. In addition, this method can not handle the oil-reattachment issue that will be introduced later. In this study, a piece-wise linear function is used to specify the P_0 across the entire computational domain. As illustrated in Figure 4-6, the entire computational domain is divided into three parts. The P_0 in the upstream part is set as P_1, and the P_0 in the downstream part is set as P_2. For the part that is in the vicinity of the location with minimum ring/liner clearance, a linear distribution of P_0 gives a gradual transition between P_1 and P_2. In this study, the width of the transition is one tenth of the width of the computational domain. By introducing this distribution function of P_0, the numerical problems encountered by the method used in [46] are well resolved.

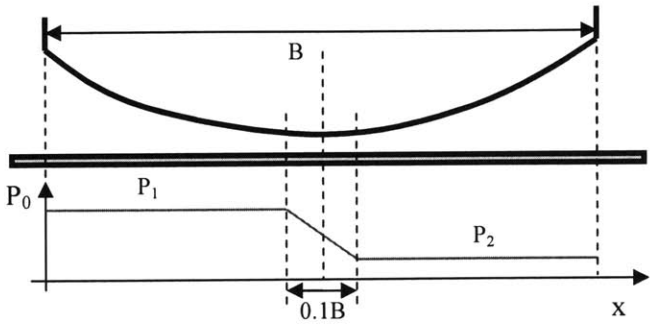

Figure 4-6 Distribution of standard pressure

Oil-Reattachment Issue

When there is no or small magnitude of bore distortion, the ring along the entire circumference can conform to the cylinder liner. Therefore, the ring always attaches to the lubricant oil, and there is no oil-reattachment issue. When the bore distortion is large, some part of ring running-surface can not conform to the liner during some crank angle degrees of an engine cycle, but can conform during other time. For example, the top ring is unable to conform to the liner during intake stroke and early part of compression stroke due to a large bore distortion; under the influence of gradually increasing gas pressure that acts on the back of the ring, the ring starts to approach the liner and may eventually touch the oil layer. To the authors' knowledge, although this so-called oil-reattachment issue is an unavoidable subject in simulating ring/liner lubrication especially when large bore distortion presents, it has never been addressed by existing studies.

The real physics happening around the time and location of oil-reattachment is still not clear, and it is beyond the scope of current study to make detailed investigation. For numerical purpose, inspections of this issue revealed several modeling difficulties. Firstly, at the moment just before the reattachment occurs, the convective oil flow carried by the liner movement has a uniform velocity profile along the direction perpendicular to the liner, thus the flow rate is $U \times h$. At the moment of reattachment, the convection flow is Couette flow and the flow rate becomes $U \times h/2$. To satisfy the mass conservation, there must be an outflow driven by the pressure difference, which requires a pressure jump inside the fully-filled region and in turn causes numerical problems. Secondly, when the pressure difference between leading edge and trailing edge is large; immediately after the oil-reattachment happens in a narrow region, the pressure gradient across this region becomes so great that uncontrollable things can happen and the whole numerical system becomes chaos.

In this work, the improved features of the model described in previous sections make it rather straightforward to handle all of the difficulties mentioned above. First, the introduced transition region gives a gradual oil-reattachment process. Before the ring running-surface touches the oil, when

the degree of oil filling exceeds 0.5, the oil starts to accumulate underneath the ring at the point with minimum ring/liner clearance, due to the reduced flow rate simulated by the coefficient c in Equation (4.7). Before the degree of oil filling reaches 1, the convection oil flow rate has been already restricted to $U \times h/2$, which is the same as when the oil attaches to the ring. Thus the pressure jump will not occur. Second, the distribution function of P_0 illustrated in Figure 4-6, which has a gradual transition part, can solve the large pressure difference problem, since the pressure gradient is well controlled and can not become too high.

Computation Algorithm

The governing equations, Equation (4.16), are nonlinear and Newton's method with a globally convergent algorithm was used to solve them numerically. The Jacobian matrix in the Newon's method is band diagonal, and the efficient solver for linear equations described in [35] is employed. After the variables ϕ at each grid point of the computational domain are calculated, the pressure in the fully-filled region and the oil film thickness in the partially-filled region can in turn be computed. It is then trivial to get the hydrodynamic supporting force and friction force.

4.2.3 Sample Results

To illustrate this hydrodynamic lubrication model, before used to a complete piston ring-pack, it was implemented to one cross-section of a ring. Since the core contents of this model are similar to the algorithm in [46], and extensive verifications of this algorithm have been reported in [46], only the improved features are presented in this section.

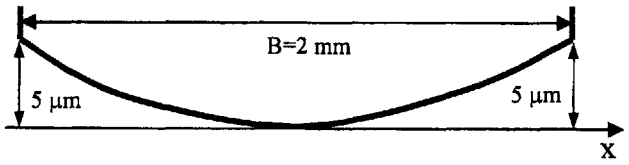

Figure 4-7 Ring running-surface with symmetric parabola shape

Figure 4-7 sketches the ring running-surface profile used in this study. It is a symmetric parabola. To simulate the operation condition of a ring in an engine cycle, the speed curve of the ring in the x direction and the movement curve of the ring in the y direction are designated and shown in Figure 4-8. The time duration is 9×10^{-3}s and the number of time steps is 180, which implies the time step to be 5×10^{-5}s. The initial oil film thickness of the liner is 2μm, and the viscosity of the lubricant oil is 3×10^{-3}Pa·s. The pressure at the trailing edge is set as 1 bar, while two values of the pressure at the leading edge, 1bar and 10bar, are used to simulate the various pressure difference between the leading and trailing edge.

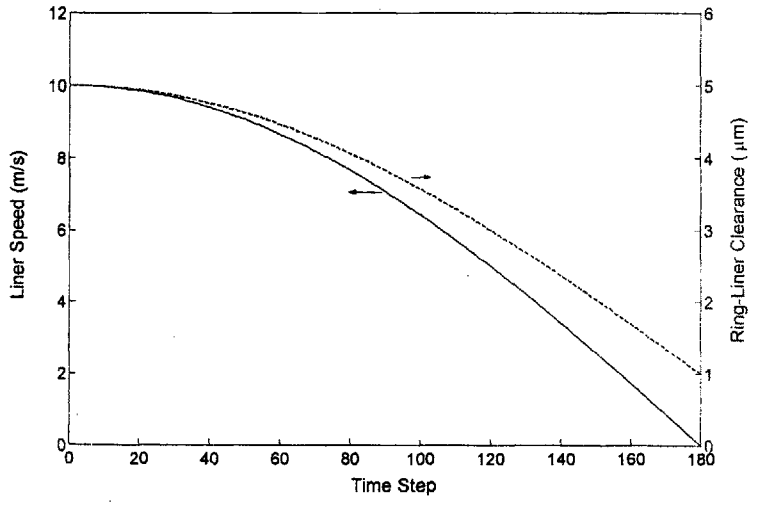

Figure 4-8 Designated evolution of liner speed and ring/liner clearance

For the case with 1bar as the leading edge pressure, the evolution of oil film thickness and pressure between the ring and the liner are shown in Figure 4-9 and Figure 4-10, respectively. At the beginning, because the minimum ring/liner clearance is greater than two times of the oil film thickness h_{oil}, the oil film on the liner is not influenced by the ring. When the ring moves closer to the liner and the ring/liner clearance becomes less than $2h_{oil}$ and greater than h_{oil}, there is still no hydrodynamic lubrication, but the oil starts to accumulate around the location of minimum ring/oil clearance. Once the oil film thickness reaches the ring/liner clearance, hydrodynamic lubrication occurs and the hydrodynamic pressure starts to be generated. As ring/liner clearance continues to decrease, more and more inlet oil carried by the liner can not pass the ring and the fully-filled region expands to both leading and trailing directions. The expanding speed of the leading point is faster than the trailing point, and at a moment, the leading point reaches the leading edge of the ring. The throttle effect of the ring to the oil flow can be detected through the decrease of the oil film thickness at the trailing edge as time going (x/B=1 in Figure 4-9). As liner movement getting slower and the ring approaching the liner getting faster, the squeezing effect becomes dominant. From Figure 4-9, it can be seen that, because of the squeezing effect, fully-filled region expands towards the trailing edge at the end of the time series. The pattern of pressure distribution also changes, with the location of maximum pressure moving towards the center of the ring, as illustrated in Figure 4-10.

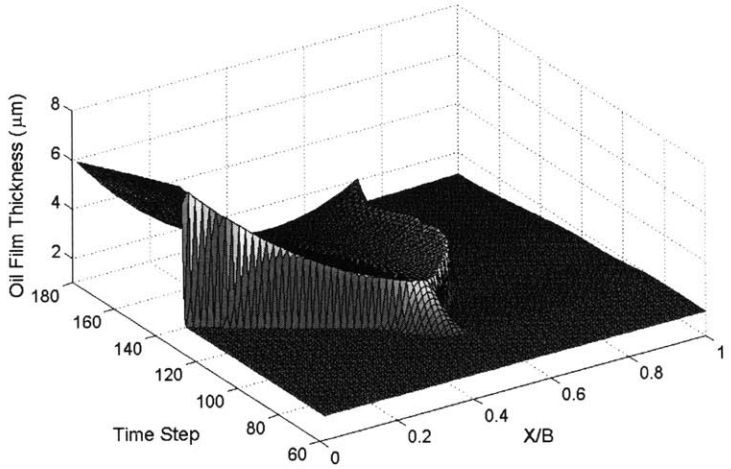

Figure 4-9 Evolution of oil film thickness at the condition of small pressure difference

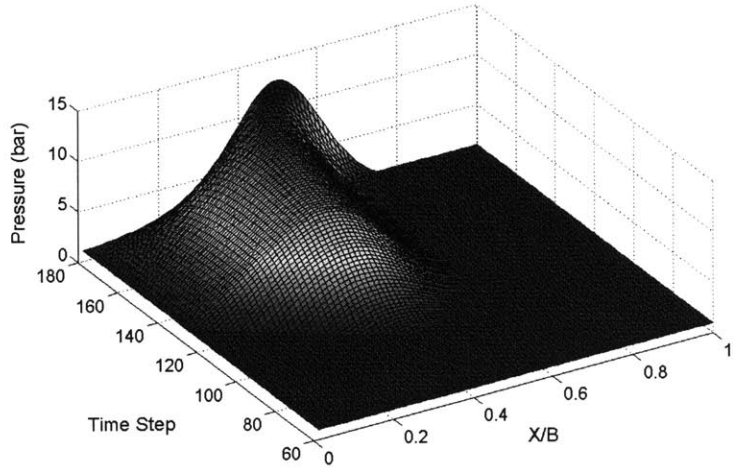

Figure 4-10 Evolution of oil film pressure at the condition of small pressure difference

To test the performance of the model when the pressure difference between the leading and trailing edge of the ring is large, the pressure at leading edge is set to be 10bar and that at trailing edge is still kept as 1bar. The oil film thickness and pressure are shown in Figure 4-11 and Figure 4-12, respectively. As can be detected, even before the minimum ring/liner is less than two times of oil film thickness, the oil film thickness beneath the ring is not uniform. The region, which is assigned to have linear distribution of standard pressure, has smaller oil film thickness due to the influence of the pressure gradient. Then, the two boundary pointes of this region become the potential locations where the oil starts to accumulate because they have the smallest ring/oil clearance. As a result, two separate fully-filled regions build up and a partially-filled region exists in between. Eventually, a single fully-filled region forms when the two fully-filled regions connect to each other, and the rest evolution is similar to the case without pressure difference between the leading and trailing edge.

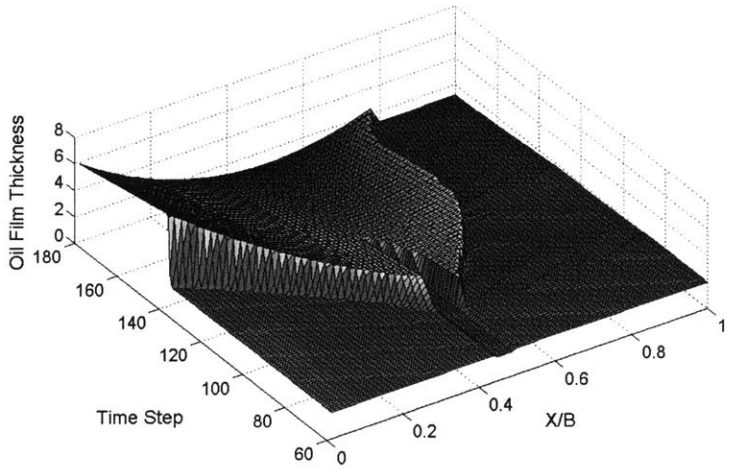

Figure 4-11 Evolution of oil film thickness at the condition of large pressure difference

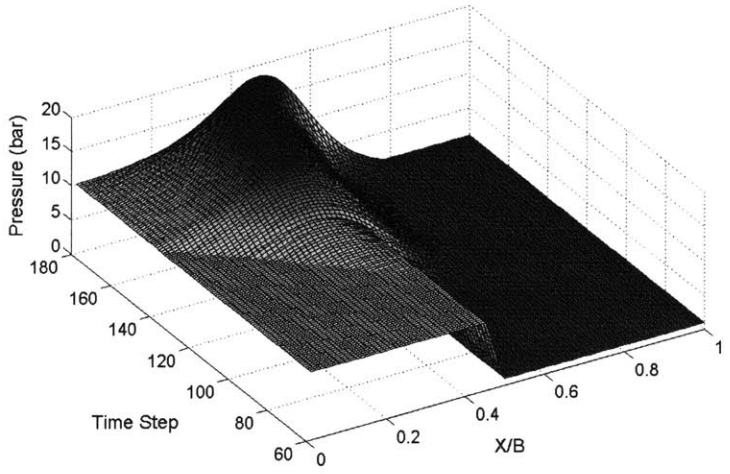

Figure 4-12 Evolution of oil film pressure at the condition of large pressure difference

It is worthy of noting that the thorough physics involved in the oil-reattachment is yet to be known. The whole scenario demonstrated by the model results is only the outcome of how the model is set up, and is not physics based. Fortunately, the oil-reattachment is not or only shortly encountered in an engine cycle. For a numerical model simulating the ring lubrication and oil transport, it is more important to satisfy the flow continuity and at the same time have stable and converged solution. By making those improvements on the algorithm initiated in [46], current model well achieved this task.

The model setup ensures the satisfaction of flow continuity. To exam if this goal is accomplished, several volume quantities are listed in Table 1. Since only one cross-section is investigated, these

quantities are all in unit of area (μm^2). If flow continuity is satisfied, there should exist an equation that relates the total inlet oil, the total outlet oil, the change of oil between the ring and liner, and the oil scraped and accumulating on the leading edge of the ring, that is

$$\delta V = V_{inlet} - V_{outlet} - \Delta V_{ring-liner} - V_{scrape} = 0 \tag{4.18}$$

As listed in Table, we can see that, in both cases, the flow continuity is well satisfied.

Table 4-1 Verification of flow continuity

	V_{inlet} (μm^2)	V_{outlet} (μm^2)	$\Delta V_{ring/liner}$ (μm^2)	V_{scrape} (μm^2)	δV (μm^2)
Case 1	114090.8	108651.1	-102.3	5542.0	0.0
Case 2	114090.8	110055.3	61.2	3976.2	-1.9

4.2.4 Conclusions

A flow continuity algorithm is implemented in modeling the ring/liner hydrodynamic lubrication. Compared to the literature, different equation was proposed in the partially-filled region based on experimental findings. A transition region was introduced to deal with the flow discontinuity between the fully-filled and partially-filled regions. The present model is then able to resolve all the possible lubrication conditions and transitions between them seamlessly. The experience of implementing and applying this model reveals its following advantages:

- In this model, oil flow mass conservation is always preserved in the entire ring/liner interface that includes partially-filled and fully-filled regions. Doing so avoids difficulties involved in switching among different boundary conditions needed when using traditional Reynolds equation.
- Introduction of a transition region is essential to the robustness of the model without violating oil mass conservation.
- Preserving oil mass conservation ensures a precise oil transport simulation and lays a solid base for oil transport and oil consumption analysis.
- It is a well defined numerical system. Its consistent performance in all kinds of lubrication situations makes it possible to have a robust ring-pack model.

4.3 Ring-Pack Lubrication Model

4.3.1 Introduction

During an engine cycle, ring lubrication and ring dynamics are linked to each other. The lubrication friction is an important component of the axial forces that affect the ring lift motion. While the ring dynamic twist changes the relative angle between the ring running-surface and the liner surface continuously, and has a great impact on the ring/liner lubrication. In addition, the inter-ring gas pressures determined by ring dynamics are crucial boundary conditions for ring/liner lubrication. The most ideal and accurate modeling approach is to couple the lubrication and dynamics together. However, this will lead to a rather complicated and time consuming model. The insights into the relationship between the two aspects of ring performance reveal that the influence of lubrication on dynamics is relatively weak. If a reasonable estimation of ring/liner friction is used in the simulation of ring dynamics, fairly accurate results can be achieved as shown in Chapter 3 and [50]. After the dynamic behaviors of the ring are obtained, the dynamic twist angle and the inter-ring gas pressures can be used as input for the simulation of ring lubrication. This modeling strategy of separating ring lubrication with ring dynamics ensures very efficient simulation, and at the same time largely preserves the calculation accuracy.

In this section, the one-dimensional hydrodynamic lubrication sub-model developed in Chapter 4.2 and [51] is implemented. A detailed elastic analysis performed by finite element method is used to model the ring structure response to the distributed forces on the ring. By coupling the ring lubrication with the ring structure response, current ring-pack lubrication model is capable of predicting the lubrication variations along the circumference in an accurate and efficient manner.

In the following, the model development is described first. Then, this model is applied to a light-duty diesel engine and the effects of ring twist, bore distortion, and piston tilt motion on the lubrication and oil transport are discussed in details.

4.3.2 Model Formula

Ring/Liner Conformability

After resolving the ring dynamic twist and inter-ring gas pressures by using the 3-D ring dynamics model, only ring in-plane structural response needs to be coupled with ring/liner lubrication. As illustrated in Figure 4-13, a ring will deform under the impact of the lubrication force from the liner and the gas pressure from the ring back. Its in-plane displacements determine the clearance between the ring running-surface and the liner surface, which is called ring/liner conformability. In order to resolve the relationship between the displacements and the external forces, finite element analysis is performed.

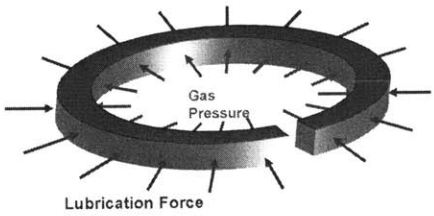

Figure 4-13 Force acting on a ring

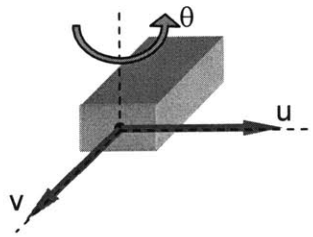

Figure 4-14 Three degrees of freedom on a ring cross-section if only in-plane displacements are considered

The ring is first discretized circumferentially into straight beam elements, and the degrees of freedom (DOF) at all of the cross-sections are the unknowns to be solved. When the in-plane displacements are of interest, which is the case in this study, only three DOFs need to be considered: linear displacement in radial direction u, liner displacement in circumferential direction v, and angular displacement in axial direction θ, as shown in Figure 4-14.

The diameter of a ring at its free state is larger than the bore size. In this study, the ring is initially compressed to a circular shape with the outer diameter as the bore size. To maintain this shape, radial

forces are needed to act on the ring, which are called initial loads in this study. For general purposes, a uniform initial load distribution, which can be derived from the specified tangential force of the ring, can be used. For more in-depth analysis that involves the specification of the free shape of the ring, the analytical tool for piston ring design that was developed in Chapter 2 and [36] can be employed to get the initial load distribution.

The ring deforms under the effects of lubrication forces and gas pressure, and the governing dynamic equation in the finite element format is:

$$M\ddot{U} + KU = S(U) - S_I \tag{4.19}$$

where U is a vector consisting of the displacements of the DOFs of all the cross-sections (u_1 v_1 θ_1 ... u_N v_N θ_N), $\ddot{U}$ a vector of the second order derivative of the displacements, M the mass matrix, K the stiffness matrix, S the load vector including all the radial forces acting on ring surface, and S_I a vector of initial loads. The details of how to set up the stiffness matrix K are described in [36] and [28], and are not repeated here.

To solve the equation, the radial forces need to be evaluated firstly. If the ring/groove friction is negligible, which is suitable for most of the time, the radial force is generated by several kinds of pressure acting on the ring surface, as shown in Figure 4-15. It is straightforward to calculate the force applied on the back of the ring, while the forces acting on the ring running-surface need further analysis. There are three kinds of pressure that may act on the ring running-surface: gas pressure, asperity contact force, and hydrodynamic lubrication force. The portion of the ring running-surface that exposes to the adjacent piston land is considered to be applied by the land pressure (P_1 and P_3 in Figure 4-15). The asperity contact force, if existing, is calculated by the asperity contact model described in Chapter 2, while the hydrodynamic lubrication force can be calculated by the hydrodynamic lubrication model introduced earlier in this chapter.

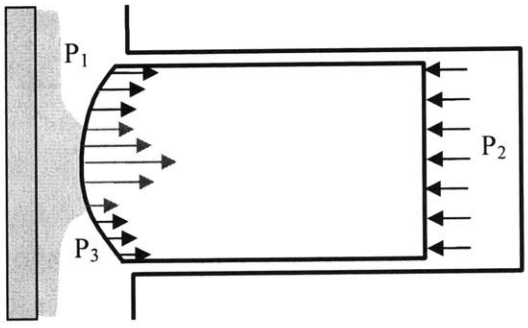

Figure 4-15 Forces acting on the ring surface

Estimation of Ring/Liner Friction

The axial friction force on the ring running-surface is considered to consist of two components: the hydrodynamic lubrication friction due to the viscosity of the lubrication oil, and the boundary lubrication due to the asperity contact. For the friction of hydrodynamic lubrication, as described in Chapter 4.2 and [51], once the pressure gradient of the oil in the ring/liner interface is obtained, the shear stress and in turn the friction force on the ring running-surface can be evaluated. The friction force of boundary lubrication can be estimated through multiplying the asperity contact force by a friction coefficient of boundary lubrication (0.1 is used in this study). The summation of these two components is the total friction force on the ring running-surface.

Oil Film Thickness on the Liner

Ring/liner lubrication is largely determined by the inlet oil film thickness encountered by a ring at a location of the liner. The oil film thickness on the liner changes after the ring passes by, and some oil can be transported by the ring from one place to another along the liner. To conduct an accurate analysis of ring/liner lubrication and oil transport, the oil film thickness on the liner needs to be tracked precisely.

In this study, a mesh is generated on the liner surface, and the oil film thickness at each grid point is tracked momentarily in an engine cycle. As shown in Figure 4-16, during one calculation step, the average oil film thickness of the grid points passed by the leading edge of a ring is used as the inlet oil film thickness for this ring. Meanwhile, the outlet oil film thickness is assigned to all of the grid points passed by the trailing edge during the same calculation step. Due to the sufficient oil supply from the oil splashing, the portion of the liner that is below the oil-control ring will be covered with fresh oil, and thus, the oil film left by the oil-control ring during upstrokes need not to be tracked.

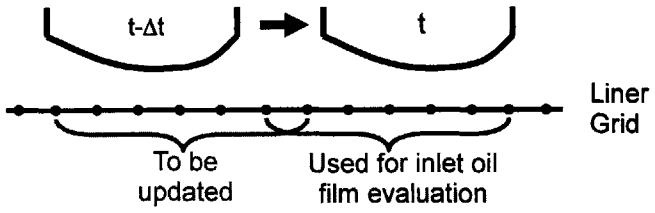

Figure 4-16 Oil film tracking on the liner

Computation Algorithm

To solve the governing Equation (4.19), the following implicit integration scheme is implemented to achieve numerical stability:

$$(\frac{M_m}{\Delta t^2} + K_m)U_m^t = S_m^t + \frac{M_m}{\Delta t^2}U_m^{t-\Delta t} + \frac{M_m}{\Delta t}\dot{U}_m^{t-\Delta t} - S_{I,m} \qquad (\text{m} = 1, 2, 3) \qquad (4.20)$$

The above equations are nonlinear and Newton's method with a globally convergent algorithm is used to solve them numerically. The Jacobian matrix in the Newon's method is band diagonal, and the efficient solver for linear equations described in [35] is employed to calculate the increment in each Newton loop.

Simplification of the Ring-Pack

The piston ring-pack in modern production engines usually consists of two compression rings and one oil-control ring. With its narrow land width, high tension and low bending stiffness, an oil-control ring can conform to the liner surface very well, even with large bore distortion existing. During downstrokes of an engine cycle, the oil film thickness passing through the oil-control ring is quite small. If this oil is the only oil supply for the second compression ring, the lubrication for the top two rings are highly starved [4].

There are several other possible oil supplies for the second ring in some operation conditions. In [27], a large amount of oil was detected on the third land of piston. This oil can travel upward under the influence of inertia force, and reaches the lower side of the second ring. The oil can then move to the liner, with the second ring playing as a "bridge". If the oil film on the third land is thick enough, some oil can even go to the liner directly. As also discovered in [27], some oil can pass through the end-gap of the oil-control ring, without being scraped by the ring rails. This amount of oil can become a direct oil supply to the second ring. Although the large oil supply is not the situation for the entire circumference of the second ring, the localized phenomenon is still worthy of investigation.

In this study, the leading edge of the second ring is assumed to be always flooded during the intake and expansion strokes to simulate the situation of maximum oil supply to the second ring.

4.3.3 Sample Results

This model was applied to a light-duty diesel engine, which comprises two compression rings and a twin-land oil-control ring. The specifications of the engine and the top two rings, as well as the operation conditions are presented in Table 4-2. The piston tilt motion and the cylinder gas pressure, which are needed for both the dynamics and lubrication simulation, were from calculation and measurement, respectively, and are shown in Figure 4-17. In the piston tilt trace, the positive angle of the piston tilt motion means piston is tilting toward the anti-thrust side.

Table 4-2 Engine specifications

Bore Diameter	85 mm
Stroke	96 mm
Connecting Rod Length	152 mm
Speed	4000 rpm
Load	Full
Top Ring Face Profile (symmetric barrel shape)	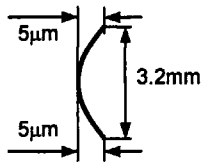
2nd Ring Face Profile (tapered shape)	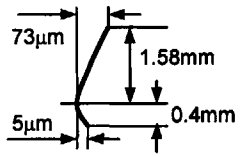

The dynamics model developed in Chapter 3 and [50] was used to predict the twist angles of the piston ring-pack and the inter-ring gas pressures. The twist angles of the top and the second ring are shown in Figure 4-18 and Figure 4-19, of which the positive value refers to the twist angle generated by the ring back moving down and the ring running-surface moving the up. It can be seen that the twist angles of both rings change with time, but the twist angle of top ring is smaller than that of the second ring. It can also be seen that, unlike the top ring, the twist angles of the second ring vary significantly along the circumference.

The inter-ring gas pressures also vary along the circumference, but with small magnitude. For simplicity, the average inter-ring pressures along the circumference were used in the calculation, as shown in Figure 4-20.

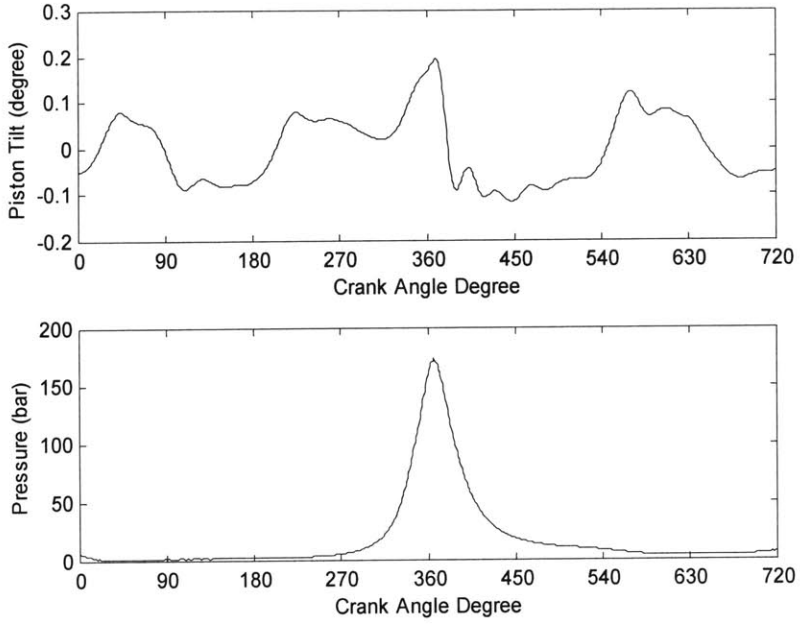

Figure 4-17 Measured piston tilt motion and cylinder pressure

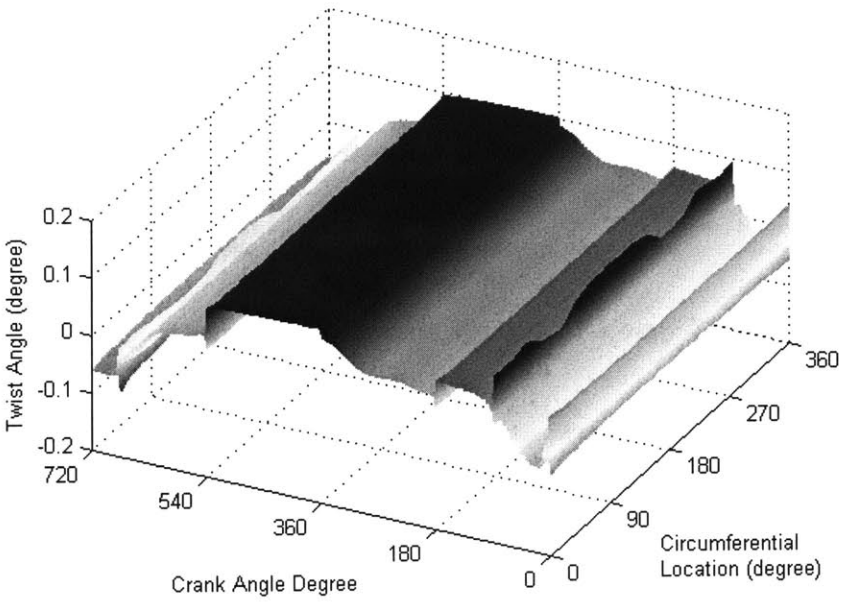

Figure 4-18 Twist angle of the top ring calculated by ring dynamics simulation

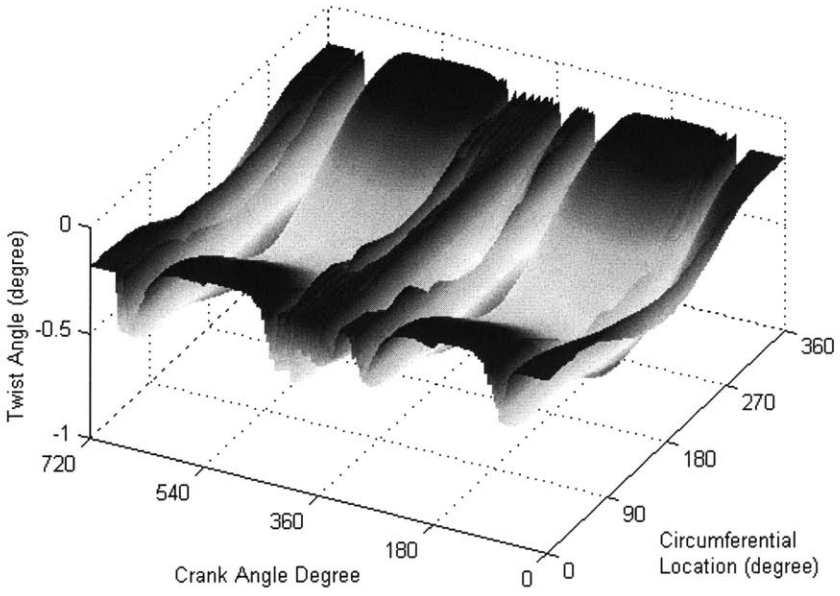

Figure 4-19 Twist angle of the second ring calculated by ring dynamics simulation

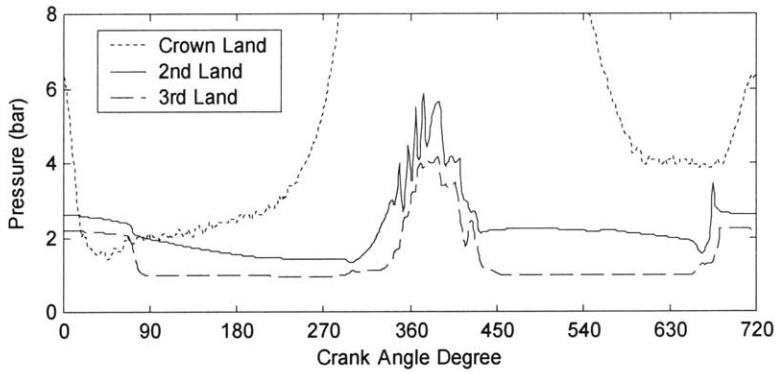

Figure 4-20 Average inter-ring gas pressure

To illustrate the effects of different factors, such as piston tilt, ring twist, and bore distortion, on the ring lubrication, the ring-pack lubrication model was tested in several circumstances with switching on or off some isolated factors. It needs to be clarified that, for all the cases, the same inter-ring pressures were used, and the two ring gaps were all fixed at the thrust side.

Baseline

A baseline case was set up first by not considering the piston tilt motion, ring twist and bore distortion. The oil film thickness on the liner in the "dry region", which is defined in this study to represent the liner region above the TDC location of the second ring, was initially set to be zero. As can be anticipated, the oil will be gradually transported to the dry region and the lubrication in this region will change from cycle to cycle. In order to see if finally a steady state can be reached, the model was allowed to run for 100 cycles. When all of the key factors that can bring on significant variations along the circumference don't exist, the ring lubrication behaves similarly to the axisymmetric cases that 2-D models simulate. Although small differences exist for different circumferential locations due to the existence of the ring gap, the results shown in this section, which are for the anti-thrust side, are quit representative for the entire circumference.

The oil film thickness on the liner at the end of expansion stroke of each cycle was recorded, and the results of selected cycles are shown in Figure 4-21. It can be found that, below the dry region, the oil film thickness reaches steady state very quickly. This is due to the repeating oil supply from below that makes the leading edge of the second ring fully flooded during downstrokes. While in the dry region, the oil film thickness keeps increasing, and then does not change after about 80 cycles. This implies that a steady state can be reached. It is very important to identify the existence of the steady state, as it decides the oil film thickness in the dry region and sequentially determines the top ring friction when it is traveling in this region.

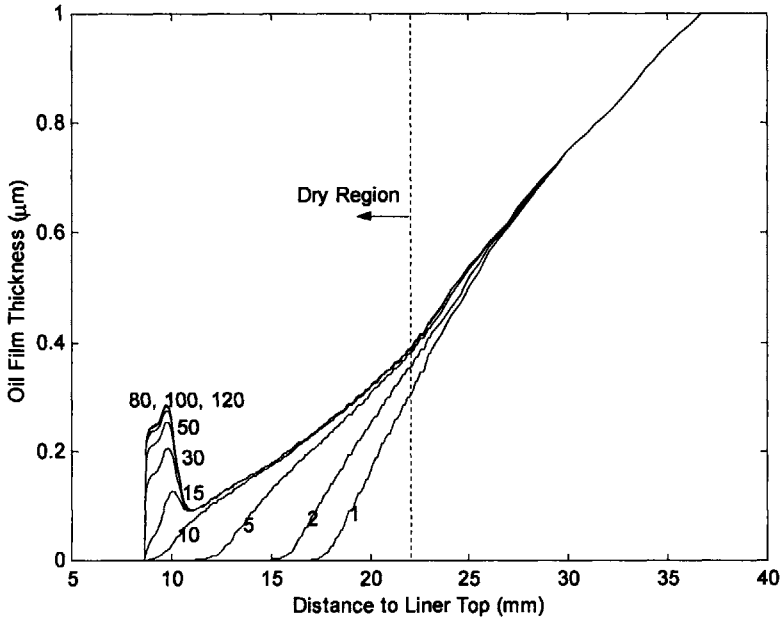

Figure 4-21 Evolution of oil film in the dry region in baseline condition

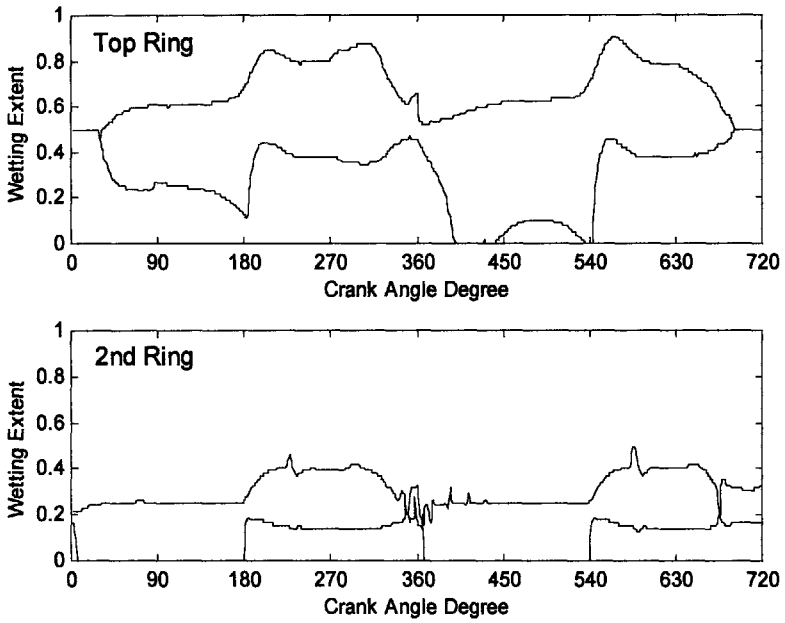

Figure 4-22 Wetting extents of top two rings in baseline condition

The wetting extents of top two rings, which represent the regions on the ring running-surface fully-filled by oil, are shown in Figure 4-22. In this figure, "0" at the y axis refers to the lower edge of the ring running-surface, "1" denotes the upper edge, and between the two lines is the region fully-filled by the oil. From the wetting extent of the second ring, one can see that, as the given boundary condition, the lower edge of the second ring is always fully flooded during downstrokes. Due to the tapered shape of the running-surface profile of the second ring, the wetting region is rather narrow throughout the entire engine cycle. It can also be noticed that, around 360 CAD, the wetting extent has intense fluctuation; at some moments, the wetting extent even shrinks to zero, which means that the ring running-surface loses contact with the oil. The cause of this phenomenon was identified to be the ring-collapse: around the 360 CAD, the upward inertia force pushes the second ring against the upper flank of the groove; the pressure in the second land is greater than that in the second groove; the taper face profile of the second ring leaves a large portion of running-surface exposing to the high pressure of the second land, and the ring is pushed away from the liner. The minimum clearance between the two rings and the liner surface are shown in Figure 4-23, from which the large clearance between the second ring and the liner because of the ring-collapse can be immediately detected. The detailed description of ring-collapse can be found in [3].

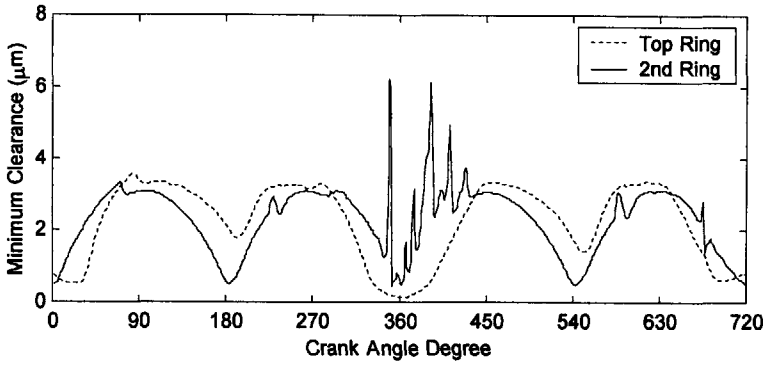

Figure 4-23 Minimum ring/liner clearance of top two rings in baseline condition

From the wetting extent of the top ring, one can see that, for most of the time, the ring is undergoing starved lubrication. During a short period of time in the expansion stroke, because of the high pressure acting on the top ring back and a large amount of oil left by the second ring due to the ring-collapse, the lower edge of the top ring becomes flooded and down-scraping of oil occurs. In this model, the scraped oil is assumed to keep accumulating, without going back to the liner. Based on this assumption, the total oil scraped by top ring lower side during expansion stroke is $5.77mm^3$. If some of this oil enters the top ring groove, it may move further up to the crown land and easily contribute to the oil consumption.

To further analyze the oil transport along the liner, the liner oil film thickness after the top ring passes by in all of the four strokes are shown in Figure 4-24. The comparison between the oil film thickness of the intake and compression stroke reveals that, in the lower region of the liner, the oil film of the intake stroke is thicker than that of the compression stroke, but in the upper region of the liner, the compression stroke has thicker oil film. The same finding can be observed for the expansion and exhaust stroke, which implies that some oil is transported by the top ring to the upper region of the liner during upstroke. Because the temperature in the upper liner region is higher than the lower liner region, and the oil transported from lower liner region is fresh, the oil evaporation will be enhanced and then contribute to the oil consumption.

In Figure 4-24, an oil film valley is detected around the bottom dead center of the ring for both compression and exhaust strokes. This implies that some oil left by the ring during previous downstroke is carried by the ring to the upper liner region during the upstroke. The inertial motion of the top ring is found to be the cause of the valleys. As can be seen in Figure 4-23, for the top ring, it is not the bottom dead center when minimum ring/liner clearance occurs. There is about 15 CAD delay at both BDC. Close to the BDC of downstrokes, the sliding speed of the ring decreases greatly and the

ring starts to squeeze the oil film. Due to the inertia effect, the squeezing motion continues to the following upstroke and leaves a valley on the oil film.

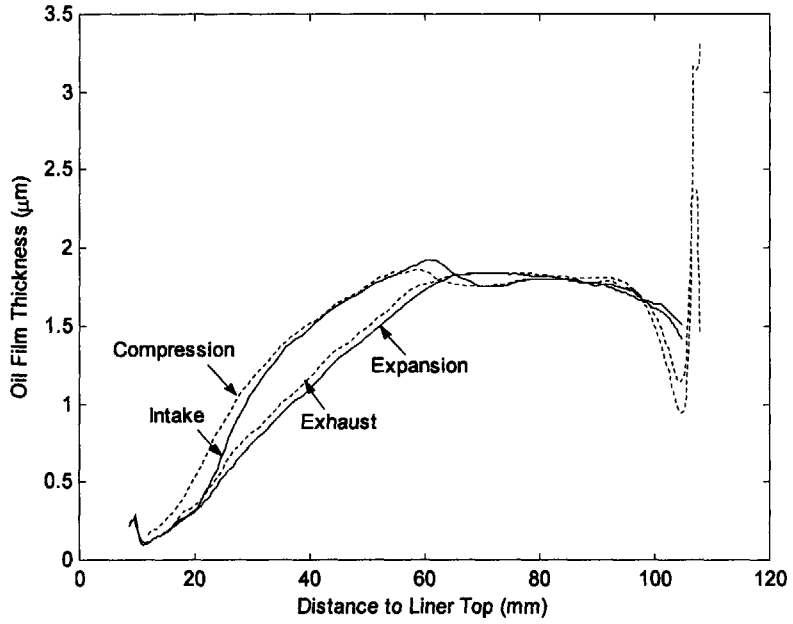

Figure 4-24 Liner oil film thickness after the top ring passes in four strokes in baseline condition

Effects of Piston Tilt Motion

Piston tilt motion influences both ring dynamic and lubrication behavior. Its effects on ring dynamic have been detailed in Chapter 3 and [50] and will not be repeated here. For ring lubrication, the piston tilt induces various relative angles between the ring running-surface and liner surface along the circumference. Figure 4-25 shows the wetting extents of the top ring at the thrust and anti-thrust side, between which the largest differences are supposed to exist. As can be seen, the wetting extent at these two locations differs greatly from each other. Because of the positive piston tilt (shown in Figure 4-17) during compression and exhaust stroke, the leading edge of wetting extent is closer to the upper edge of the ring at the anti-thrust side than thrust side. In a short period of time of the exhaust stroke, even up-scraping of oil happens at the anti-thrust side. During the expansion stroke, piston tilts toward the thrust side, and the time duration of the down-scraping of oil is longer at the anti-thrust side than thrust side. These differences imply that, because of the piston tilt motion, it is easier for the ring at the anti-thrust side to scrape oil in either up or down direction.

Because of the characteristics of the face profile of the second ring used in this study, the ring/liner relative angle induced by piston tilt can not shift the axial location of minimum point too much, and the influence of piston tilt on the wetting extent of the second ring is small.

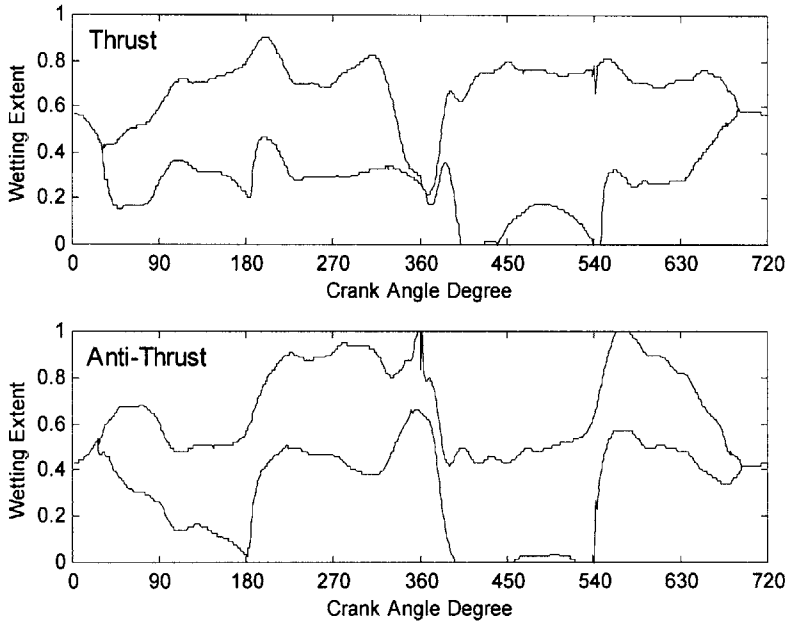

Figure 4-25 Wetting extents of top ring at anti-thrust and thrust side in piston tilt condition

Effects of Ring Twist

When the twist angles of the top and second ring (shown in Figure 4-18 and 4-19) are considered, the relative angles between the ring running-surface and the liner surface are changed compared to the baseline case. The lubrication of the second ring is greatly influenced by its negative twist angle. As a result, more oil can pass through the second ring and becomes available for the top ring during the expansion stroke. Additionally, the positive twist angle of the top ring during the expansion stroke, although with small magnitude, makes the top ring to scrape oil more easily. As a result, the oil scraped by the top ring during the expansion stroke ($17.53mm^3$) is more than the baseline case ($5.77mm^3$).

As shown in Figure 4-19, the magnitude of the negative twist angle of the second ring has the largest value at the back point and the smallest value at the end tips. To clearly demonstrate the difference, the twist angles at the ring tips and the back point, which in this study coinciding with the thrust and anti-thrust side, respectively, are plotted in Figure 4-26. The difference of the twist angle induces different wetting extents at these two locations: as shown in Figure 4-27, the wetting extent of

the second ring during downstrokes at the anti-thrust side is relatively wider than that of the thrust side. Correspondingly, the minimum clearance between the second ring and the liner surface at the anti-thrust side is greater than that of the thrust side, as is illustrated in Figure 4-28. As a result, the oil film passed by the second ring during the expansion stroke is thicker at the anti-thrust side, which induces more down-scraping of oil by the top ring at the anti-thrust side.

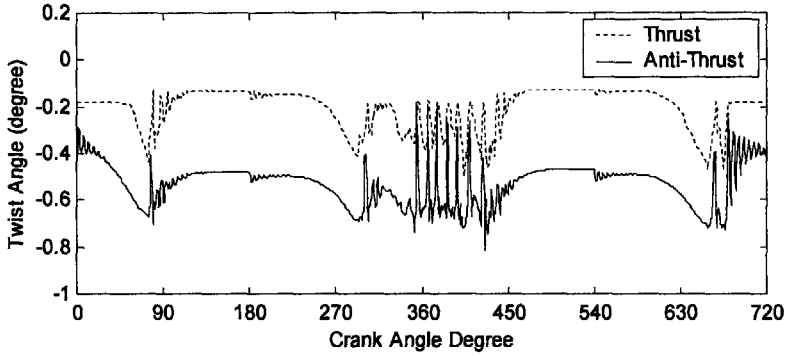

Figure 4-26 Twist angles of the second ring at the thrust and anti-thrust side

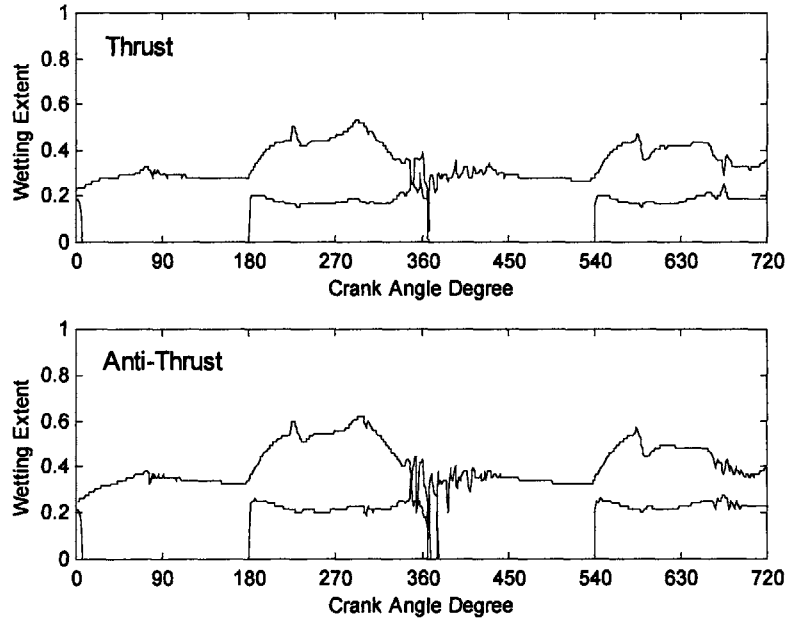

Figure 4-27 Wetting extents of the second ring at the thrust and anti-thrust side in ring twist condition

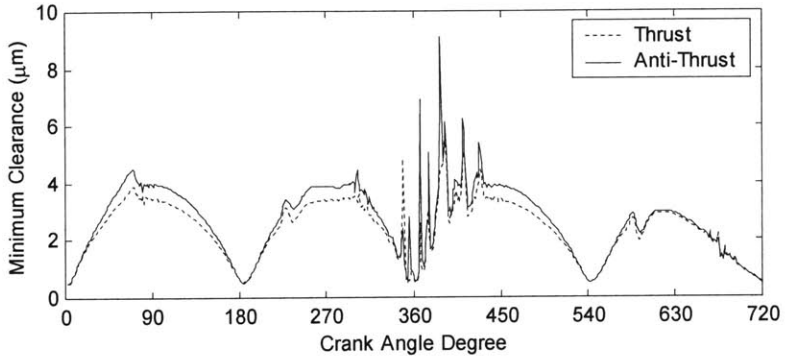

Figure 4-28 Minimum clearance of the second ring at thrust and anti-thrust side in ring twist condition

Effects of Bore Distortion

Bore distortion is usually depicted by a Fourier series that comprise different orders. Along the axial direction of the liner, bore distortion can vary from one location to another. Although current model is capable of dealing with all of the bore distortion cases, in this study, only the fourth order bore distortion was considered and the bore shape was assumed to be the same along the axial direction. The fourth order bore distortion is generally seen due to the bolting of the cylinder head, and is usually a major concern for ring/bore conformability. The amplitude of the fourth order was set to be 6μm, which means the largest deviation of the distorted bore from roundness is 6μm, as illustrated in Figure 17. During engine operation, the end-gaps of both rings were assumed to stay at the circumferential location of 0 degree (one of the four valleys).

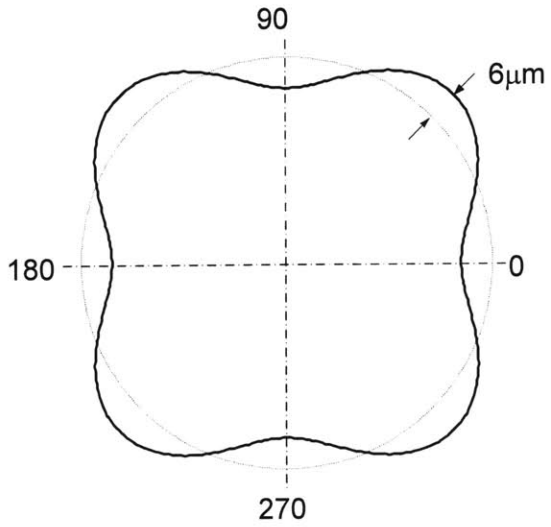

Figure 4-29 Bore shape with 4th order distortion

The calculated minimum ring/liner clearance for the top and the second ring are shown in Figure 4-30 and Figure 4-31, respectively. It can be clearly seen that, corresponding to the fourth order of bore distortion, the minimum ring/liner clearance for both rings has four peaks and four valleys throughout the entire engine cycle. It can also be seen that ring-collapse happens for both rings. When the ring-collapse occurs, the difference between the peak and valley of the ring/liner clearance is much greater than no ring-collapse situation. The explanation for this phenomenon is illustrated in Figure 4-32: without ring-collapse, a ring tends to conform to the distorted bore under the help of its self-tension and the gas pressure acting on its back, and the difference of the ring/liner clearance along the circumference is small; once the ring-collapse occurs, the ring shape becomes almost circular, and the clearance differences along the circumference turns out to be much greater. This means that, when ring-collapse happens, the existence of bore distortion may increase the gas leakage, compared to the situation without bore distortion.

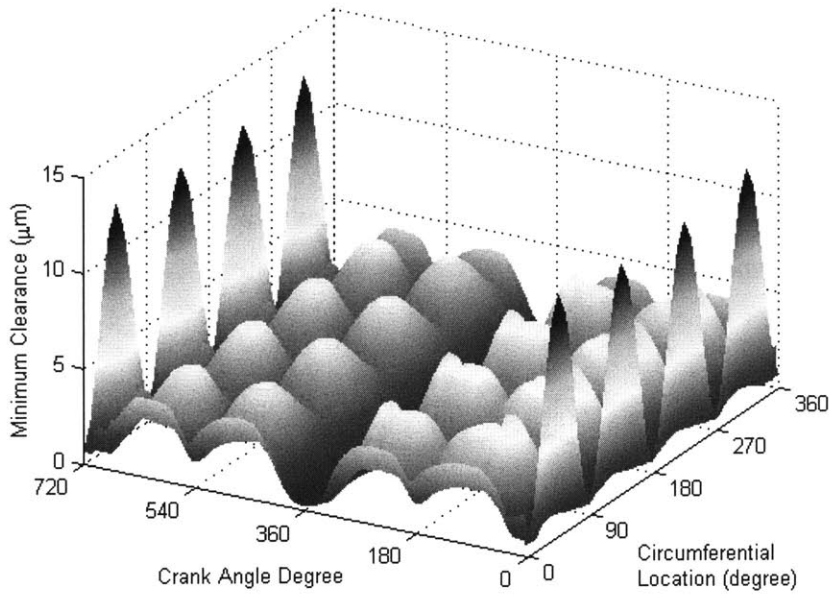

Figure 4-30 Minimum clearance of top ring in bore distortion condition

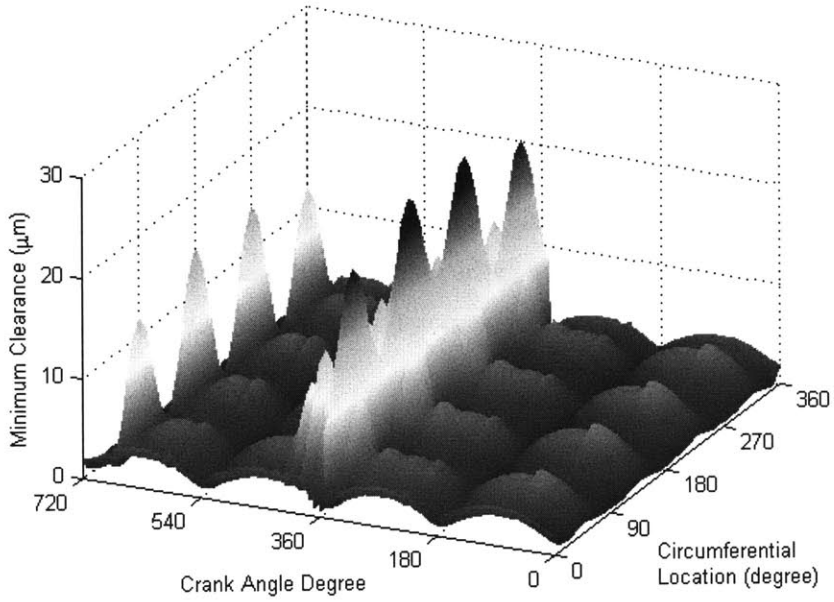

Figure 4-31 Minimum clearance of the second ring in the condition of bore distortion

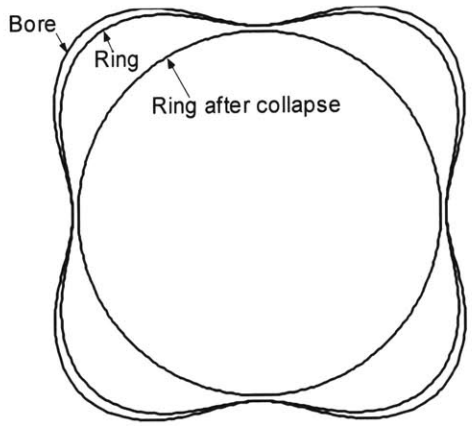

Figure 4-32 Illustration of the effects of ring-collapse on ring/liner clearance

The wetting extents of the top ring at the locations of 135 degree (called location 1) and 180 degree (called location 2) are shown in Figure 4-33. The situation of leading edge flooded and hence the up-scraping of oil by the top ring can be detected during the compression stroke at location 1, but not at location 2. This is because, at location 1, there is a large amount of oil left by the top ring during the intake stroke due to the peak of bore distortion at this location. During the compression stroke, gas

pressure behind the top ring keeps increasing, pushing the ring move closely to the liner, and up-scraping of oil happens eventually. The distribution of the oil scraped by the upper edge of the top ring at the end of compression stroke is shown in Figure 4-34. It can be seen that the peaks of the oil-scraping correspond exactly to the peaks of the bore distortion. From Figure 4-33, one can also see that, during expansion stroke, the situation of leading edge flooded and hence the down-scraping of oil occur in a longer time period at location 1 than location 2. This is because that more oil passes through the second ring at location 1 due to the reduced conformability at this location. As a result, the down-scraping of oil by the top ring at location 1 is more than location 2, as illustrated in Figure 4-35.

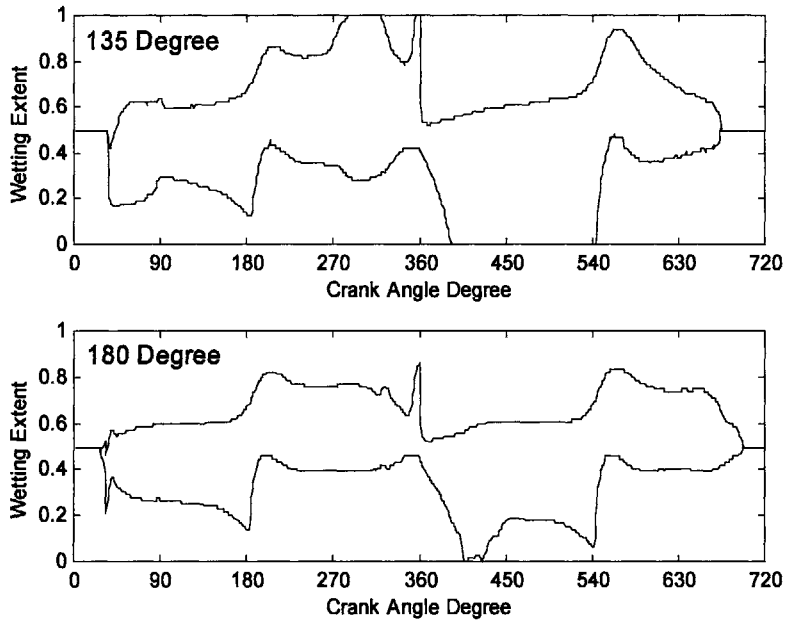

Figure 4-33 Wetting extents of the top ring at 135 and 180 degrees from the end-gap in the condition of bore distortion

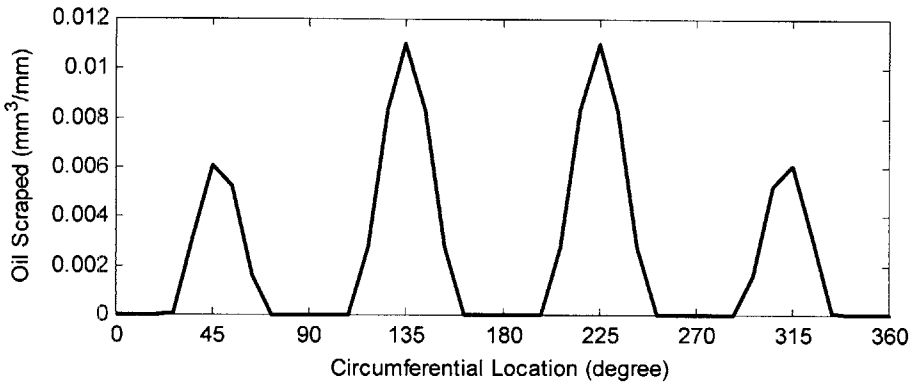

Figure 4-34 Distribution of oil up-scraped by the top ring at the end of compression stroke in the condition of bore distortion

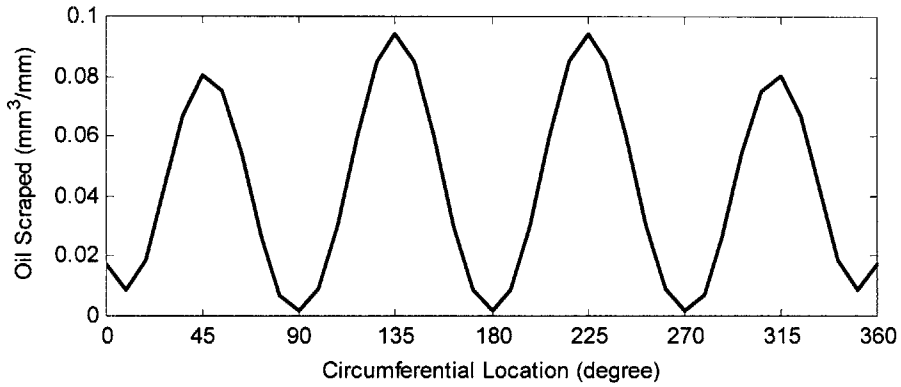

Figure 4-35 Distribution of oil down-scraped by the top ring at the end of expansion stroke in the condition of bore distortion

The oil film thickness on the liner at location 1 after the top ring passes by in all of the four strokes are shown in Figure 4-36. Similar observations of oil transport can be made as baseline case. However, much thicker oil film is detected in the intake stroke. The large discrepancy of the oil film thickness between the intake and compression stroke indicates that significant oil is transported by the top ring through either scraping to the upper edge of the top ring or pushing to the upper region of the liner.

Several other amplitudes of the fourth order bore distortion were also studied. Emphases were placed on the scraping of oil by the top ring. As shown in Figure 4-37 and Figure 4-38, both the up-scraping during the compression stroke and the down-scraping during the expansion stroke increase with the amplitude of the fourth order bore distortion

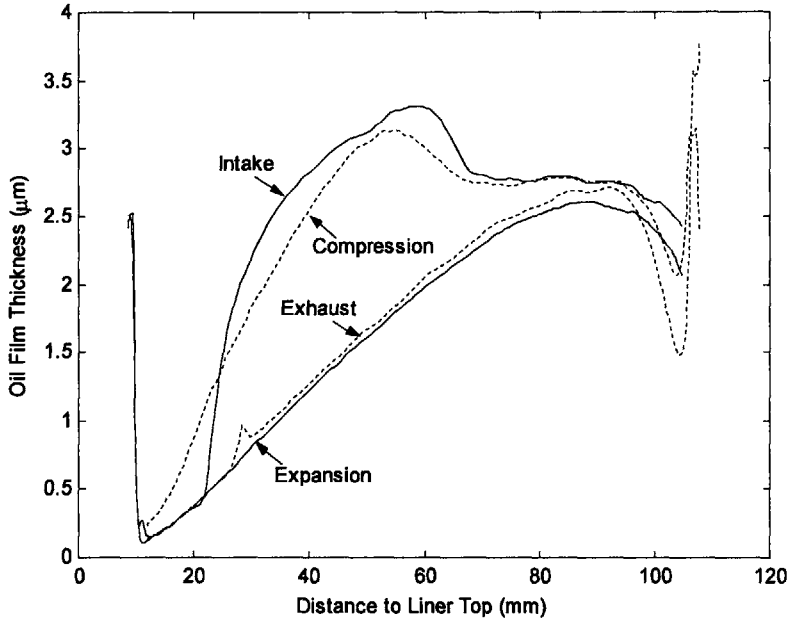

Figure 4-36 Liner oil film thickness after the top ring passes in four strokes in the condition of bore distortion

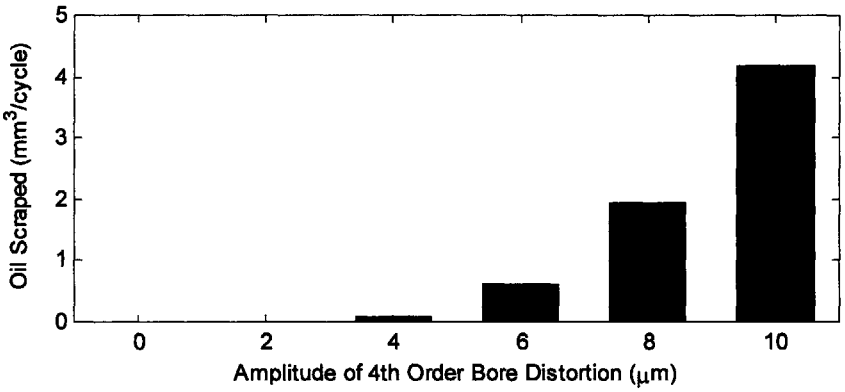

Figure 4-37 Oil up-scraped by the top ring in the conditions of different bore distortion

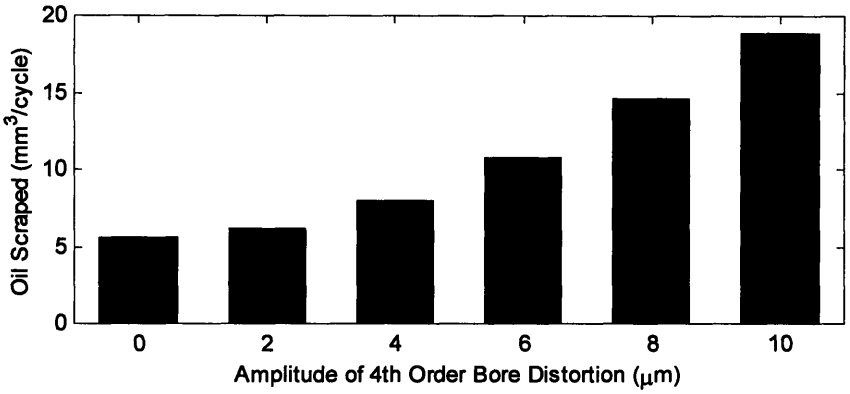

Figure 4-38 Oil down-scraped by the top ring in the conditions of different bore distortion

4.3.4 Conclusions

By coupling ring structural analysis and an improved hydrodynamic lubrication theory, a comprehensive ring-pack lubrication model has been developed. It is computationally robust and efficient, and hence has appreciable practical values.

This model was applied to a light-duty diesel engine, and has demonstrated its capability of simulating the variations of ring/liner lubrication along the circumference. The key points drawn from the model application are as follows:

- The distribution of oil film thickness on the liner can reach a steady state, which gives a consistent base for the estimation of friction and oil evaporation
- Model results shows significant variations of ring/liner lubrication along the circumference due to the effects of piston tilt motion, ring twist and bore distortion, which proves the necessity of current non-axisymmetrical approach.
- Because of piston tilt motion, scraping of oil by the top ring, in both up and down directions, was observed to be different from the anti-thrust side to thrust side.
- Bore distortion was found to have profound effects on the oil transport along the liner. Particularly, it stimulates the occurrence of the up-scraping of oil by the top ring during the compression stroke. Both up and down-scraping of oil by the top ring were found to increase with the amplitude of bore distortion.

Because of the precise consideration of the flow continuity of lubrication oil in current model, a fairly reasonable oil transport simulation is achieved. To further utilize these results in oil consumption analysis, an oil evaporation model appears to be very necessary. The dynamic coupling of the oil transport and oil evaporation will provides more insights into the mechanisms of oil consumption in internal combustion engines.

Chapter 5 Modeling Oil Evaporation on Cylinder Liner

5.1 Introduction

The oil film on the liner is in relatively high temperature condition. When it is exposed to moving in-cylinder gases, significant evaporation occurs. Oil vapor is presumed to join cylinder gases and leave the engine as either partially burned or unburned hydrocarbons. Experimental studies have demonstrated the significance of oil volatility and liner temperature on oil consumption, which implies the contribution of the oil evaporation to the overall oil consumption [52-55, 63].

Several numerical models for the evaporation of oil from the liner have been presented in an attempt to establish which physical mechanisms and which design parameters most strongly influence oil evaporation [55-57, 63]. In most of these models, the oil evaporation process is treated as the diffusion of oil vapor through a gas boundary layer on the liner surface. The oil itself is modeled as being composed of several distinct hydrocarbon species each with its own boiling point and associated vapor pressure. Overall oil evaporation is computed by calculating the local instantaneous oil vapor mass flux for numerous locations on the liner, integrating over time and space, and summing over the number of oil species.

Due to the temperature distribution along the liner, the composition of the oil varies from location to location along the liner. To address this concern, Yilmaz et al. [55, 63] tested several different composition distributions along the liner, and found that the model results predicted by the distribution considering depleted lighter oil species mach the experimental measurement better. Since the oil composition varies along the liner, the oil transport by the ring movement can alter the composition. Audette et al. [57] calculated the change in oil composition due to ring passage by using a simplified mass conservation model. Both works demonstrated the importance of considering the variation of oil composition along the liner in predicting oil evaporation.

The ring-pack lubrication model described in the previous chapter is capable of computing the oil transport along the liner in a precise manner, which enables an accurate evaporation prediction. Meanwhile, the 3-D feature of this lubrication model can even deal with the variation of oil composition along the circumference. When bore distortion issue comes into the picture, this capability becomes very crucial. In this chapter, a model for oil evaporation on the liner is described. It takes similar approaches as [55-57, 63] to simulate the convective evaporation process, but with more accurate consideration of oil composition on the entire liner surface by incorporating with the 3-D ring-pack lubrication model.

As a supplement to the ring-pack lubrication model described in Chapter 4, this evaporation model calculates the rate of oil evaporation on every location of the liner at every computational step. The change of oil film thickness due to evaporation is calculated, which makes the lubrication model more complete. Meanwhile, the information of oil transport along the liner is used to compute the change of oil composition caused by the ring passage.

In this chapter, the key components of the evaporation sub-model are introduced first, with emphases on the calculation of evaporation rate and change of oil composition due to oil transport. The model is then applied to a light-duty diesel engine and detailed analyses are performed.

5.2 Model Formulation

In [63], the mass transfer Biot number, which is defined as the ratio of the oil species diffusion resistance in the liquid to the convection resistance in the gas phase, was found to be in the order of 10^{-3} to 10^{-2} during the engine cycle. The small Biot number indicates that the diffusion resistance is negligible and oil evaporation is limited by gas side convection. Consequently, it is appropriate to assume a uniform oil composition within the oil film, and the evaporation process reduces to a convective mass transfer in the liquid-gas interface.

5.2.1 Evaporation Rate

The approaches in [55-57, 63] were adapted for modeling the mass convection process. If the oil layer on the liner can be modeled as a mixture of N species with different vapor pressures and other thermo-physical properties, the oil evaporation rate in an engine cycle is the integration of the local evaporation rate of all species over time and space, as

$$\dot{M} = \frac{R}{T}\int_0^T \int_0^{L(t)} \int_0^{2\pi} \sum_{i=1}^{N} \dot{m}_i(\theta, x, t)\, d\theta dx dt \tag{5.1}$$

where R is the cylinder radius, T the period of one cycle, $L(t)$ the axial length of the liner that is exposed to the cylinder gases, $\dot{m}_i$ the local evaporation rate of species i. To evaluate the local evaporation rate, the standard expression for convective mass transfer is used such that

$$\dot{m}_i(\theta, x, t) = g_i(\theta, x, t) \times [\xi_i(\theta, x, t) - \xi_{i,\infty}(\theta, x, t)] \tag{5.2}$$

where g_i is the instantaneous local mass convective coefficient of specie i, ξ_i the instantaneous local vapor mass fraction of species i in the gas phase of the liquid-gas interface, and $\xi_{i,\infty}$ the vapor mass fraction of oil species i in the cylinder gases. Due to the large mass of cylinder gases relative to the small mass of expected oil vapor, $\xi_{i,\infty}$ is assumed to be zero. Therefore, to evaluate the local evaporation rate, only g_i and ξ_i are needed. In the following sections, the details of how to evaluation of g_i and ξ_i are stated.

Oil Model

To account for the complex volatility behavior of engine oils, the oil is modeled as being composed of several pure hydrocarbon species. The boiling point and mass fraction for each species must be specified. This data can be taken from a distillation curve for the oil of interest.

Once the boiling point is specified from the distillation curve, molecular weight of each oil species could be determined by using the polynomial relationship between the boiling point and the molecular weight of paraffin hydrocarbon [58]

$$M = aT_b^4 + bT_b^3 + cT_b^2 + dT_b + e \tag{5.3}$$

where, T_b is the boiling point of the oil species (°C), the coefficients: a=6.072×10^{-8}, b=-1.01431998×10^{-4}, c=0.691023398, d=-19.31502887594, and e=2139.90829605837.

The vapor pressure of each oil species can be calculated by using Antoine Equation. This equation correlates the temperature of a paraffin hydrocarbon T and its vapor pressure P^0 as

$$\log_{10} P^0 = A - \frac{B}{C+T} \tag{5.4}$$

where P^0 is in unit mmHg, T in unit °C, coefficients A, B and C are constants that are tabulated by the molecular weight of different paraffin hydrocarbon [58].

Evaluation of Mass Transfer Coefficient

The mass transfer coefficient is obtained by using the Chilton-Colburn analogy between heat and mass transfer, expressed as

$$g_i = \frac{h}{\rho c_p Le_i^{2/3}} \tag{5.5}$$

and

$$Le_i = \frac{k}{\rho c_p D_{i,gas}} \tag{5.6}$$

where h is the heat transfer coefficient, ρ and c_p the gas density and specific heat capacity, respectively, Le_i the Lewis number of oil species i, k the gas thermal conductivity, and $D_{i,gas}$ the diffusion coefficient of species i through the gas.

The heat transfer coefficient h is evaluated by using Woschni's correlation [59]. To evaluate the mass transfer coefficient, several cylinder gas properties are needed which depend on temperature. The temperature of the bulk cylinder gas is evaluated by using ideal gas law, where the mass of the mixture is estimated at the crank angle degree of intake vale closing. Then the average temperature of the liner and the bulk cylinder gas are used to evaluate the temperature dependent gas properties. The temperature measurements on the liner are used to estimate the temperature distribution on the liner with an expression based on the square root of the distance from the TDC of the top ring as [60]

$$T_{liner} = T_{TDC} - (T_{TDC} - T_{BDC})\sqrt{\frac{y}{s}} \tag{5.7}$$

where T_{liner} is the local liner temperature, T_{TDC} and T_{BDC} the liner temperatures at the locations of the top ring at TDC and BDC, respectively, y the liner location relative to the TDC location of the top ring, and s the engine stroke.

The binary diffusion coefficients for each oil species $D_{i,gas}$ are estimated by using the Wilke-Lee relation [61]

$$D_{12} = (0.00217 - 0.0005\sqrt{\frac{M_1 + M_2}{M_1 M_2}})\frac{T\sqrt{T}}{P}\frac{\sqrt{\frac{M_1 + M_2}{M_1 M_2}}}{\sigma_{12}{}^2 \Omega_D} \tag{5.8}$$

where D_{12} is the binary diffusion coefficient (cm^2/s), M the molecular weight (kg/kmol), T the temperature of air-oil vapor mixture (k), P the pressure of the mixture (atm), σ the characteristic Lennard-Jones length (Å), Ω_D the diffusion collision integral. How to calculate each term in Equation (5.8) is detailed in [61] and also briefly shown in the following.

For a pure oil component, the Lennard-Jones length

$$\sigma_{oil} = 1.18 V_b^{1/3} \tag{5.9}$$

where V_b is the Le Bas volume, which can be calculated as

$$V_b = 14.8 \times (number\ of\ C) + 3.7 \times (number\ of\ H) \tag{5.10}$$

For the air, σ_{air}=3.711. For the air-oil vapor mixture, the Lennard-Jones length is

$$\sigma_{air,oil} = \frac{\sigma_{air} + \sigma_{oil}}{2} \tag{5.11}$$

The diffusion collision integral is

$$\Omega_D = \frac{A}{T^{*B}} + \frac{C}{e^{DT^*}} + \frac{E}{e^{FT^*}} + \frac{G}{e^{HT^*}} \tag{5.12}$$

where, A=1.06036, B=0.15610, C=0.19300, D=0.47635, E=1.03587, F=1.52966, G=1.76474, H=3.89411, and

$$T^* = \frac{T}{(\varepsilon / k)_{1,2}} \tag{5.13}$$

For air-oil vapor mixture,

$$(\varepsilon / k)_{air,oil} = \sqrt{78.6 \times 1.15 T_b} \tag{5.14}$$

It needs to be noted that the units for T, $(\varepsilon/k)_{1,2}$ and T_b are all K.

Mass Fraction of Species in the Gas Phase of the Liquid-Gas Interface

The mass fraction of oil species is in general discontinuous across the phase interface. Thermodynamic equilibrium is assumed at the vapor-liquid interface, and the species mass fraction in the gas phase is obtained by using Raoult's law [58]:

$$\xi_i = \xi_{i,oil} \frac{P_i^0}{P} \frac{M_{oil}}{M_{air}} \tag{5.15}$$

where $\xi_{i,oil}$ is the mass fraction of species i in the liquid oil, P_i^0 the saturated vapor pressure of the pure-species, P the bulk cylinder gas pressure, M_{oil} the molecular weight of the oil, and M_{air} the molecular weight of air.

5.2.2 Change of Oil Composition due to Ring Passage

During an engine cycle, the composition of the oil film on the liner keeps changing due to the evaporation and ring passage. In this work, the evaporation is assumed to occur only on the portion of the liner exposed to the cylinder gases, and the change of mass fraction of an oil species due to the evaporation can be calculated in a straightforward way once the evaporation rate is known.

The calculation of the change of oil composition due to ring passage is associated with the lubrication of the piston ring-pack. As stated in Chapter 4, the lubrication in the ring/liner interface determines the oil film thickness at the trailing edge of the ring, which is in turn used to estimate the oil film thickness on the liner after ring passage. Analogue to this method, if the oil composition in the ring/liner interface is tracked, the composition of the oil on the liner can be obtained.

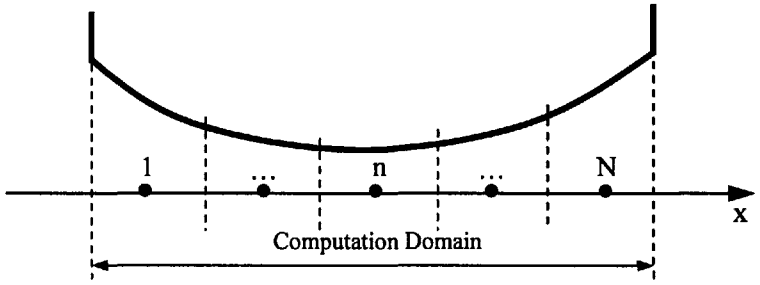

Figure 5-1 Discretization of computation domain

As shown in Figure 5-1, the ring/liner interface is discretized into a grid. The relative motion between the ring and the liner and the pressure difference between the leading and trailing edges can drive the oil from one node to another. The governing equation for species i at a specific location is

$$\frac{d(\xi_i h_{oil})}{dt} = -\frac{d(\xi_i q)}{dx} \tag{5.16}$$

where ξ_i is the mass fraction of species i in the oil, h_{oil} the oil film thickness at this location, q the oil flow rate at this location.

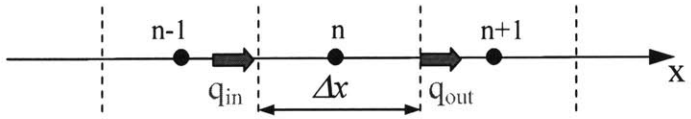

Figure 5-2 Mass conservation in a grid cell

As shown in Figure 5-2, if taking the grid cell of node n as the control volume, Equation (5.16) can be expressed in a discretization form with implicit temporal scheme

$$\frac{\xi_{i,n}{}^{t} h_{oil,n}{}^{t} - \xi_{i,n}{}^{t-\Delta t} h_{oil,n}{}^{t-\Delta t}}{\Delta t} = -\frac{\xi_{i,n}{}^{t} q_{out} - \xi_{i,n-1}{}^{t} q_{in}}{\Delta x} \tag{5.17}$$

where q_{in} and q_{out} are the rate of mass flow in and out of the grid cell, and the superscript "t" and "t-Δt" refer to the value at current and previous time step, respectively. In Equation (5.17), the mass flow rate q_{in} and q_{out} are known information from the hydrodynamics lubrication sub-model described in Chapter 4.

The collection of Equation (5.17) at all the nodal points is a set of linear equations. In these equations, the only unknowns are the mass fractions of species i at these nodal points. From Figure 5-2, it can be concluded that the mass fraction at one node can only be affected by its two neighbor nodes, therefore the collection of Equation (5.17) at all the nodes can be re-written as following format with a tri-diagonal coefficient matrix

$$\begin{bmatrix} \times & \times & & & \\ \vdots & \vdots & \vdots & & \\ & \times & \times & \times & \\ & & \vdots & \vdots & \vdots \\ & & & \times & \times \end{bmatrix} \begin{bmatrix} \xi_{i,1}{}^{t} \\ \vdots \\ \xi_{i,n}{}^{t} \\ \vdots \\ \xi_{i,N}{}^{t} \end{bmatrix} = [RHS] \tag{5.18}$$

The distribution of mass fraction of species i in the ring/liner interface can be obtained by solving Equation (5.18). For all the other species, similar equation as Equation (5.18) can be derived. As can be detected, although the Equation (5.18) for different species has different right-hand-side vector, their coefficient matrixes on the left hand side are the same. This feature implies that when solving Equation (5.18) for al the species, the inverse of the coefficient matrix only needs to be conducted once, and hence the computational efficiency is largely enhanced.

It is worthy of noting that the above calculation needs to be performed for the ring/liner interface at every cross-section of a ring, and for each ring. The oil composition at the trailing edge of a ring across the entire circumference is then used for estimating the oil composition on the liner after ring passage.

5.3 Sample Results

To facilitate the discussion, the same engine and operation conditions used in the demonstration of the ring-pack lubrication model in Chapter 4 is employed in this chapter. Synthetic oil is chosen for investigated. This oil is assumed to have fifteen species, and their identities are obtained from the distillation curve of this oil (Figure 5-3). The carbon number and the mass fraction of each paraffin hydrocarbon species are shown in Figure 5-4.

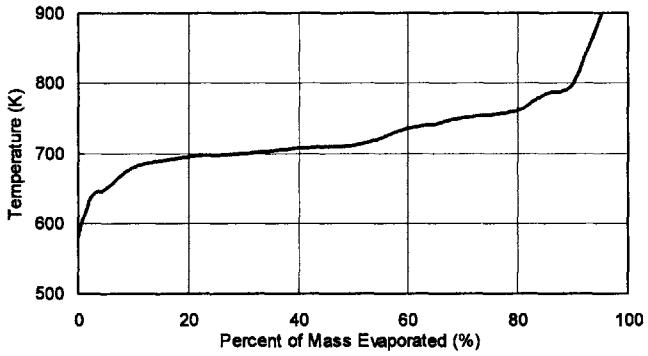

Figure 5-3 Distillation curve of synthetic oil

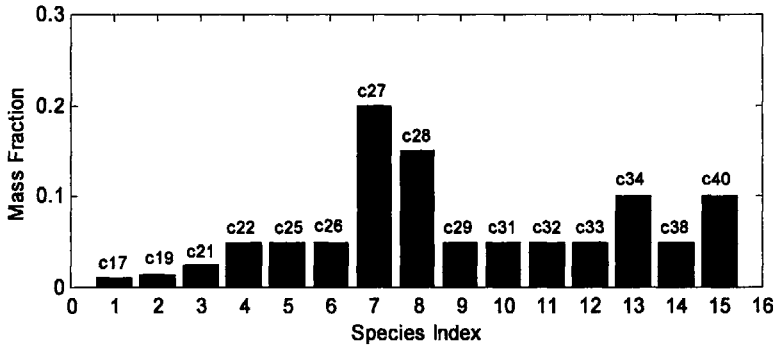

Figure 5-4 Composition of the synthetic oil

The model started with no oil on the dry region, and kept running for many cycles. During this process, the oil was transported gradually to the dry region, while the lighter species of the oil in the dry region was depleted. After about 30 cycles, except the oil film thickness around the upper bound of dry region, other parameters, such as overall evaporation rate, oil composition, etc., did not change too much from cycle to cycle, and the results are considered as steady state ones. The results shown below are all steady state ones.

Compared to the results of no-evaporation case in Chapter 4, even thought the evaporation does reduce the oil film thickness on the liner, its overall effects on the ring/liner lubrication is not significant. As shown in Figure 5-5 the oil film thickness on the liner after the top ring passes, it is almost identical to that of the no-evaporation case (Figure 4-24), except that the oil accumulating around the upper bound of dry region is less than the no-evaporation case. The conclusion of small effects of oil evaporation on ring/liner lubrication is drawn from the specific operating conditions and oil properties being tested, and is not a general conclusion. If faster evaporation occurs, it may largely decrease the oil film thickness, and thus influence the ring/liner lubrication more significantly.

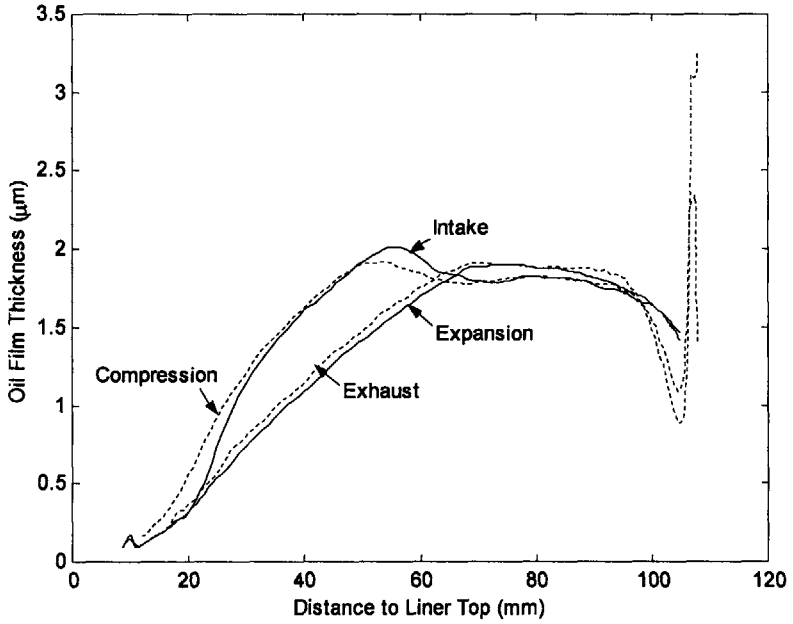

Figure 5-5 Liner oil film thickness after the top ring passes in each stroke under evaporation condition

The model results show that the total evaporated oil over a complete cycle is 0.175mg. The composition of the evaporated oil is shown in Figure 5-6. As can be see, light species contribute the most to the total evaporated oil. Specifically, the four lightest species, which are only 10% in the fresh oil, add up to 70% of the evaporated oil.

In this model, the oil vapor is tracked regarding on which axial location of the liner the oil is evaporated. As shown in Figure 5-7 the distribution of evaporation rate along the cylinder liner, the region around the lower bound of the dry region has the highest evaporation rate and contributes the most to the total oil evaporation. Inside the dry region, although the liner temperature increases as the

axial location getting closer to the liner top, the evaporation rate decreases because it becomes more difficult for fresh oil to be transported into the upper region. Around the lower bound of the dry region, the fresh oil is easy to reach as model assumption indicates. Meanwhile, the temperature at this region is still in a high level. These two factors determine that the highest evaporation rate occurs around the lower bound of the dry region. Further down to the lower region of the liner, although the fresh oil is easy to reach, the evaporation rate decrease rapidly because of the low liner temperature. It can be speculated that if fresh oil is assumed for the entire liner, the evaporation rate will increase as the location is closer to the liner top, and the evaporation rate in dry region will be unreasonably high.

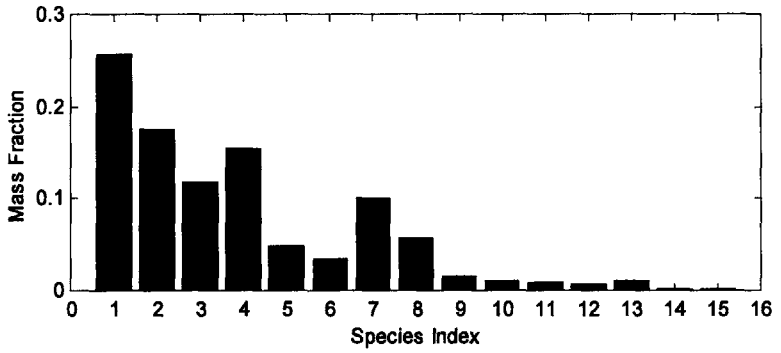

Figure 5-6 Contribution of different species to the total oil evaporation

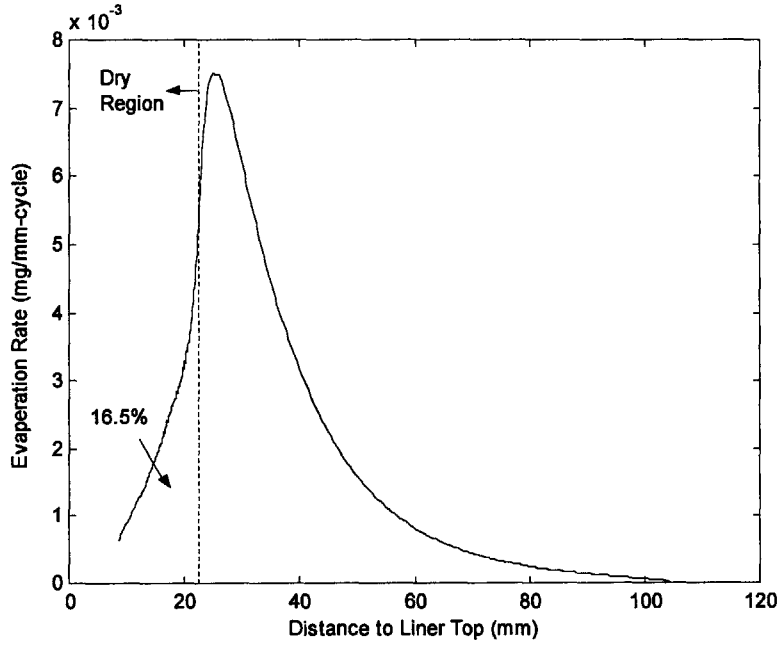

Figure 5-7 Distribution of evaporation rate along the liner

From above discussion, we can see that the transport of the light species to the upper region of the liner is of great importance to the oil evaporation. To better understand this issue, the oil film thickness on the upper region of the liner and the corresponding mass fraction of the four lightest species after the top ring passes in each stroke are shown in Figure 5-8 and Figure 5-9, respectively. From Figure 5-8, it can be seen that at the end of compression stroke, the oil film thickness is greater than that of the intake stroke, which means that some amount of oil is carried by the ring-pack from lower liner region to upper liner region. Corresponding to the change of oil film thickness, the mass fraction of the four lightest species in the dry region at the end of compression stroke is higher than that at the end of intake stroke, as shown in Figure 5-9. This is because the light species of oil on the lower liner region is less depleted than the upper liner region, and oil transport from the lower region to the upper region during the compression stroke can increase the concentration of light species in the upper region. During the following expansion stroke, the light species on the upper region is evaporated and their mass fraction decreases to a low level. From the analysis above, it can be concluded that oil transport plays a very important role in the oil evaporation. Without the continuous supply of light species to the upper liner region, the oil in this region will be greatly depleted and hard to be evaporated. A wise design of the piston ring-pack can diminish the amount of oil transport to the upper liner region, and hence reduce the oil evaporation.

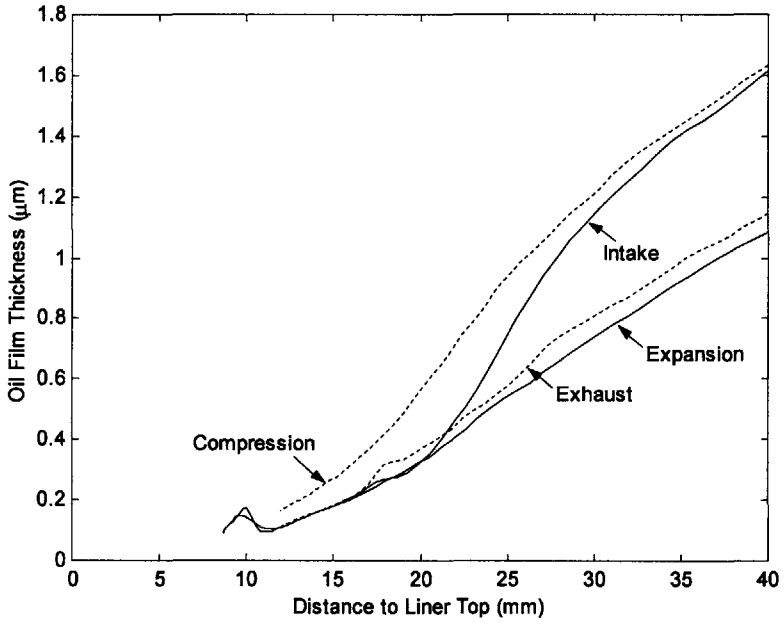

Figure 5-8 Oil film thickness on the liner after the top ring passes at the end of each stroke

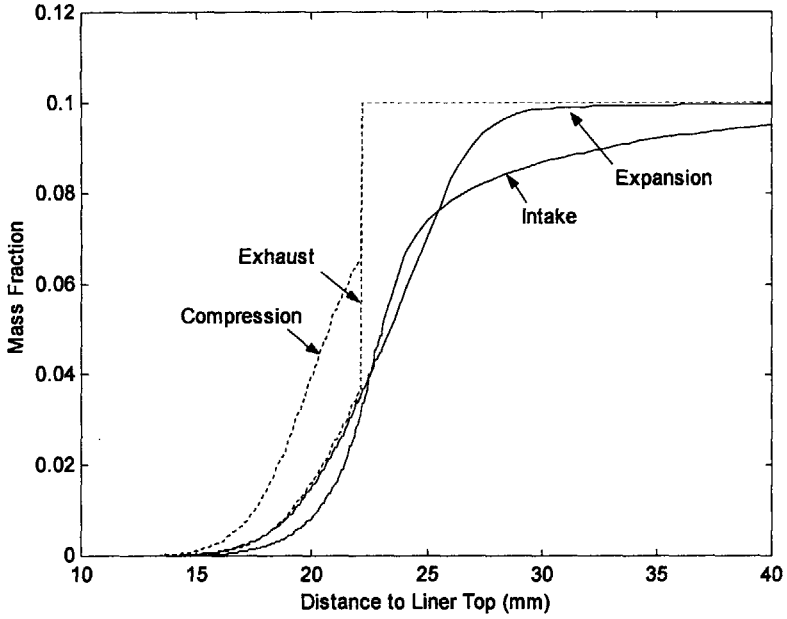

Figure 5-9 Mass fraction of four lightest species on the liner at the end of each stroke

It was shown in Chapter 4 that in the condition of bore distortion, the ring-pack can transport more oil to the upper region. According to above discussions, bore distortion may, therefore, induce more oil evaporation. To study the effects of bore distortion on oil evaporation, a bore distortion with 4^{th} order amplitude of 6μm (same as Figure 4-29) was chosen, and the ring gaps were fixed at 0 degree. The total evaporated oil over a complete cycle was found to be 0.199mg, about 13% increase compared to the case without bore distortion. The mass fractions of four lightest species on the liner at the circumferential location of 135 degree at the end of each stroke are shown in Figure 5-10. Comparing Figure 5-9 and 5-10, we can clearly see that more light species are transported to the dry region under bore distortion condition. The evaporation rates along the liner for both cases are shown in Figure 5-11, where more oil evaporated in the dry region due to the bore distortion is evident. Therefore, it can be concluded that besides the oil-scraping aspect that was revealed in the discussions of Chapter 4, bore distortion can affect the oil consumption through the oil evaporation aspect by transport more light species to the dry region.

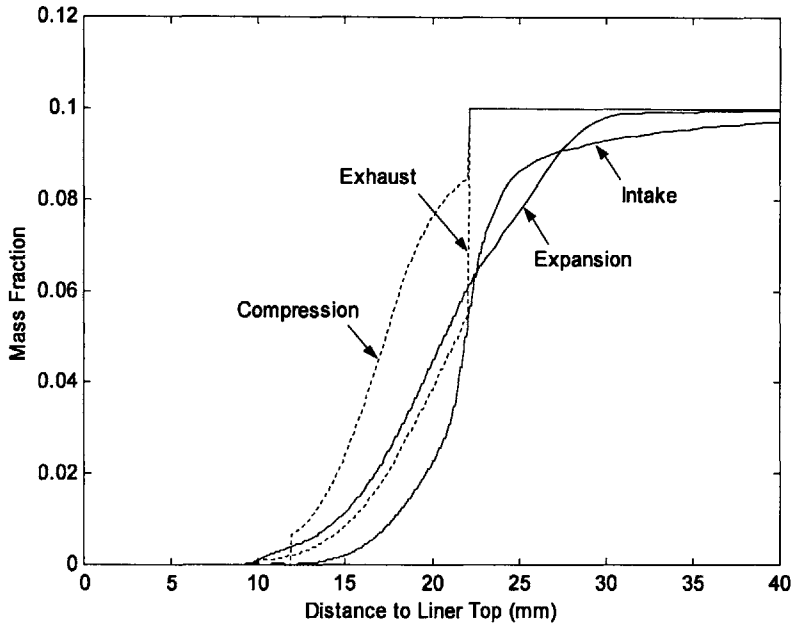

Figure 5-10 Mass fraction of four lightest species on the liner at the end of each stroke under bore distortion condition

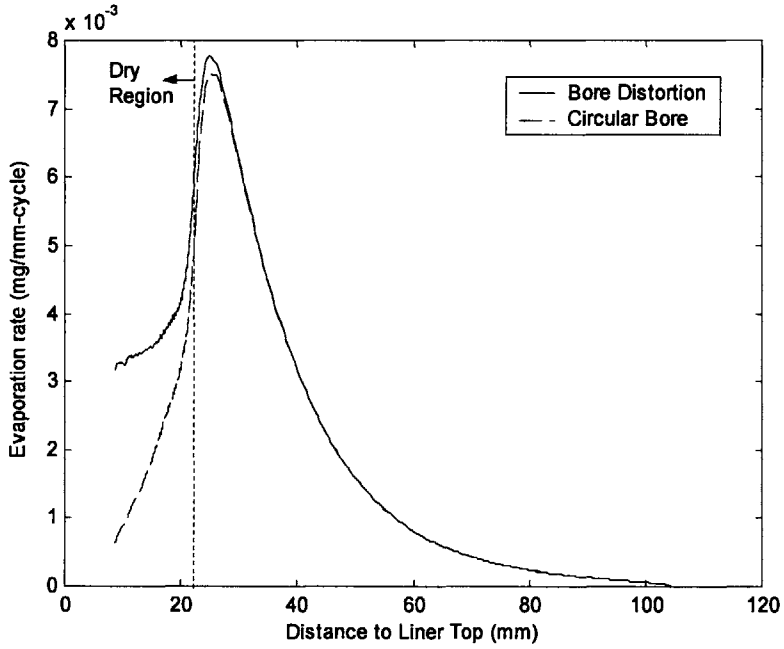

Figure 5-11 Distributions of evaporation rate along the liner with and without bore distortion

5.4 Conclusions

An oil evaporation sub-model has been developed to estimate the contribution of oil evaporation on the liner to oil consumption. The oil is modeled as being composed of several distinct hydrocarbon species each with its own boiling point and associated vapor pressure. Due to the depletion of light species and the temperature variation along the liner, the composition of oil changes with space and time. As a sub-model in the ring-pack lubrication simulation, it considers the oil transport induced change of oil composition, and at the same time addresses the influence of the oil evaporation on oil film thickness.

The model was applied to a light duty diesel engine. For the testing circumstances, following key findings are concluded:

- Light species contribute the most to the total evaporated oil. Specifically, the four lightest species, which are only 10% in the fresh oil, add up to 70% of the evaporated oil.
- Around the lower bound of the dry region, the fresh oil is easy to reach. Meanwhile, the temperature at this region is still in a high level. These two factors determine that the highest evaporation rate occurs around the lower bound of dry region.
- Due to the movement of the ring-pack along the liner, the oil can be transported from lower liner region to upper liner region, especially during compression stroke. Although the light species are depleted in the upper region, the continuing supply from lower region makes them always available for evaporation.
- With bore distortion existing, more fresh oil and hence more light species can be carried to the upper region of the liner. The rate of oil evaporation is therefore greater than the case without bore distortion.

Chapter 6 A Comprehensive Package for Piston Ring Analysis

From Chapter 2 to 5, three models have been developed to facilitate the analysis of piston rings. Although these models are separate from each other and each serves its own purpose, there do exist some connections among them (Figure 6-1). The dynamic analysis, which includes dynamics modeling and lubrication modeling, lacks the information of the ring-pack before it is inserted into the engine, and hence needs the initial loads from the static analysis (Ring Design Tool). Modeling ring-pack lubrication requires ring twist and inter-ring gas pressure as given information, which has to be prepared by the simulation of ring-pack dynamics. Therefore, in order to conduct a complete simulation of ring-pack lubrication, all three models have to be employed.

The combination of these three models is a comprehensive and highly integrated package for piston ring analysis. Its application scope ranges from design practice all the way to ring performance analysis. Most importantly, it can provide valuable 3-D information that will help researchers and engineers to develop more advanced understanding of the performance of the piston ring-pack, especially under the influence of non-axisymmetric characteristics of the power cylinder system.

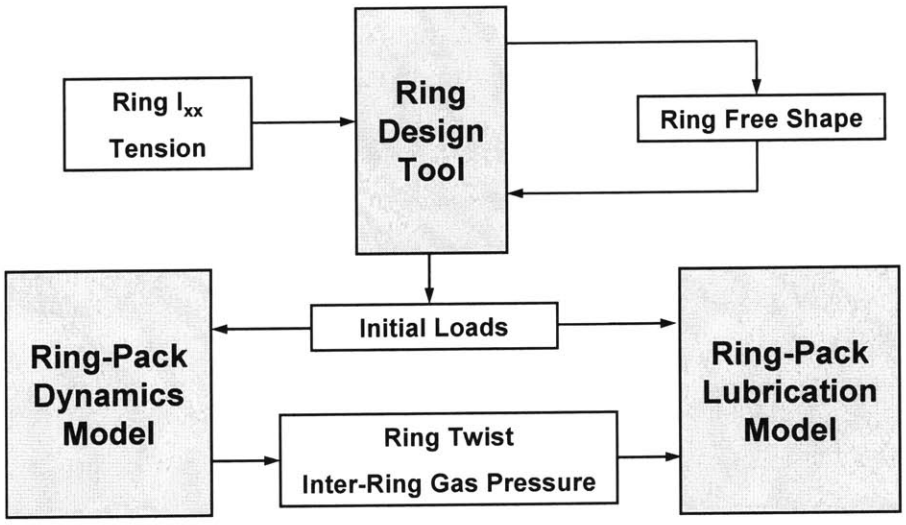

Figure 5-12 Connections among the models developed in this study

(This page intentionally left blank)

Chapter 7 Summary

To investigate the piston ring-pack performance under the influence of non-axisymmetric characteristics of the power cylinder system, three-dimensional models have been developed to conduct both static and dynamic analysis.

In the model for static analysis, a finite beam element model is implemented with incorporation of an asperity contact sub-model describing the interaction between the ring and the bore as well as the ring and the groove. A step-by-step approach is adopted to calculate the ring/bore and ring/groove conformability if ring free shape is given. A reverse process is used to determine the ring free shape as to achieve a specific tension distribution. To facilitate the ring design, the ovality calculation and the effects of external load and thermal stress on ring conformability are also modeled. Model results revealed the complex ring/bore and ring/groove interaction. Particularly, the 3-D geometrical shape of a ring with asymmetric cross-section after being compressed was obtained for the first time, and the large axial lifts at the ring tips were found to be responsible for the severe wear at those locations. This numerical tool has been successfully applied to the practice of ring design.

To study the ring-pack dynamic performance efficiently and accurately, ring dynamics and ring lubrication are simulated separately. In the 3-D model of ring-pack dynamics and blow-by gas flow, ring is discretized into straight beam elements. 3-D finite element analysis is employed to address the structural response of each ring to external loads. Physics-based sub-models are developed to simulate each ring's interactions with the piston groove and the liner. The gas flows driven by the pressure difference along both the axial and circumferential directions are modeled as well. This model predicts the inter-ring gas pressure and 3-D displacements of the three rings at various circumferential locations. Preliminary application of the model to a heavy-duty diesel engine shows significant variations of ring dynamics along the system circumference. Specifically, local ring flutter was detected for the second ring with an asymmetric cross-section and a non-uniform static twist angle distribution. Piston dynamic tilt was found to have a significant influence on the ring dynamics and gas flow by creating a negative relative angle between the twin-land oil control ring and its groove flanks. Significant variation of gas pressure along the circumference of piston land was also detected when the land-liner clearance is small. This model is the first comprehensive 3-D ring dynamics model.

In the 3-D ring-pack lubrication model, an improved flow continuity algorithm is implemented in the ring/liner hydrodynamic lubrication, and proves to be very practicable. The key improvement of this hydrodynamic lubrication model is the introduction of a transition region between the region

partially filled by oil and the region fully filled by oil in the ring/liner interface. This improvement eliminates the discontinuity of the convection flow at the boundary of these two regions and hence avoids the numerical problems that may be caused by this discontinuity otherwise. By coupling the ring/liner lubrication with the ring in-plane structural response, the lubrication along the entire ring circumference is calculated. The model has been applied to a light-duty diesel engine, and the results show significant variations of lubrication along the circumference due to non-axisymmetric characteristics of the power cylinder system. Bore distortion was found to have profound effects on oil transport along the liner. Particularly, it stimulates the occurrence of oil up-scraping by the top ring during compression stroke.

A sub-model of oil evaporation on the liner is incorporated with the ring-pack lubrication model. In this sub-model, the oil is modeled as being composed of several distinct hydrocarbon species each with its own boiling point and associated vapor pressure. With the help of the information of oil transport along the liner obtained in the lubrication model, the prediction of evaporation is more precise. The model was applied to a light-duty diesel engine. For the testing circumstances, it was found that the light species contribute the most to the total evaporated oil. Specifically, the four lightest species, which are only 10% in the fresh oil, add up to 70% of the evaporated oil. Around the lower bound of the dry region, the fresh oil is easy to reach; meanwhile, the temperature at this region is still in a high level; these two factors determine that the highest evaporation rate occurs around the lower bound of dry region. Due to movement of the ring-pack along the liner, the oil can be transported from lower liner region to upper liner region, especially during compression stroke; although the light species are depleted in the upper region, the continuing supply from lower region makes them always available for evaporation. With bore distortion existing, more oil and hence the light species can be carried to the upper liner region, and the rate of oil evaporation is, therefore, greater than the case without bore distortion.

The combination of these models is a comprehensive package for piston ring analysis, and can be used in wide applications ranging from ring design to the performance analysis. All of the components in this package are computationally robust and efficient, and hence have appreciable practical value.

References

1. Nakada, M., "Piston and Piston Ring Tribology and Fuel Economy," Proceedings of Internal Tribology Conference, Yokohama, 1993.
2. Heywood, J. B., *Internal Combustion Engine Fundamentals*, McGraw-Hill, 1988.
3. Tian, T., 2002, "Dynamic Behaviors of Piston Rings and Their Practical Impact. Part 1: Ring Flutter and Ring Collapse and Their Effects on Gas Flow and Oil Transport," Proc IMechE, Part J: Journal of Engineering Tribology, Vol. 216, pp. 209-227
4. Tian, T., 2002, "Dynamic Behaviors of Piston Rings and Their Practical Impact. Part 2: Oil Transport, Friction, and Wear of Ring/Liner Interface and the Effects of Piston and Ring Dynamics," Proc IMechE, Part J: Journal of Engineering Tribology, Vol. 216, pp. 229-247
5. Timoshenko, S., and Lessells, J. M., *Applied Elasticity*, Westinghouse Press, 1925.
6. Feodosyev, V. I., *Selected Problems and Questions in Strength of Materials*, Mir Publishers, 1977.
7. Sun, D. C., "A Thermal Elastica Theory of Piston-Ring and Cylinder-Bore Contact," ASME Journal of Applied Mechanics, Vol.58, pp. 141-153, 1991.
8. Ma, J., Ryan, T. W., Winter, J., and Dixon, R., 1996, "The Piston Ring Shape and Its Effects on Engine Performance," SAE Paper 960052.
9. Prescott, J., *Applied Elasticity*, Dover Publication Inc. New York, 1925.
10. Dunaevsky, V., Alexandrov, S., Barlat, F., 2000, "Analysis of Three-Dimensional Distortions of the Piston Rings with Arbitrary Cross-Section," SAE Paper 2000-01-3453.
11. Dunaevsky, V., Alexandrov, S., Barlat, F., 2001, "The Effect of Contact Pressure on Piston Ring Twist," SAE Paper 2001-01-2720.
12. Dunaevsky, V., Alexandrov, S., 2002, "Development of Conformability Model of Piston Rings with Consideration of Their Three-Dimensional Torsional Distortions and Fourier Series Representation of Cylinder Bore Geometry," SAE Paper 2002-01-3131.
13. Tian, T., Noordzij, L. B., Wong, V. W., and Heywood, J. B., 1998, "Modeling Piston-Ring Dynamics, Blowby, and Ring-Twist Effects," ASME Transaction – JOURNAL OF ENGINEERING FOR GAS TURBINES AND POWER, Vol.120, pp.843-854.
14. Namazian, M., and Heywood, J. B., 1982, "Flow in the Piston-Cylinder-Ring Crevices of a Spark-Ignition Engine: Effects on Hydrocarbon Emission, Efficiency and Power," SAE Paper 820088

15. Keribar, R., Dursunkaya, Z., and Flemming, M. F., 1991, "An Integrated Model of Ring Pack Performance," ASME Transaction - JOURNAL OF ENGINEERING FOR GAS TURBINES AND POWER, Vol.113, pp.382-389.
16. Ruddy, B. L., Parsons, B., Dowson, D., and Economou, P. N., 1979, " The Influence of Thermal Distortion and Wear of Piston Ring Groove upon the Lubrication of Piston Rings in Diesel Engines," Proceedings of the 6th Leeds-Lyon Symposium on Tribology.
17. Dursunkaya, Z., Keribar, R., and Richardson, D., 1993, "Experimental and Numerical Investigation of Inter-Ring Gas Pressures and Blowby in a Diesel Engine," SAE Paper 930792
18. Tian, T., Rabute, R., Wong, V. W., and Heywood, J. B., 1997, "Effects of Piston-Ring Dynamics on Ring/Groove Wear and Oil Consumption in a Diesel Engine," SAE Paper 970835
19. Rabute, R. and Tian, T., 2001, "Challenges involved in Piston Top Ring Designs for Modern SI Engines," ASME Transaction - JOURNAL OF ENGINEERING FOR GAS TURBINES AND POWER, Vol.123, pp.448-459.
20. Dowson, D., Economou, P. N., Ruddy, B. L., Strachan, P. J., and Baker, A. J. S., 1979, "Piston Ring Lubrication – Part II. Theoretical Analysis of a Single Ring and a Completer Ring Pack," Energy Conservation through Fluid Film Lubrication Technology: Frontiers in Research and Design, Winter annual Meeting of ASME, pp.23-52.
21. Keribar, R., Dursunkaya, Z., and Flemming, M. F., 1991, "An Integrated Model of Ring Pack Performance," ASME Transaction - JOURNAL OF ENGINEERING FOR GAS TURBINES AND POWER, Vol.113, pp.382-389.
22. Richardson, D. E. and Borman, G. L., 1992,"Theoretical and Experimental Investigations of Oil Films for Application to Piston Ring Lubrication," SAE Paper 922341.
23. Jeng, Y. R., 1992, "Friction and Lubrication Analysis of a Piston-Ring Pack," SAE Paper 920492.
24. Taylor, R. I., Brown, M. A., Tompson, D. M., and Bell, J. C., 1994, "The influence of Lubrication Rheology on Friction in the Piston Ring-Pack," SAE Paper 941981.
25. Tian, T., Wong, V. W., and Heywood, J. B., 1996, "A Piston Ring-Pack Film Thickness and Friction Model for Multigrade Oils and Rough Surfaces," SAE Paper 962032.
26. Liu, L., Tian, T., and Rabute, R., 2003, "Development and Application of an Analytical Tool for Piston Ring Design," SAE Paper 2003-01-3112.
27. Thirouard, B., 2001, "Characterization and Modeling of the Fundamental Aspects of Oil Transport in the Piston Ring Pack of Internal Combustion Engines," Ph.D. Thesis, MIT.

28. Ejakov, M. A., Schock, H. J., and Brombolich, L. J., 1998, "Modeling of Ring Twist for an IC Engine," SAE Paper 982693.
29. Hu, Y., Cheng, H. S., Arai, T., Kobayashi, Y., and Aoyama, S., 1993, "Numerical Simulation of Piston Ring in Mixed Lubrication – A Nonaxisymmetrical Analysis," ASME Journal of Tribology, 93-Trib-9.
30. Ma, M-T, Sherrington, I., and Smith, E. H., 1997, "Analysis of Lubrication and Friction for a Complete Piston-Ring Pack with an Improved Oil Availability Model. Part 1: Circumferentially Uniform Film," Proc IMechE, Part J: Journal of Engineering Tribology, Vol. 211, pp. 1-15.
31. Ma, M-T, Sherrington, I., and Smith, E. H., 1997, "Analysis of Lubrication and Friction for a Complete Piston-Ring Pack with an Improved Oil Availability Model. Part 2: Circumferentially Variable Film," Proc IMechE, Part J: Journal of Engineering Tribology, Vol. 211, pp. 17-27.
32. Mierbach, A., Duck, G. E., and Newman, B. A., 1983, "Heat Flow through Piston Rings and Its Influence on Shape," SAE Paper 831283.
33. Greenwood, J. A., and Tripp, J. H., 1971, "The Contact of Two Nominally Flat Surfaces," Proc. Inst. Mech. Engrs., Vol. 185, p.625.
34. Shapiro, A. H., "The Dynamics and Thermodynamics of Compressible Fluid Flow," Vol. I, The Ronald Press Company, New York, 1953
35. Press, W. H., Teukolsky, S. A., Vetterling, W. T., and Flannery, B., 1992, *Numerical Recipe*, Cambridge University Press, Second Edition.
36. Liu, L., Tian, T., and Rabute, R., 2003, "Development and Application of an Analytical Tool for Piston Ring Design," SAE Paper 2003-01-3112.
37. Hamilton, G. M. and Moore, S. L., 1974, "The Lubrication of Piston Rings," Proc. IMechE, Vol. 188, 253-268
38. Moore, S. L. and Hamilton, G. M., 1978, "The Starved Lubrication of Piston Rings in a Diesel Engine," J. Mech. Engng Sci., 20(6), 345-352.
39. Brown, S. R. and Hamilton, G. M., 1977, "The Partially Lubricated Piston Ring," J. Mech. Engng Sci., 19(2), 81-89.
40. Lux, J. P. and Hoult, D. P., 1991, "Lubricant Film Thickness Measurements in a Diesel Engine Piston Ring Zone," STLE, Tribology Trans., 47(5), 353-364.
41. Prest, M., Dowson, D. and Taylor, C. M., 2000, "Theoretical Modeling of Cavitation in Piston Ring Lubrication," Proc. IMechE, Part C: Journal of Mechanical Engineering Science, Vol.214, pp. 435-447.

42. Jakobsson, B. and Floberg, L., 1957, "The Finite Journal Bearing Considering Vaporization," Transcript 190, Chalmers University of Technology, Sweden.
43. Olsson, K., 1965, "Cavitation in Dynamically Loaded Bearings," Transcript 26, Chalmers University of Technology, Sweden.
44. Elrod, H. G., 1981, "A Cavitation Algorithm," Tran. ASME, J. Lubric. Technol., Vol.103, pp. 350-355.
45. Paydas, A. and Smith, E. H., 1992, "A Flow-Continuity Approach to the Analysis of Hydrodynamic Journal Bearings," Proc. IMechE., Part C: Journal of Mechanical Engineering Science, Vol.206, pp51-69
46. Ma, M-T, Sherrington, I., and Smith, E. H., 1996, "Implementation of an Algorithm to Model the Starved Lubrication of a Piston Ring in Distorted Bore: Prediction of Oil Flow and Onset of Gas Blow-By," Proc. IMechE, Part J: Journal of Engineering Tribology, Vol. 210, pp. 29-44.
47. Richardson, D.E., Borman, G.B., 1991, "Using Fiber Optics and Laser Fluorescence for Measuring Oil Films with Application to Engines," SAE Paper 912388.
48. Tamai, G., 1995, "Experimental Study of Engine Oil Film Thickness Dependence on Liner Location, Oil Properties, and Operating Conditions," M.S. Thesis, Department of Mechanical Engineering, MIT, September, 1995.
49. Liu, L. and Tian, T., 2005, "Modeling Piston Ring-Pack Lubrication with Consideration of Ring Structural Response," SAE Paper 2005-01-1641.
50. Liu, L., Tian, T., 2004, "A Three-Dimensional Model for Piston Ring-Pack Dynamics and Blow-by Gas Flow," ASME ICE Fall Technical Conference, ICE 2004-968.
51. Liu, L., Tian, T., 2005, "Implementation and Improvements of a Flow Continuity Algorithm in Modeling Ring/Liner Lubrication," SAE Paper 2005-01-1642.
52. Orrin, D. s. and Coles, B. W., 1971, "Effect of Engine Oil Composition on Oil Consumption", SAE Paper 710141.
53. Didot, F. E., Green, E., and Johnson, R. H., 1987, "Volatility and oil Consumption of SAE 5-30 Engine oil", SAE Paper 872126.
54. Furuhama, S., Hiruma, M., and Yoshida, H., 1981, "An Increase of Engine Oil Consumption at High Temperature of piston and cylinder", SAE Paper 810976.
55. Yilmaz, E., Tian, T., Wong, V. W., and Heywood, J. B., 2002, "An Experimental and Theoretical Study of the Contribution of Oil Evaporation to Oil Consumption", SAE Paper 2002-01-2684.

56. Wahiduzzaman, S., Keribar, R., Dursunkaya, Z., and Kelley, F. A., 1992, "A Model for Evaporative Consumption of Lubricating Oil in Reciprocating Engines", SAE Paper 922202.
57. Audette III, W. E., and Wong. V. W., 1999, "A Model for Estimating Oil Vaporization from the Cylinder Liner as a Contributing Mechanism to Engine Oil Consumption", SAE Paper 1999-01-1520.
58. Zwolinski, B. J., Whlhoit, R. C., *Handbook of Vapor Pressures and Heats of Vaporization of Hydrocarbons and Related Compounds*, College Station: Thermodynamics Research Center, Dept. of Chemistry, Texas A&M University, 1971.
59. Woschni, G., and Fieger, J., "Experimentelle Bestimmung des ortlich gemittelten Warmeubergangskoeffizienten im Ottomotor", MTZ Vol. 42, No.6, pp.229-234, 1981.
60. Woschni, G., and Zeilinger, K., "Vorausberechnung des Kolbenringverhaltens", FVV Workshop, Tribosystem Kolben-Kolbenring-Zylinderlaufflache, 10. Oktober, VDMA-Haus Frankfurt, 1989.
61. Reid, R. C., Prausnitz, J. M., and Sherwood, T. K., *The Properties of gases and Liquids*, 3rd Ed., McGraw-Hill, 1977.
62. Tian, T., 1997, "Modeling the Performance of the Piston Ring-Pack in Internal Combustion Engines," Ph.D. Thesis, MIT.
63. Yilmaz, E., 2003, "Sources and Characteristics of Oil Consumption in a Spark-Ignition Engine," Ph.D. Thesis, MIT.